The Astrophysical Journal, 898:25 (38pp), 2020 July 20 https://doi.org/10.3847/1538-4357/ab9b8c

Formation and Evolution of Compact-object Binaries in AGN Disks

Hiromichi Tagawa[1], Zoltán Haiman[2], and Bence Kocsis[1]
[1] Institute of Physics, Eötvös University, Pázmány P.s., Budapest, 1117, Hungary; htagawa@caesar.elte.hu
[2] Department of Astronomy, Columbia University, 550 W. 120th Street, New York, NY 10027, USA
Received 2019 December 17; revised 2020 May 10; accepted 2020 May 18; published 2020 July 20

Abstract

The astrophysical origin of gravitational wave (GW) events discovered by LIGO/VIRGO remains an outstanding puzzle. In active galactic nuclei (AGNs), compact-object binaries form, evolve, and interact with a dense star cluster and a gas disk. An important question is whether and how binaries merge in these environments. To address this question, we have performed one-dimensional *N*-body simulations combined with a semianalytical model that includes the formation, disruption, and evolution of binaries self-consistently. We point out that binaries can form in single–single interactions through the dissipation of kinetic energy in a gaseous medium. This "gas-capture" binary formation channel contributes up to 97% of gas-driven mergers and leads to a high merger rate in AGN disks even without preexisting binaries. We find the merger rate to be in the range of $\sim$0.02–60 $\mathrm{Gpc^{-3}\,yr^{-1}}$. The results are insensitive to the assumptions on the gaseous hardening processes: we find that once they are formed, binaries merge efficiently via binary–single interactions even if these gaseous processes are ignored. We find that the average number of mergers per black hole (BH) is 0.4, and the probability for repeated mergers in 30 Myr is $\sim$0.21–0.45. High BH masses due to repeated mergers, high eccentricities, and a significant Doppler drift of GWs are promising signatures that distinguish this merger channel from others. Furthermore, we find that gas-capture binaries reproduce the distribution of low-mass X-ray binaries in the Galactic center, including an outer cutoff at $\sim$1 pc due to the competition between migration and hardening by gas torques.

Unified Astronomy Thesaurus concepts: Gravitational wave sources (677); Active galactic nuclei (16); Black holes (162); Low-mass x-ray binary stars (939); Close binary stars (254); N-body simulations (1083)

1. Introduction

Recent detections of gravitational waves (GWs) have shown evidence for a high rate of black hole (BH)–BH and neutron star (NS)–NS mergers in the universe (Abbott et al. 2016a, 2016b, 2017a, 2017b, 2017c, 2019a; Zackay et al. 2019, 2020; Venumadhav et al. 2020). However, the proposed astrophysical pathways to mergers remain highly debated. Possible compact-object merger pathways include isolated binary evolution (Dominik et al. 2012; Kinugawa et al. 2014; Belczynski et al. 2016, 2017; Breivik et al. 2016; Giacobbo et al. 2018; Bavera et al. 2019; Spera et al. 2019) accompanied by mass transfer (Inayoshi et al. 2017a; Pavlovskii et al. 2017; van den Heuvel et al. 2017), common-envelope ejection (e.g., Paczynski 1976; Ivanova et al. 2013), envelope expansion (Tagawa et al. 2018), or chemically homogeneous evolution in a tidally distorted binary (de Mink & Mandel 2016; Mandel & de Mink 2016; Marchant et al. 2016), evolution of triple or quadruple systems (Antonini et al. 2017; Liu & Lai 2017, 2018, 2019; Silsbee & Tremaine 2017; Arca-Sedda et al. 2018; Hoang et al. 2018b; Randall & Xianyu 2018; Fragione & Kocsis 2019; Fragione et al. 2019; Michaely & Perets 2019), gravitational capture (O'Leary et al. 2009; Kocsis & Levin 2012; Gondán et al. 2018b; Rodriguez et al. 2018; Rasskazov & Kocsis 2019; Zevin et al. 2019; Samsing et al. 2020), dynamical evolution in open clusters (Banerjee 2017, 2018a, 2018b; Bouffanais et al. 2019; Kumamoto et al. 2019; Rastello et al. 2019) and dense star clusters (e.g., Portegies Zwart & McMillan 2000; O'Leary et al. 2006, 2016; Samsing et al. 2014; Ziosi et al. 2014; Mapelli 2016; Rodriguez et al. 2016a, 2016b; Askar et al. 2017; Fujii et al. 2017; di Carlo et al. 2019; Zevin et al. 2019; Zhang et al. 2019), and dynamical interaction in gas-rich nuclear regions (McKernan et al. 2012, 2014, 2018; Bellovary et al. 2016; Bartos et al. 2017; Stone et al. 2017; Leigh et al. 2018; Tagawa & Umemura 2018; Yi et al. 2018; Secunda et al. 2019; Yang et al. 2019a, 2019b; Gayathri et al. 2020; McKernan et al. 2020; Tagawa et al. 2020).

Twelve low-mass X-ray binary (LMXB) candidates have also recently been discovered by Hailey et al. (2018) within a distance $r \lesssim 1$ pc of the Galactic center, with a density distribution of $\propto r^{-1.5\pm0.3}$, by observing X-ray sources within $\sim$4 pc presented by Muno et al. (2009). Generozov et al. (2018) proposed that the density profile of these hard binaries can be explained by the tidal capture mechanism and stellar relaxation processes. Although this model predicts the radial distribution of LMXBs to be $\propto r^{-(0.9-1.4)}$, the outer cutoff at $\sim$1 pc remains unexplained.

Galactic nuclei are the densest environments of stars and compact objects in the universe (Walcher et al. 2005; Merritt 2010; Norris et al. 2014; Gallego-Cano et al. 2018). In the active phase of a galactic nucleus, a high-density gas disk forms within 0.1–10 pc (Burtscher et al. 2013) of a central supermassive BH (SMBH). In such environments, binaries form and evolve through interaction with densely populated stars and gas. Baruteau et al. (2011) showed that even when a binary is so massive that it opens a gap within the accretion disk around an SMBH, it is efficiently hardened via gas dynamical friction. McKernan et al. (2012, 2014) predicted the formation of intermediate-mass BHs (IMBHs) in active galactic nucleus (AGN) disks due to collisions of compact objects. Bartos et al. (2017) have proposed a pathway for BH–BH mergers in AGN disks, in which binaries are captured in an

accretion disk within ∼0.01 pc of the central SMBH due to linear momentum exchange, and after that, binaries are hardened by gas dynamical friction of the AGN disk and by type I/II torques of a circumbinary disk. Stone et al. (2017) proposed another pathway, in which binaries that formed in situ at ∼parsec scale evolve via the effects of binary–single interactions with a stellar disk and via type I/II torques from a circumbinary disk. Leigh et al. (2018) showed that fewer than 10 binary–single interactions are sufficient to drive hard binaries with a binary separation of $s \lesssim 10$ au to merger. McKernan et al. (2018, 2020) estimated the mass and spin distributions of the merged BHs and the merger rate in AGN disks. Bellovary et al. (2016) suggested that BHs accumulate and merge with each other in migration traps at 20–300 Schwarzschild radii, where the torque by the AGN disk changes sign. Secunda et al. (2019) and Yang et al. (2019b) modeled the formation of binaries within the migration traps. Just et al. (2012), Kennedy et al. (2016), and Panamarev et al. (2018) discussed the capture of stars in an AGN disk and their subsequent migration toward the central SMBH due to the ram pressure of an AGN disk. Tagawa et al. (2020) investigated the distribution of the effective spin parameter for mergers in AGN disks.

Previous studies of compact-object mergers in AGN disks have focused on the role of gas in driving binary mergers assuming preexisting binaries in the nuclear star cluster (Bartos et al. 2017) or in the disk itself (Stone et al. 2017; McKernan et al. 2018), or assuming that binaries form at migration traps (Bellovary et al. 2016; Secunda et al. 2019; Yang et al. 2019a, 2019b; Gayathri et al. 2020). In the present study, we examine the formation of binaries during close two-body encounters in a gaseous medium, where the gas absorbs some of the initial kinetic energy of the two objects. Goldreich et al. (2002) proposed that planetesimal binaries can form in the Kuiper Belt due to the dissipation of the relative velocity between the planetesimals by dynamical friction in the environment of a background population of smaller solid bodies. They showed that this leads to efficient binary formation in the Kuiper Belt, but to our knowledge, the analogous mechanism of binary formation in an AGN disk has not been previously explored. Here we include this "gas-capture" binary formation mechanism and find that it supplies the majority of binaries in AGN disks. We also examine binary formation in dynamical three-body encounters (e.g., Aarseth & Heggie 1976; Binney & Tremaine 2008), which have also been ignored in previous studies of mergers in AGN disks, but find this mechanism to be less important. These mechanisms enable binary formation in AGN disks without migration traps whose existence and properties are poorly understood.

More generally, in this paper we investigate whether and how binaries form and merge in AGN disks. We combine one-dimensional *N*-body simulations with a semianalytical model, which incorporates the effects of gas dynamical friction, type I/II migration torques, GW radiation, and several different types of stellar interaction. We simulate the evolution of both single and binary objects, and follow their radial position from the central SMBH, as well as their velocities in time, together with the evolution of the binaries' separation. The other two spatial directions are followed only statistically. Our flexible model allows us to test previous assumptions on whether and how efficiently binaries may merge in AGN disks (e.g., McKernan et al. 2020 and references above) and to examine the dependence of the merger rate on the model parameters of the AGN disk and the stellar cluster.

The rest of this paper is organized as follows. In Section 2, we give an executive summary of our method and describe the numerical scheme and the setup of simulations in detail in Section 3. We present our main results in Section 4. We discuss the implications for the spin and eccentricity distribution, the merger rate, and a comparison with LMXBs observed in the Galactic nucleus in Section 5. We summarize our conclusions in Section 6. For clarity, the variables used in this paper are listed and defined in Table 1.

2. Overview of Simulations

We consider a system describing a galactic nucleus, consisting of the following five components: (1) a central SMBH, (2) a gaseous accretion disk ("AGN disk"), (3) a spherical stellar cluster, (4) a flattened cluster of BHs, and (5) stars and BHs inside the AGN disk, referred to as the "disk stellar" and "disk BH" components (Section 3.1.2). Figure 1 illustrates our setup.

In our fiducial model, we adopt the SMBH mass and the distribution of stars from observations of the quiescent central region of the Milky Way at present (Section 3.1.1), which does not have an AGN. Also we generate the BH mass distribution using the results of population synthesis models and accounting for an initially mass segregated radial distribution (Section 3.1.1). On the other hand, our model with an AGN disk represents the conditions during the active phase, which is believed to have existed at an earlier time in the Milky Way's history (e.g., Wardle & Yusef-Zadeh 2008; Su et al. 2010; Zubovas et al. 2011; Bland-Hawthorn et al. 2013).

We employ the AGN accretion disk model proposed by Thompson et al. (2005) (Section 3.1.3), as adopted in the earlier work by Stone et al. (2017). This represents a Shakura–Sunyaev α disk with a constant viscosity parameter α and accretion rate in the region where it is not self-gravitating. The model describes a radiatively efficient, geometrically thin, and optically thick disk and extends the disk to parsec scales with a constant Toomre parameter in the self-gravitating regime (see Figure 4 below), assuming that it is stabilized by radiation pressure and supernovae from in situ star formation. We assume that stars and BHs form in the disk at the rate required to stabilize the AGN disk, and some fraction of BHs are initially formed in binaries (Section 3.1.3).

To follow the time evolution of the BHs in this system, focusing on their capture by the disk, and the formation and disruption of BH binaries in the disk, we run one-dimensional *N*-body simulations combined with a semianalytical method. Binaries form in the disk either due to gas dynamical friction (Section 3.3.8) or due to three-body encounters (Section 3.3.7), and are disrupted by soft-binary–single interactions. We assume that binaries are disrupted when the binary separation becomes larger than the Hill radius of a binary with respect to the SMBH.

We model the evolution of the orbital separation (s_j), the radial position (r_j), and the magnitude of a random velocity relative to the local Keplerian AGN disk motion (v_j) for all binaries labeled with the binary index j. We also track the radial position (r_i) and random velocity (v_i) of single compact objects, which represent stellar-mass BHs. These quantities evolve

Table 1
Notation

Symbol	Description	Symbol	Description
i, j, k	The index of a single BH, a BH binary, and either of a single BH or a BH binary	$v_{\rm Kep}(r)$	The Keplerian velocity at the distance r from the SMBH
l	The index of a cell, in which physical quantities are stored	$M_{\rm SMBH}$, $\bar{m}_{\rm star}$	The SMBH mass and the average stellar mass
xy, z	The direction of the plane and the angular momentum of the AGN disk	$\rho_{\rm gas}$, $n_{\rm gas}$	The mass and number density of gas
t, Δt	The elapsed time and the time step in simulations	$\Sigma_{\rm disk}$	The surface density of a gas disk
r, r_k, r_l,Δr_l	The distance, the distance of the kth object, the distance of the geometric center of the lth cell from the SMBH, and the width of the lth cell	$h_{\rm disk}$	The scale height of a gas disk
s_j, v_j, $v_{{\rm bin},j}$	The binary separation, the velocity of the center of mass of the binary relative to the local AGN motion, and the relative rotation velocity of the binary components in the jth BH binary	$c_{\rm s}$	The sound velocity of gas
v_k, $v_{xy,k}$, $v_{z,k}$	The magnitude of the velocity and the xy and z-direction velocity of the center of mass for the kth object relative to the local AGN motion	Ω	The angular velocity of a gas disk
m_k, m_{j_1}, m_{j_2}	The mass of the kth object, and the primary and secondary masses in the jth binary, respectively	$t_{\rm AGN}$	The typical lifetime of AGN disks
h_k	The typical height of the orbital motion for the kth object, $h_k = v_{z,k} r_k / v_{\rm Kep}$	$\dot{M}_{\rm out}$	The gas accretion rate from the outer radius $r_{\rm out}$
$r_{{\rm Hill},k}$	The Hill radius of the kth object with respect to the SMBH, $r_{\rm Hill} = r_k (m_k / 3M_{\rm SMBH})^{1/3}$	$\dot{M}_{\rm Edd}$	The Eddington accretion rate
$v_{{\rm rel},k}$	The typical relative velocity of a third body relative to the center of mass for the kth object	$\beta_{\rm v}$	The parameter setting the initial velocity dispersion for BHs
$b_{90,k}$	The impact parameter of the kth object at which the direction of particles changes by 90° after an encounter, $b_{90,k} = G(m_k + m_{\rm c}) / v_{{\rm rel},k}^2$	$\delta_{\rm IMF}$	A power-law exponent for the initial mass function of stars
$r_{{\rm BHL},k}$	The Bondi–Hoyle–Lyttleton radius for the kth object, $r_{{\rm BHL},k} = m_k G / (v_k^2 + c_s^2)^{3/2}$	$M_{\rm star,3pc}$	The stellar mass within 3 pc from the SMBH
$\dot{m}_{{\rm BHL},k}$	The Bondi–Hoyle–Lyttleton accretion rate for the kth object (Equation (29))	γ_ρ	A power-law exponent of the radial profile of the initial BH distribution (Equation (1))
$p_{{\rm disk},k}$, $p_{{\rm c},k}$	The time fraction that the kth object spends within the AGN disk and a background component, respectively, $p_{{\rm disk},k} = \frac{2}{\pi} a \sin(h_{{\rm AGN},l} / h_k)$, $p_{{\rm c},k} = \frac{2}{\pi} a \sin(h_{\rm c} / h_k)$	$\Gamma_{\rm Edd,cir}$	The Eddington accretion rate onto a BH binary from a circumbinary disk
$\rho_{\rm c}$, $n_{\rm c}$	The mass and number density of a background component	$m_{\rm AM}$	The efficiency of angular momentum transport in outer regions of the AGN disk
$\sigma_{\rm c}$	The one-dimensional velocity dispersion of a background component	$v_{\rm GW}$	The recoil velocity on a merger remnant due to anisotropic GW radiation
$m_{\rm c}$	The average mass of a background component	$f_{\rm pre}$	The number of preexisting binaries over the number of initial BHs
$h_{\rm c}$	The average orbital height of a background component	$\alpha_{\rm SS}$	The α parameter that gives the efficiency of angular momentum transport in standard thin disks
$\rho_{{\rm AGN},l}$	The mass density of the AGN disk at r_l	η_t	The time-step parameter
$h_{{\rm AGN},l}$	The height of the AGN disk at r_l	$N_{\rm cell}$	The number of cells storing physical quantities

Table 1
(Continued)

Symbol	Description	Symbol	Description
$N_{\rm totBH,ini}$, $N_{\rm mer}$, $N_{\rm bin}$, $N_{\rm acc}$, $N_{\rm mer,SF}$	The number of initial BHs, mergers, binaries, migrators within $r_{\rm in}$, and mergers among in situ formed BHs	$r_{\rm in,BH}$, $r_{\rm out,BH}$	The inner and outer boundaries for r within which BHs are initially distributed
$f_{\rm mer,pre}$, $f_{\rm mer,gas}$, $f_{\rm mer,dyn}$, $f_{\rm mer,rep}$	The fraction of mergers among preexisting binaries, gas-capture binaries, dynamically formed binaries, and repeated mergers over total mergers	$r_{\rm in}$, $r_{\rm out}$	The inner and outer boundaries for r within which we calculate
$f_{\rm BH,mer}$	The number of mergers over the initial number of BHs, $f_{\rm BH,mer} = N_{\rm mer}/N_{\rm ini,BH}$	$f_{\rm BH}$, $f_{\rm BH,n}$	The fraction of the mass and the number of all stellar-mass BHs over the mass of all stars

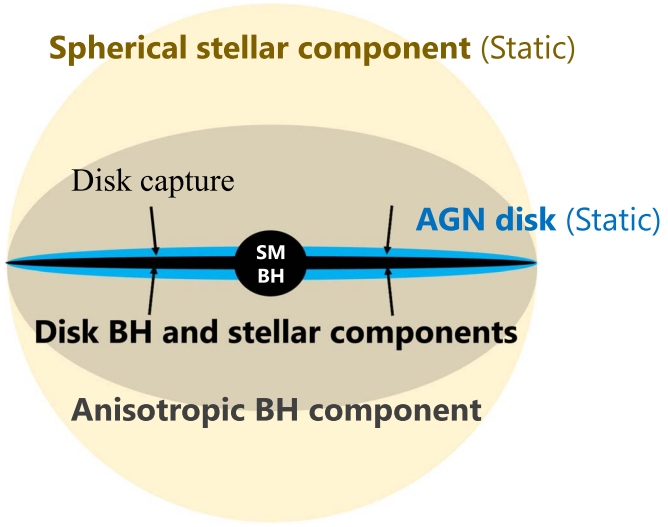

Figure 1. Components describing an active galactic nucleus, including (1) a central SMBH, (2) a gaseous AGN accretion disk, (3) a spherical stellar cluster, (4) an anisotropic (flattened) cluster of BHs, and (5) BHs and stars in the AGN disk. We perform numerical simulations to follow the evolution of BHs during this AGN phase, including the formation and orbital evolution of binaries.

according to analytical formulas as summarized in Figure 2 and illustrated visually in Figure 3.

Our model includes physical processes due both to the presence of gas and to multibody dynamical interactions, as follows. For the interaction with gas, the radial positions of all BHs evolve in response to (i) type I/II migration torques by the AGN disk (Section 3.3.2), and the velocities of all BHs relative to the local AGN disk decrease due to (ii) the accretion torque (Section 3.3.4) and (iii) gas dynamical friction in the AGN disk (Section 3.3.3). For binaries of stellar-mass BHs, the separation evolves due to gas dynamical friction by the AGN disk and due to type I/II migration torque by a small circumbinary disk that forms within the Hill sphere of the binary. We also account for dynamical interactions with single stars and BHs and BH binaries: the binaries' separations and velocities evolve due to binary–single interactions (Section 3.3.5), and the velocities of all BHs additionally evolve due to scattering (Section 3.3.6). For dynamical interactions, we ignore the BHs in the spherical cluster, as they are greatly outnumbered by stars in the cluster, but we include both stars and BHs in the disk component. We

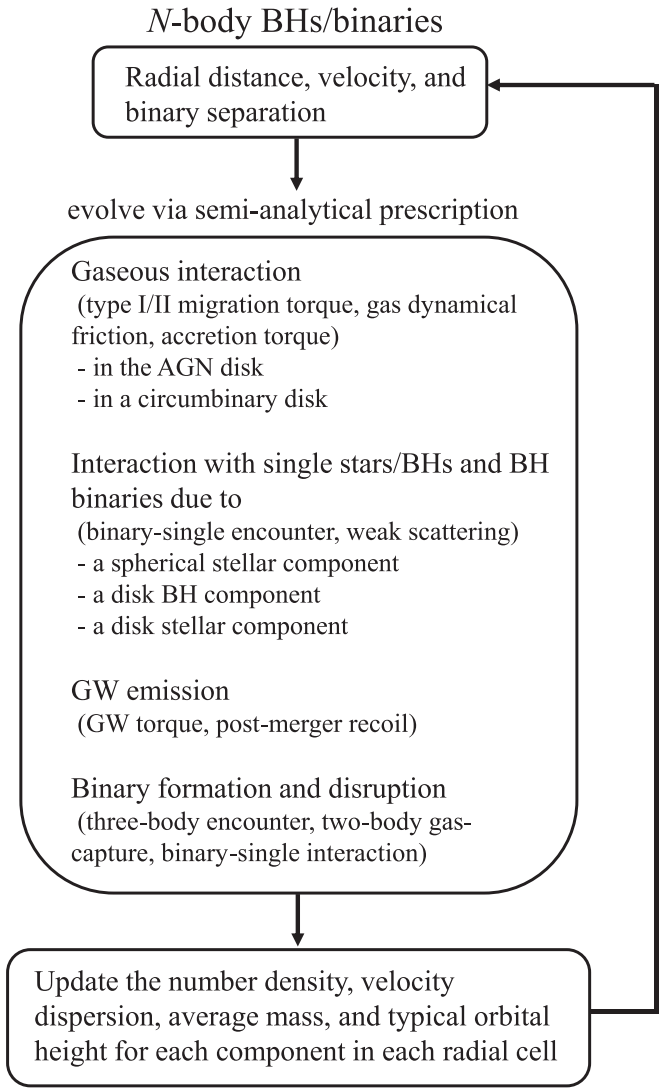

Figure 2. Schematic diagram for following the evolution of the BH population in our model, including both single and binary BHs. The N-body simulation keeps track of these individual objects (starting with 2×10^4 BHs and 1.5×10^3 binaries in our fiducial model). Single BHs are characterized by their radial position (r_i) from the central SMBH and by their velocity ($\boldsymbol{v}_i$) relative to the local Keplerian value. Binaries are similarly characterized by their center-of-mass position (r_j) and velocity ($\boldsymbol{v}_j$), and additionally by their orbital separation (s_j). These variables are updated via semianalytic prescriptions in each "N-body" time step, due to multiple processes as listed in the diagram.

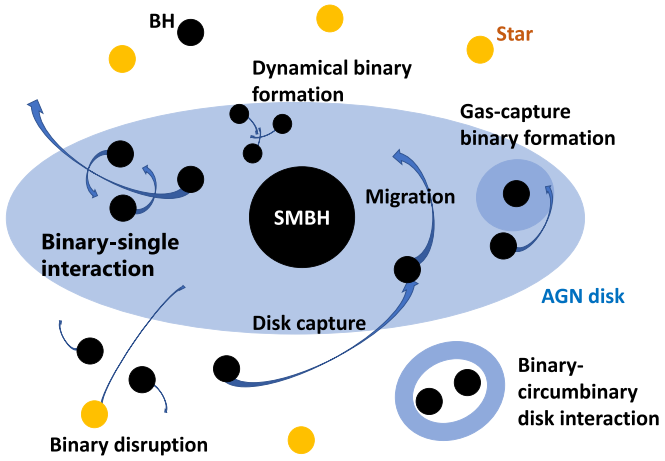

Figure 3. Schematic diagram illustrating the mechanisms affecting the BH population and driving binary formation and evolution. See Section 2 and Figure 2 for an overview and Section 3 for numerical details.

also account for GW emission, which reduces the binary separation rapidly once the binary is sufficiently tight. For simplicity, eccentricity evolution is ignored and orbits around the SMBH and binary orbits are both assumed to be circular.

To model the orbits of merged BHs, a recoil velocity is added to the BH remnant due to anisotropic GW radiation (Section 3.3.10). The small mass loss during mergers due to GW radiation is taken into account assuming zero BH spins.

In this study, we ignored several processes for simplicity. These include the exchange of binary components during binary–single interaction, the formation and evolution of stellar binaries, radial migration of stars due to the torque of the AGN disk, evolution of compact objects other than BHs, the Kozai–Lidov effect of the SMBH or a third stellar-mass object on binaries, dynamical relaxation processes, counterrotating BHs or stars in the AGN disk (Ivanov et al. 2015; Sánchez-Salcedo et al. 2018), stellar evolution, supernova feedback, binary mass transfer, and the possible presence of massive perturbers like an SMBH companion and/or IMBHs. A few IMBHs, if present, may efficiently disrupt most BH binaries which may greatly reduce the merger rates (Deme et al. 2020).

The above model allows us to describe the time evolution of the binary BH population in a self-consistent and flexible way. It extends the simplified prescriptions of previous studies of stellar-mass BH binary mergers in AGN disks and creates a self-consistent, one-dimensional N-body simulation that includes the time-dependent formation, disruption, and evolution of binaries in AGNs. We use this method to estimate the contribution of binaries formed during the AGN phase. We confirm previous suggestions (Secunda et al. 2019; Yang et al. 2019a) that repeated mergers are frequent in AGN disks, although in contrast with these previous works, in our models repeated mergers occur due to efficient binary formation and evolution processes well outside the "migration traps."

3. Method

Here we describe in detail the method and the initial conditions adopted in this study. Table 1 lists the definition of variables that appear in this paper.

3.1. Stellar-mass BHs, Stars, and AGN Disk

In this section, we describe the initial condition in the calculations.

3.1.1. Initial BH and Stellar Distributions

We simulate the evolution of N-body particles representing stellar-mass BHs. We assume that these are initially distributed according to

$$\frac{dN_{\rm BH,ini}(r)}{dr} \propto r^{\gamma_\rho}, \tag{1}$$

where $N_{\rm BH,ini}(r)$ labels the total initial number of BHs within a distance r from the central SMBH, and γ_ρ is a power-law index. Theoretically, γ_ρ is expected to be between ~ -0.5 and 0.25 for plausible mass functions for spherically symmetric systems (Freitag et al. 2006; Hopman & Alexander 2006; Alexander & Hopman 2009; Keshet et al. 2009; O'Leary et al. 2009). In our fiducial model, we adopt $\gamma_\rho = 0$ between $r_{\rm in,BH} \leqslant r \leqslant r_{\rm out,BH}$, where $r_{\rm in,BH} = 10^{-4}$ pc and $r_{\rm out,BH} = 3$ pc.

We set the total stellar mass within 3 pc to be

$$M_{\rm star,3pc} = 10^7\,M_\odot \tag{2}$$

(Feldmeier et al. 2014) as the fiducial value. The minimum and maximum masses for progenitor stars are assumed to be 0.1 and 140 $M_\odot$, respectively. The BH mass is determined through the relations between the progenitor mass ($m_{{\rm star},i}$) and the BH mass ($m_{{\rm BH},i}$) of

$$m_{{\rm BH},i} = \begin{cases} \frac{m_{{\rm star},i}}{4} & \text{for } 20\,M_\odot < m_{{\rm star},i} < 40\,M_\odot, \\ 10\,M_\odot & \text{for } 40\,M_\odot < m_{{\rm star},i} < 55\,M_\odot, \\ \frac{m_{{\rm star},i}}{13} + 5.77\,M_\odot & \text{for } 55\,M_\odot < m_{{\rm star},i} < 120\,M_\odot, \\ 15\,M_\odot & \text{for } 120\,M_\odot < m_{{\rm star},i} < 140\,M_\odot, \end{cases} \tag{3}$$

which roughly matches population synthesis simulation results in Belczynski et al. (2010) for their model with solar metallicity and a weak wind.

Because observational studies (Bartko et al. 2010; Lu et al. 2013) suggest a top-heavy initial mass function (IMF) for stars in the Galactic center region, we investigate IMFs:

$$\frac{dN}{dm_{\rm star}} \propto m_{\rm star}^{-\delta_{\rm IMF}}, \qquad 0.1M_\odot \leqslant m_{\rm star} \leqslant 140M_\odot, \tag{4}$$

with $\delta_{\rm IMF}$ in the range 1.7–2.35. We set the fiducial value to be $\delta_{\rm IMF} = 2.35$, yielding an average stellar mass $\bar{m}_{\rm star} = 0.36\,M_\odot$ and initial number of BHs $N_{\rm ini,BH} = 2.0 \times 10^4$. For $1.7 \leqslant \delta_{\rm IMF} \leqslant 2.35$, $\bar{m}_{\rm star}$ and $N_{\rm ini,BH}$ vary between 0.36–1.78 $M_\odot$ and 2.0×10^4–1.0×10^5.

The simulation tracks the velocity of particles relative to the local Keplerian AGN disk in the plane of the disk, $v_{xy,k}$, and perpendicular to it, $v_{z,k}$, at the point where the orbit crosses the equatorial plane, where k is the particle index. The direction of $v_{xy,k}$ is assumed to be axisymmetrically random in the xy plane. The x, y, and z components of the velocity of each BH relative to the local disk are initially drawn randomly from a Gaussian distribution with dispersion of $\beta_v v_{\rm Kep}(r)/\sqrt{3}$ and zero mean. Here $v_{\rm Kep}(r) = \{G[M_{\rm SMBH} + M_{\rm star}(<r)]/r\}^{1/2}$ is the Keplerian orbital velocity at the distance r from the central SMBH,

$M_{\rm star}(<r)$ is the stellar mass within r, and $\beta_{\rm v}$ is a parameter that determines the initial velocity dispersion of BHs. In our fiducial model, we set $\beta_{\rm v}=0.2$. Because this is with respect to the comoving Keplerian frame, it corresponds to a net rotation for the preexisting BH component, which is consistent with observational (e.g., Trippe et al. 2008; Feldmeier et al. 2014, 2015; Yelda et al. 2014) and theoretical (Kocsis & Tremaine 2011b; Szolgyen & Kocsis 2018) suggestions that massive stars in the central region of $\lesssim$1 pc have some degree of net rotation.

We assume that some fraction of BHs are initially in binaries as follows. Spectroscopic observations show that the binary fraction of O stars in the Galactic field is ∼0.7 (Sana et al. 2012), but the binary fraction of OB/WR stars in the Galactic center is estimated to be only ∼0.3 (Pfuhl et al. 2014). We define the corresponding initial "preexisting" BH binary fraction $f_{\rm pre}$ as the number of BH binaries over the total number of (single+binary) BHs. Belczynski et al. (2004) found that if the binary fraction of progenitor stars is 50% (2/3 of stars are in binaries), the binary fraction of BHs is ∼10% as a result of stellar evolution due to supernova kicks and mergers during the common-envelope and Roche-lobe overflow phases. In the Galactic center, binary disruption due to soft-binary–single interactions may further decrease the BH binary fraction (see also Stephan et al. 2016). We adopt $f_{\rm pre}=0.15$ in our fiducial model.

We draw the initial separation of preexisting binaries randomly from a log-flat distribution following Abt (1983). The minimum separation $R_{\rm min}$ has large uncertainties because $R_{\rm min}$ is determined by common-envelope evolution, which is not well understood (Ivanova et al. 2013). For the fiducial value, we set $R_{\rm min}$ as the sum of the radii of the progenitor binary components. We compute the stellar radius as (Torres et al. 2010)

$$R_{{\rm star},i}=R_\odot\left(\frac{m_{{\rm star},i}}{M_\odot}\right)^{1/2}. \tag{5}$$

We set the maximum binary separation $R_{\rm max}$ to $10^5\,R_\odot$ following binary evolution models (e.g., Belczynski et al. 2008; Kinugawa et al. 2014). We further assume that binaries that are soft compared to the local spherical stellar component (Section 3.3.5) are promptly disrupted prior to the AGN phase. The timescale of the disruption of binaries is ∼300 Myr at $r_j\lesssim 0.01$ pc and ∼20 Myr at $r_j=3$ pc (Equation (7.173) of Binney & Tremaine 2008), in which we use the velocity dispersion, the density, and the average stellar mass for the spherical stellar component in the fiducial setting of our simulations (Equation (6)), the Coulomb logarithm is assumed to be 10, each BH binary component is assumed to have a mass of 5 $M_\odot$, and the binary separation is the maximum of the hard–soft boundary (Equation (102) below) and the separation at which a binary merges within the Hubble time (Equation (103) below). Due to the disruption of binaries prior to the AGN phase, the binary fraction at the beginning of the simulation is reduced to ∼7%. Note that this value varies according to the IMF, the total stellar mass, and the mass of the SMBH (see Section 4.4 below).

3.1.2. Stellar and BH Components

We categorize stars and BHs by whether they reside within or orbit outside of the AGN disk. These components are referred to as the disk stellar, the spherical stellar, the disk BH, and the anisotropic BH components (Figure 1). We assume that stars are initially spherically distributed, and the velocity of stars follow a Maxwell–Boltzman distribution with no net rotation, while BHs are initially distributed with some degree of net rotation (see justification below). Due to the interaction with the AGN disk and star formation in the outer regions of the AGN disk, the number of BHs and stars in the AGN disk gradually increase. As a result, the BH and stellar density within the AGN disk rise. Thus, the BH and stellar disk components form during the AGN phase (Figure 1). Because the mass outside of the AGN disk is dominated by stars (i.e., the spherical stellar component), we ignored the interaction of BHs/binaries with BHs orbiting outside of the AGN disk (i.e., the anisotropic BH component) in the fiducial model for simplicity (but investigate their importance below, in model 37).

To compute the rates of various density- and velocity-dependent processes (see Sections 3.3.5–3.3.8 below), we calculate the number density ($n_{\rm c}$), the velocity dispersion ($\sigma_{\rm c}$), the average mass ($m_{\rm c}$), and the typical orbital height ($h_{\rm c}$) for each component in each radial cell in a grid. The spherical radial grid extends from $r_{\rm in}=10^{-4}$ to $r_{\rm out}=5$ pc, and is divided into $N_{\rm cell}=120$ cells uniformly on a log scale in the fiducial model. The dependence of results on $N_{\rm cell}$ is discussed in Section 4.4. We ignore the possible effects related to migration traps, which may exist at $\lesssim 9\times10^{-5}(M_{\rm SMBH}/4\times10^6\,M_\odot)$ pc for the model by Thompson et al. (2005; Bellovary et al. 2016), just outside of the simulated domain.

We set the time-independent physical quantities for the spherical stellar component in each cell to be

$$(m_{\rm c},\,n_{\rm c},\,\sigma_{\rm c},\,h_{\rm c})_{{\rm Sstar},l}=\left(\bar{m}_{\rm star},\,\frac{\rho_{\rm Sstar}(r_l)}{\bar{m}_{\rm star}},\,\frac{v_{\rm Kep}(r_l)}{\sqrt{3}},\,\frac{r_l}{\sqrt{2}}\right), \tag{6}$$

where $\bar{m}_{\rm star}$ is the average stellar mass in the spherical stellar component determined from the assumed IMF (Equation (4)), $v_{{\rm Kep},l}$ is the Keplerian velocity at the radius r_l of the geometric center of a cell l, and $\rho_{\rm Sstar}(r)$ is the density profile of the spherical stellar component. We adopt

$$\rho_{\rm Sstar}(r)=\left(\frac{M_{\rm star,3pc}}{4.3}\right){\rm pc}^{-3}\times\left(\frac{r}{0.3\ {\rm pc}}\right)^{-0.5}\left[1+\left(\frac{r}{0.3\ {\rm pc}}\right)^4\right]^{-0.325}, \tag{7}$$

chosen to match the observed stellar surface density distribution in the Galactic nucleus (Merritt 2010; Feldmeier et al. 2014), where $M_{\rm star,3\,pc}$ is given by Equation (2). The typical orbital height for the spherical stellar component $(h_{\rm c})_{{\rm Sstar},l}$ is set to $r_l/\sqrt{2}$ considering a uniform distribution in each spherical shell.

On the other hand, the quantities for the disk BH component in each cell are initialized as

$$(m_{\rm c},\, n_{\rm c},\, \sigma_{\rm c},\, h_{\rm c})_{{\rm DBH},l} = \left[\frac{\sum_{k\in{\rm DBH},l} m_k}{N_{{\rm DBH},l}},\, \frac{N_{{\rm DBH},l} r_l}{V_l h_{{\rm c,DBH},l}},\, \left(\frac{\sum_{k\in{\rm DBH},l} v_k^2}{3N_{{\rm DBH},l}}\right)^{1/2},\, \frac{r_l}{v_{\rm Kep}(r_l)}\left(\frac{\sum_{k\in{\rm DBH},l} v_{z,k}^2}{N_{{\rm DBH},l}}\right)^{1/2}\right], \quad (8)$$

which evolve with time, where DBH,l refers to the BH components which are within the AGN disk in the lth cell, $N_{{\rm DBH},l}$ is the number of single BHs and BH binaries within the AGN disk in cell l, $V_l = 4\pi r_l^2 \Delta r_l$ is the spatial volume of the lth spherical shell so that $h_l V_l / r_l$ is the spatial volume of the AGN disk in the lth cell, and Δr_l is the width of the lth cell. Note that we include the number of BH binaries in $N_{{\rm DBH},l}$. For the binaries, m_k and v_k refer to the total mass and center of mass velocity of the kth binary relative to the Keplerian velocity in Equation (8). The average mass $m_{{\rm c,DBH},l}$ and the velocity dispersion $\sigma_{{\rm c,DBH},l}$ of the disk BH component in a cell l are given by the average of m_k and the rms of $v_k/\sqrt{3}$ of BHs, respectively.

We assume that when $h_k < h_{{\rm AGN},l}$, the kth object is embedded in the AGN disk, where $h_k = v_{z,k} r_k / v_{\rm Kep}$ is the typical height of orbital motion for the kth object and $h_{{\rm AGN},l}$ is the height of the AGN disk at r_l ($h_{{\rm AGN},l}$ is derived in Section 3.1.3). We assume that the disk BH component rotates in the same sense as the AGN disk, so $\sigma_{\rm c} = 0$ means that BHs in the disk corotate with the Keplerian gas.

In model 37, we take into account interactions with BHs outside the AGN disk (i.e., the anisotropic BH component). Each quantity for this new component is calculated in the same way as in Equation (8), but including BHs outside the AGN disk ($h_k > h_{{\rm AGN},l}$).

The statistical quantities of the disk stellar component in each cell are calculated as

$$(m_{\rm c},\, n_{\rm c},\, \sigma_{\rm c},\, h_{\rm c})_{{\rm Dstar},l} = (\bar{m}_{\rm star},\, n_{{\rm Dstar},l},\, \sigma_{{\rm c,DBH},l},\, h_{{\rm c,DBH},l}), \quad (9)$$

where Dstar,l refers to the stellar component embedded within the AGN disk in the lth cell. We ignore the accretion and migration of stars captured by the AGN disk for simplicity. This is a conservative assumption for the merger fraction as it ignores the possibility for migration to increase the stellar density in the inner regions which would facilitate BH mergers through frequent binary–single interactions. Because we do not calculate the evolution of stars, we assume that their velocity dispersion and scale height match that of the BH disk component, given by Equation (8). The density of the disk stellar component is calculated from the number of stars by simply assuming that the stars reside in the same volume as the disk BH component ($V_l h_{{\rm c,DBH},l}/r_l$). The number of stars in the disk stellar component is calculated considering three factors. First, we assume that stars form at a rate $\dot{\Sigma}_*$ in the outer regions of the AGN disk (Figure 4, Section 3.1.3). We ignore the evolution of newly formed stars. Second, we assume that spherically distributed stars are captured in the AGN disk at the rate estimated in Section 3 of Bartos et al. (2017). Bartos et al. (2017) estimated the timescale on which objects are captured in the AGN disk based on the torque due to Bondi–Hoyle–Lyttleton accretion during crossing of the AGN disk. In our simulation, we calculate the critical inclination angle of stellar orbits with respect to the AGN disk at which the alignment timescale (Equation (11) of Bartos et al. 2017) becomes the same as the elapsed time. We assume that the inclination of stars $\cos i$ is distributed uniformly between -1 and 1 as in Bartos et al. (2017) and derive the fraction of stars whose inclination is smaller than the critical inclination angle. We assume that gas within the Bondi–Hoyle–Lyttleton radius is captured by a star, and we ignore cases in which the stellar radius is larger than the Bondi–Hoyle–Lyttleton radius, which is realized for $v_i \gtrsim 300\ {\rm km\ s^{-1}} (m_{{\rm star},i}/0.36\ M_\odot)^{1/2}$. In this way, we calculate the number of stars captured in the AGN disk in each step. Third, we reduce the number of stars in the disk stellar component in the lth cell hosting the binary by one for each BH binary that experiences a hard binary–stellar single interaction with objects in the disk stellar component. This reflects the fact that the recoil kick following a hard BH binary–single interaction with the typical low-mass stars is so large that the interacting stars are usually kicked out from the AGN disk in the vertical direction.

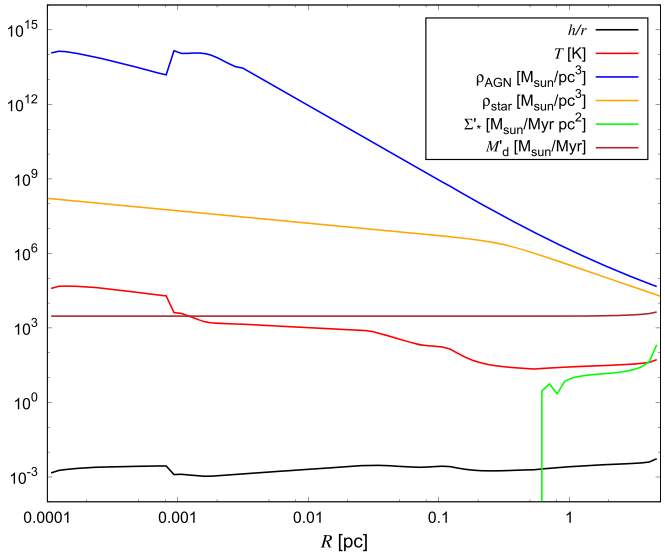

Figure 4. Physical quantities for the adopted disk model as a function of the distance r from the SMBH. The colored lines represent the disk height over the distance $h_{\rm disk}/r$ (black), the midplane temperature T (red), the gas density $\rho_{\rm AGN}$ (blue), the background stellar density (orange), the star formation surface density $\dot{\Sigma}_*$ (green), and the accretion rate $\dot{M}_{\rm d}$ (brown). Units are $M_\odot$, Myr, K, and pc.

3.1.3. AGN Disk

We employ the AGN accretion disk model proposed by Thompson et al. (2005). In the fiducial model, we set the SMBH mass to $M_{\rm SMBH} = 4 \times 10^6 M_\odot$ and the accretion rate from the outer boundary of $r_{\rm out} = 5$ pc to be $\dot{M}_{\rm out} = 0.1\, \dot{M}_{\rm Edd}$, where $\dot{M}_{\rm Edd} = L_{\rm Edd}/(c^2 \eta_{\rm c})$ is the Eddington accretion rate, $L_{\rm Edd}$ is the Eddington luminosity, c is the light speed, and $\eta_{\rm c}$ is the radiative efficiency. We adopt $\eta_{\rm c} = 0.1$ assuming a

standard thin-disk model. We adopt the opacity model given by Bell & Lin (1994), which gives the opacity as a function of temperature and density. Following the fiducial values in Thompson et al. (2005), we assume the pressure ratio parameter $\xi = 1$. We improve the calculation of the conversion efficiency ϵ of star formation to radiation in Thompson et al. (2005) by taking into account the limitations due to the AGN and stellar lifetimes (see Appendix A for details). This reduces ϵ by a factor of $\sim$4 to $\epsilon = 1.5 \times 10^{-4}$ for the fiducial model, and ϵ varies between 1.5×10^{-4} and 7.7×10^{-4} according to the IMF exponent ($-2.35 \leqslant -\delta_{\rm IMF} \leqslant -1.7$). We assume that the efficiency of angular momentum transport due to global torque in the outer region is $m_{\rm AM} \sim 0.1$–0.2 as suggested by Thompson et al. (2005). In the inner region, we adopt the α model for angular momentum transport, in which the alpha parameter is $\alpha_{\rm SS} = 0.1$ (King et al. 2007; Bai & Stone 2013). In the transition between the inner and outer regions, the degree of angular momentum transport is adjusted to keep the Toomre parameter at $Q = 1$.

We assume a locally isothermal equation of state to calculate the sound speed of the AGN disk as $c_s = (p/\rho_{\rm gas})^{1/2}$, where p is the total gas+radiation pressure, and $\rho_{\rm gas}$ is the local density of a gas disk. The viscosity is given by $\nu = r v_r/(d\ln\Omega/d\ln r)$, where v_r is the radial velocity and Ω is the angular velocity of the gas disk, which is rotating around the enclosed mass of the SMBH and stars (Equation (7)). In the α prescription, the viscosity ν is assumed to be proportional to the total pressure, $\nu = \alpha_{\rm SS} c_s^2/\Omega$. The surface density of the gas disk is calculated using the radial velocity and the gas inflow rate ($\dot{M}$) as $\Sigma_{\rm disk} = \dot{M}/(2\pi r v_r)$.

The AGN disk properties are shown in Figure 4. The outer region ($\gtrsim$1 pc) is stabilized by radiation pressure and supernovae from in situ formed stars. Therefore, the star formation rate is determined by the disk model, which depends on the mass of the SMBH, the accretion rate, and efficiency parameters through Equations (C1)–(C12) of Thompson et al. (2005). The green line in Figure 4 represents the surface density of the star formation rate $\dot{\Sigma}_*$. The star formation rate and BH formation rate surface densities are given by $f_{\rm star} \times \dot{\Sigma}_*$ and $f_{\rm BH} \times \dot{\Sigma}_*$, respectively, where $f_{\rm star}$ and $f_{\rm BH}$ are the ratio of the mass of stars with mass less than 20 $M_\odot$ and all stellar-mass BHs to the mass of all stars at formation, respectively. BHs continuously form at this rate in our simulations, and the number of BHs formed within 100 Myr is $\sim$7% of the initial number of BHs in the fiducial model. The accretion disk model with large size and star formation is motivated by several observations, which are the early enhancement of metallicity in disks (Artymowicz et al. 1993; Xu et al. 2018; Novak et al. 2019), long-timescale transients in AGNs (Graham et al. 2017), and supernovae found in the vicinity of an AGN (Pérez-Torres et al. 2010).

Based on Equation (3), $f_{\rm BH}$ varies from 0.016 to 0.092 according to the IMF ($1.7 \leqslant \delta_{\rm IMF} \leqslant 2.35$), and $f_{\rm BH} = 0.016$ in the fiducial model. We set the velocity of newly formed BHs relative to the local AGN motion v_k to be the sonic velocity of the AGN disk at their location. This is motivated by numerical simulations suggesting that the scale height of newly born stars within an AGN disk is roughly similar to the thickness of the AGN disk (Nayakshin et al. 2007). In this study, BHs form immediately during star formation, ignoring the lifetime of the progenitor stars for simplicity. We assume that the mass distribution and the binary fraction of in situ formed BHs are the same at formation as those of the preexisting BHs described above.

3.2. Formation, Destruction, and Orbital Evolution of Binaries

In this study, we do not follow the evolution of individual stars, but only track their average statistical properties in a grid as explained in Section 3.1.2 for both the spherical and the disk stellar components. However, we follow the orbital parameters of individual BHs and BH binaries as follows.

For clarity, we use the indices i and j in this paper exclusively to label a single BH and a BH binary, respectively. We use the index k to denote either a single BH or a BH binary. For single BHs, we characterize their orbits with their orbital radius around the SMBH r_i, the magnitude of their z-direction velocity $v_{z,i}$, and their xy-direction velocity $v_{xy,i}$ at $z = 0$. Here, $v_i = (v_{xy,i}^2 + v_{z,i}^2)^{1/2}$ is the velocity relative to the local Keplerian velocity of a circular orbit with $z = 0$. Given $v_{z,i}$, the maximum height of the orbit is $h_i = r_i v_{z,i}/v_{\rm Kep}(r_i)$. For binaries, we follow their radial position r_j, their center-of-mass velocity components $v_{xy,j}$ and $v_{z,j}$, and their binary separation s_j. The position, velocity, and separation of BHs evolve by interacting with gas and/or stellar and BH components (Figure 3). In this paper, we do not consider the evolution of the binary eccentricity (e_j), and assume $e_j = 0$ for all binaries.

We incorporate the effects of gas dynamical friction, GW radiation, weak gravitational scattering, binary–single interaction, type I/II migration torque, binary formation via three-body encounter and via gas-capture mechanism, binary disruption, and star formation.

The velocity $\boldsymbol{v}_i = (v_{xy,i}, v_{z,i})$ of a single BH evolves via the equation of motion (Papaloizou & Larwood 2000)

$$\frac{d\boldsymbol{v}_i}{dt} = \boldsymbol{a}_{{\rm acc},i} + \boldsymbol{a}_{{\rm GDF},i} + \boldsymbol{a}_{{\rm WS},i}, \tag{10}$$

where $\boldsymbol{a}_{{\rm acc},i}$ is the acceleration due to the accretion torque (Section 3.3.4), gas dynamical friction $\boldsymbol{a}_{{\rm GDF},i}$ (Section 3.3.3), and weak gravitational scattering $\boldsymbol{a}_{{\rm WS},i}$ (Section 3.3.6).

For BH binaries, the center-of-mass velocity $\boldsymbol{v}_j$ changes due to all of these processes and additionally due to binary–single interactions as

$$\frac{d\boldsymbol{v}_j}{dt} = \boldsymbol{a}_{{\rm acc},j} + \boldsymbol{a}_{{\rm GDF},j} + \boldsymbol{a}_{{\rm WS},j} + \boldsymbol{a}_{{\rm BS},j}, \tag{11}$$

where $\boldsymbol{a}_{{\rm BS},j}$ is the acceleration due to binary–single interactions ($\boldsymbol{a}_{{\rm BS},j}$).

Bartos et al. (2017) proposed that the binary separation decreases due to gas dynamical friction in an AGN disk, type I/II torque from a circumbinary disk, and GW radiation after the capture of close-in binaries in the smooth disk in $\leqslant$0.01 pc. Stone et al. (2017) considered mergers from binaries formed in situ at the unstable part of the disk at larger radii of $\sim$ parsec. Stone et al. (2017) find that binary–single interaction with the disk stellar component also hardens the binary separation. In this study, we incorporate these effects into the evolution of the binary separation as

$$\frac{ds_j}{dt} = \left.\frac{ds_j}{dt}\right|_{\rm GW} + \left.\frac{ds_j}{dt}\right|_{\rm gas} + \left.\frac{ds_j}{dt}\right|_{\rm BS}, \tag{12}$$

where the three terms on the right-hand side are the evolution rates for the binary separation due to GW radiation

(Section 3.3.1), gaseous torque (Sections 3.3.2 and 3.3.3), and binary–single interaction, respectively.

Single and binary BHs migrate radially toward the SMBH due to the gaseous torque of the AGN disk, given by the type I or type II torque formula (Section 3.3.2):

$$\frac{dr_k}{dt} = \left.\frac{dr_k}{dt}\right|_{\rm type\ I/II}. \tag{13}$$

Furthermore, binaries form and are disrupted according to

$$\frac{dN_{\rm bin}}{dt} = \sum_i P_{\rm 3bbf,i} + \sum_i P_{\rm gas,i} + K_{\rm dis}, \tag{14}$$

where $P_{\rm 3bbf,i}$ is the binary formation rate by three-body encounter (Section 3.3.7), $P_{\rm gas,i}$ is the binary formation rate by gas-capture mechanism (Section 3.3.8), and $K_{\rm dis} = dN_{\rm bin}/dt|_{\rm dis} < 0$ is the binary disruption rate. Binaries are disrupted in the simulation when the binary separation s_j becomes larger than the Hill radius of a binary with respect to the SMBH,

$$r_{{\rm Hill},j} = r_j\left(\frac{m_j}{3M_{\rm SMBH}}\right)^{1/3}. \tag{15}$$

The terms in Equations (10)–(14) are described in the next section, Section 3.3. These equations are calculated separately using the local statistical quantities describing the stellar environment in each shell l.

3.3. Individual Processes

Here we describe in detail the prescription adopted for each of the mechanisms included in our simulations.

3.3.1. Gravitational Wave Radiation

When the binary separation is small, GW radiation strongly decreases the binary separation. The hardening rate via GW radiation is given as

$$\frac{ds_j}{dt}|_{\rm GW} = -\frac{64}{5}\frac{G^3 m_{j_1} m_{j_2}(m_{j_1}+m_{j_2})}{c^5 s_j^3} \tag{16}$$

assuming zero eccentricity (Peters 1964), where m_{j_1} and m_{j_2} are the masses of the primary and secondary BHs in the jth binary, respectively.

3.3.2. Type I and II Migration

Objects in a gaseous disk interact gravitationally with nearby gas, resulting in radial migration. When the gravitational torque exerted by an object within the disk exceeds the viscous torque of gas, a gap opens in the disk around the object (e.g., Ward 1997; Crida et al. 2006). When a gap does not open around the object, the object migrates due to torques from the Lindblad and corotation resonances on the type I migration timescale (e.g., Ward 1997; Tanaka et al. 2002; Paardekooper et al. 2010; Baruteau et al. 2011) of

$$t_{\rm type\ I} \simeq \frac{1}{2f_{\rm mig}}\left(\frac{M_{\rm cen}}{M_{\rm sat}}\right)\left(\frac{M_{\rm cen}}{\Sigma_{\rm disk} r^2}\right)\left(\frac{h_{\rm disk}}{r}\right)^2 \Omega^{-1}, \tag{17}$$

where $f_{\rm mig}$ is a dimensionless factor depending on the local temperature and density profiles (see Paardekooper et al. 2010; Baruteau et al. 2011), $h_{\rm disk}$ is the half-thickness of the disk, $M_{\rm cen}$ and $M_{\rm sat}$ are the central and satellite object mass, respectively, and $\Sigma_{\rm disk}$ is the surface density of the disk.[3] We calculate the evolution in the range $r \geqslant r_{\rm in} \sim 10^3 R_g$, where $f_{\rm mig}$ remains positive and its variation is not significant. We set $f_{\rm mig} = 2$ in the fiducial model, which is the typical value found numerically by Kanagawa et al. (2018). If a gap opens in a disk around an object, the object migrates due to the torque of the gas approaching the gap boundary on a timescale related to the viscosity. This process is the so-called type II migration (e.g., Lin & Papaloizou 1986; Ward 1997; Ida & Lin 2004; Edgar 2007; Haiman et al. 2009; Duffell et al. 2014).

Recent hydrodynamic simulations (Duffell et al. 2014; Durmann & Kley 2015; Kanagawa et al. 2018) have shown that even when the torque from a BH exceeds the viscous torque of gas, the gas is able to pass through the gap. Duffell et al. (2014) and Kanagawa et al. (2018) show that the migration timescale even for a massive migrator is given by the type I migration timescale with a reduced gas surface density in the gap ($\Sigma_{\rm disk,min}$),

$$t_{\rm type\ I/II} = \frac{\Sigma_{\rm disk}}{\Sigma_{\rm disk,min}} t_{\rm type\ I}. \tag{18}$$

Fung et al. (2014) and Kanagawa et al. (2015) show that

$$\Sigma_{\rm disk,min} = \Sigma_{\rm disk}/(1+0.04K), \tag{19}$$

where $K = (M_{\rm sat}/M_{\rm cent})^2 (h_{\rm disk}/r)^{-5}\alpha_{\rm eff}^{-1}$, and $\alpha_{\rm eff} = \nu/(c_s h_{\rm disk})$ is the effective α parameter.

We calculate the migration rate of stellar-mass BHs within the AGN disk as

$$\frac{dr_k}{dt}|_{\rm type\ I/II} = -\frac{r_k}{t_{\rm type\ I/II}} p_{{\rm disk},k}, \tag{20}$$

where $p_{{\rm disk},k}$ is the fraction of time that the kth object spends in the disk along its orbit around the SMBH, which we calculate as

$$p_{{\rm disk},k} = \begin{cases} 1 & \text{for } h_k < h_{\rm disk}(r_k), \\ \frac{2}{\pi}\arcsin\left[\frac{h_{\rm disk}(r_k)}{h_k}\right] & \text{otherwise} \end{cases}, \tag{21}$$

assuming that the time spent inside the AGN disk is approximated by the ratio of the scale height of the disk and the BH's orbit. To calculate the migration rate, we substitute $h_{{\rm AGN},l}$ into $h_{\rm disk}$ in Equation (17). To reduce the computational cost, we use quantities at the center of each cell r_l in Equations (17)–(18). For comparison, we also investigate cases in which migration by type I/II torque does not operate, because the migration of BHs is not well understood due to the complexity of the effects of N-body migrators (Broz et al. 2018), feedback from BHs (e.g., del Valle & Volonteri 2018; Regan et al. 2019), and inhomogeneities in the turbulent accretion disk (Laughlin et al. 2004; Baruteau & Lin 2010).

Due to the torques exerted by the BHs, the gas density is reduced near each BH according to Equation (19). We take into account this reduction when we use gas dynamical friction

[3] It has been argued that $f_{\rm mig}$ may change sign in the inner region of the disk and BHs may migrate outward (Bellovary et al. 2016). The region where this may occur, around ~40–600 $R_g \sim 8\times10^{-6}$–10^{-4} pc$(M_{\rm SMBH}/4e6\ M_\odot)$, is not included in our simulated domain. Here, $R_g = GM_{\rm SMBH}/c^2$ is the gravitational radius of the SMBH.

(Section 3.3.3), gas accretion (Section 3.3.4), and the gas-capture mechanism (Section 3.3.8). In these mechanisms, when a BH is in the AGN disk, we use the local gas density of the AGN disk around each BH as

$$\rho_{\rm gas} = \rho_{{\rm AGN},l}\Sigma_{\rm disk,min}/\Sigma_{\rm disk}, \quad (22)$$

where $\rho_{{\rm AGN},l}$ is the unperturbed density of the AGN disk in the lth cell hosting a BH (Section 3.1.3). When a BH orbits outside of the AGN disk ($h_{z,k} > h_{{\rm AGN},l}$), we use $\rho_{\rm gas} = \rho_{{\rm AGN},l} = \Sigma_{{\rm disk},l}/(2h_{{\rm disk},l})$.

After gas is captured within the Hill's sphere of a binary, a circumbinary disk forms. This disk exerts a torque on the binary and changes its separation similar to type I/II migration. The naive expectation, detailed in several semianalytic treatments (see, e.g., Haiman et al. 2009 and references therein) has been that this process hardens the binary, on a timescale related to the viscous timescale in the disk, but modified by a factor involving the ratio of the mass of the binary and the disk. On the other hand, recent hydrodynamical simulations have found that an equal-mass binary is softened, rather than hardened, by the presence of a circumbinary gas disk (Miranda et al. 2017; Tang & MacFadyen 2017; Moody et al. 2019; Muñoz et al. 2019). At the present time, these simulations have many limitations: they treat equal-mass binaries on prescribed orbits, and disks with a specific viscosity parameter α, isothermal equation of state, and a temperature that is generically chosen (for numerical reasons) to be much higher than expected in real disks. They do not include radiation and cooling. Most of them are two dimensional and study circular binaries. As a result, it remains unclear how generic these simulations results are and whether they are applicable to real systems. For example, recent studies have found that unequal-mass binaries (Duffell et al. 2019), as well as binaries embedded in cooler disks (Tiede et al. 2020), are generally hardened by the circumbinary disk.

Here we consider several prescriptions (models 3–6). In the fiducial model, we follow the conclusions of the earlier semianalytic studies and assume that the binary can be hardened by the torque of a circumbinary disk, and the hardening timescale is given by Equation (20) by substituting s_j into r_k,

$$\frac{ds_j}{dt}|_{\rm type\ I/II} = -\frac{s_j}{t_{\rm type\ I/II}}p_{{\rm disk},k}. \quad (23)$$

Here, we substitute the BH binary component masses for $M_{\rm cen}$ and $M_{\rm sat}$, and use the angular velocity of the binary in Ω in Equation (20). If the Toomre parameter of the circumbinary disk satisfies $Q > 1$, it is stable against gravitational fragmentation. In this case, we calculate the surface density of a circumbinary disk using Equation (14) in Goodman & Tan (2004), in which we assign the opacity consistently following Bell & Lin (1994), and the disk temperature is given by the maximum of Equation (13) in Goodman & Tan (2004) and the temperature of the AGN disk at the position r_k. We assume that the gas pressure dominates over the radiation pressure for the circumbinary disk, which is a valid approximation for the radial range of the disk ($\gg\sim 10^9$ cm) we are interested in. When $Q < 1$, we reduce the surface density of the gas disk around a binary to satisfy $Q = 1$.

We assume that the accretion rate onto a binary or a single BH is given by the minimum of the Bondi–Hoyle–Lyttleton rate (Equation (29)) times $p_{{\rm disk},k}$ (Equation (21)) and Eddington-limited accretion,

$$\dot{m}_{{\rm acc},k} = \min\left(\dot{m}_{{\rm BHL},k}p_{{\rm disk},k}, \frac{\Gamma_{\rm Edd,cir}L_{{\rm Edd},k}}{\eta_{\rm c}c^2}\right), \quad (24)$$

where $\Gamma_{\rm Edd,cir}$ is the Eddington ratio, $L_{{\rm Edd},k}$ is the Eddington luminosity for a binary, and $\eta_{\rm c}$ is the energy conversion efficiency. We set $\Gamma_{\rm Edd,cir} = 1$ and $\eta_{\rm c} = 0.1$. The Eddington-limited accretion rate is motivated by regulation due to strong radiation pressure acting on dust grains for gas of around solar metallicity (Toyouchi et al. 2019), by a bipolar jet (Regan et al. 2019), and also by inefficient angular momentum transfer in circumbinary disks (Inayoshi et al. 2018; Sugimura et al. 2018).

We assume that the type I/II migration torque generated by a circumbinary disk surrounding the binary operates to shrink the binary separation only when the Bondi–Hoyle–Lyttleton radius $r_{{\rm BHL},k}$ is larger than the binary separation and otherwise the circumbinary disk does not exert a torque on the binary. Furthermore, we assume that a circumbinary disk is always aligned with the binary. This is justified as the alignment timescale of the disk with the binary is roughly given by the viscous timescale at the binary separation (e.g., Ivanov et al. 1999; Moody et al. 2019). This timescale is $r^2/\nu \sim \alpha_{\rm SS}^{-1}(h_{\rm disk}/r)^{-2}\Omega^{-1} \sim 10^5$ yr (Moody et al. 2019) for $s_j\sim$ astronomical unit, which is shorter than the timescale of evolution of binaries by type I/II torque from circumbinary disks ($\gtrsim$Myr).

3.3.3. Gas Dynamical Friction

When an object has a nonzero velocity relative to the ambient gas, gas dynamical friction reduces the relative velocity. In this manner, gas dynamical friction hardens binaries (Escala et al. 2004; Kim & Kim 2007; Baruteau et al. 2011) and damps the velocity dispersion of BHs and stars (Papaloizou & Larwood 2000; Tanaka et al. 2002) in the disk. For simplicity, we adopted the formulation for deceleration by gas dynamical friction derived by Ostriker (1999) as

$$a_{{\rm GDF},k}(v_k) = -\frac{4\pi G^2 m_k \rho_{\rm gas} p_{{\rm disk},k}}{v_k^2} f(v_k/c_s),$$
$$\text{where } f(x) = \begin{cases} \frac{1}{2}\ln\left(\frac{1+x}{1-x}\right) - x & \text{for } 0 < x < 1, \\ \frac{1}{2}\ln(x^2-1) + \ln\Lambda_{\rm gas} & \text{for } x > 1, \end{cases} \quad (25)$$

where $\ln\Lambda_{\rm gas}$ is the Coulomb logarithm for gas. We set $\ln\Lambda_{\rm gas} = 3.1$ referring the results in Chapon & Mayer (2013). For both binary hardening and velocity damping, we use the sonic velocity c_s from the disk model of Thompson et al. (2005, Section 3.1.3) at the geometric center of the cell l hosting BHs. Although these formulae apply for linear motion, they remain approximately correct for circular motion, despite the strong curvature and possible interaction of the pair of "wakes" in the binary case (Kim & Kim 2007). For binary hardening, we assume that gas dynamical friction operates while the binary is captured by the AGN disk ($h_k < h_{\rm AGN}$).

The AGN disk-capture timescale on which the initial supersonic velocity of an object $v_{\rm ini,k}$ decays due to crossing the disk due to gas dynamical friction is

$$t_{\rm capAGN} \equiv \int_0^{v_{\rm ini,k}} \frac{1}{a_{\rm GDF,k}(v_k) p_{\rm disk,k}} dv_k \simeq \frac{v_{\rm ini,k}^4 r_k}{16\sqrt{3}\pi G^2 \rho_{\rm gas} m_k h_{\rm AGN} v_{\rm Kep}} \sim 22\ {\rm Myr} \left(\frac{v_{\rm ini,k}}{0.2 v_{\rm Kep}}\right)^4 m_{k,10}^{-1} M_{\rm SgrA}^{3/2} r_{1\ {\rm pc}}^{-3/2} \times \left(\frac{h/r}{0.01}\right)^{-1} \rho_{\rm gas,6}^{-1}, \quad (26)$$

where we introduced the abbreviated labels $M_{\rm SgrA} = M_{\rm SMBH}/(4 \times 10^6\ M_\odot)$, $m_{k,10} = m_i/(10\ M_\odot)$, $r_{1\ {\rm pc}} = r_k/{\rm pc}$ $h/r = h_{\rm AGN}(r_k)/r_k$, $\rho_{\rm gas,6} = \rho_{\rm gas}/(10^6\ M_\odot\ {\rm pc}^{-3})$ (see Figure 4), where we assumed $f \sim 1$ in $a_{\rm GDF}$ for simplicity (see Equation (25)), and ignore the contribution of the stellar mass as $v_{\rm Kep} \sim (GM_{\rm SMBH}/r_k)^{1/2}$, which underestimates $t_{\rm capAGN}$ by $\sim$2 at $r_k = {\rm pc}$.

Similarly, we define the gas dynamical friction hardening timescale of a binary as

$$t_{\rm GDF,HS} \equiv \int_0^{v_{\rm HS}} dv/a_{\rm GDF} \simeq \frac{v_{\rm HS}^3}{12\pi G^2 \rho_{\rm gas} m_k} \sim 7\ {\rm Myr} \left(\frac{m_{\rm star}}{0.36\ M_\odot}\right)^{3/2} m_{k,10}^{-5/2} M_{\rm SgrA}^{3/2} r_{1\ {\rm pc}}^{-3/2} \rho_{\rm gas,6}^{-1}, \quad (27)$$

where $v_{\rm HS} = (\bar{m}_{\rm star}/m_k)^{1/2} v_{\rm Kep}(r)$ is the orbital velocity of a binary of mass m_k around its center of mass at which the binary is at the hard–soft boundary compared to the spherical stellar component.

During the hardening of binaries, it is not obvious whether type I/II torques by a circumbinary disk or gas dynamical friction by the AGN disk is a better description. Baruteau et al. (2011) showed that a binary in an AGN disk is hardened roughly on the timescale of gas dynamical friction. Derdzinski et al. (2019) find that the gas captured by a rapidly migrating BH within an AGN disk has almost no rotation with respect to the migrator, which suggests that gas torques may operate in the manner of dynamical friction (although this was demonstrated only for a single specific binary + disk configuration). As this issue has not been settled yet, we investigate several different prescriptions. In the fiducial model, we investigate the cases in which the binary-hardening rate due to gas interaction is given by

(i) the maximum value of the gas dynamical friction and the type I/II torque,
(ii) only the gas dynamical friction,
(iii) only the type I/II torque, or
(iv) zero (no hardening by gas interaction).

Park & Bogdanovic (2017) have shown that gas dynamical friction does not operate when the Bondi–Hoyle–Lyttleton radius ($r_{{\rm BHL},k} = Gm_k/(c_s^2 + v_k^2)$) is smaller than the size of a H II sphere ($r_{{\rm H\,II},k} = (3Q_{{\rm ion},k}/4\pi\alpha_{\rm rec,B} n_{\rm gas})^{1/3}$), where $\alpha_{\rm rec,B}$ is the case-B recombination coefficient for H (evaluated at $T = 10^4$ K), and $Q_{{\rm ion},k}$ is the ionizing photon number flux from the kth BH. This is caused by radiation feedback from a BH which diminishes the wake created by gas dynamical friction. The condition $r_{{\rm BHL},k} > r_{{\rm H\,II},k}$ can be rewritten as

$$\left(\frac{n_{\rm gas}}{2 \times 10^8\ {\rm cm}^{-3}}\right)^2 \left(\frac{m_k}{10\ M_\odot}\right)^2 \left(\frac{v_k}{10\ {\rm km\ s}^{-1}}\right)^{-6} > 1 \quad (28)$$

if we assume the Eddington accretion rate with the radiative efficiency $\eta_{\rm c} = 0.1$, $c_s \ll v_k$, and $Q_{\rm ion} \sim L_k/h\nu_{\rm p}$ with $h\nu_{\rm p} \sim 13.6$ eV, where h is Planck's constant, $\nu_{\rm p}$ is the average photon's frequency, and L_k is the luminosity from the kth BH. , the velocity of a BH exceeds twice the sound velocity in the H II region ($v_k \gtrsim 50\ {\rm km\ s}^{-1}$), gas dynamical friction is recovered (Park & Ricotti 2013; Park & Bogdanovic 2017). We set these conditions, $r_{{\rm BHL},k} > r_{{\rm H\,II},k}$ or $v_k > 50\ {\rm km\ s}^{-1}$, as criteria for gas dynamical friction to operate (also see a recent update considering dust emission by Toyouchi et al. 2020). In this work, we ignore kinetic feedback on gas dynamical friction, the effects of which are highly debated (Regan et al. 2019; Gruzinov et al. 2020; Li et al. 2020; Takeo et al. 2020).

3.3.4. Accretion Torque

As a BH crosses the AGN disk, it captures gas from the disk. The velocity of the BH decreases to satisfy conservation of momentum. The capture rate of gas on the kth BH during the passing of the AGN disk is given by the Bondi–Hoyle–Lyttleton rate:

$$\dot{m}_{{\rm BHL},k} = 4\pi r_{{\rm w},k} r_{{\rm h},k} \rho_{\rm gas} (c_s^2 + v_k^2)^{1/2}, \quad (29)$$

where

$$r_{{\rm w},k} = \min(r_{{\rm BHL},k},\ r_{{\rm Hill},k},\ r_{{\rm shear},k}) \quad (30)$$

and

$$r_{{\rm h},k} = \min(r_{{\rm w},k},\ h_{{\rm AGN},l}) \quad (31)$$

are the width and height of the gas bound to the kth BH, and

$$r_{{\rm shear},k} = \frac{Gm_k}{(r_{{\rm Hill},k}\Omega)^2} \quad (32)$$

is the typical radius over which gas motion changes due to the Keplerian shear of the AGN disk. Because $\boldsymbol{v}_k$ represents the relative velocity compared to the local rotating motion of the AGN disk, the acceleration by gas accretion torque is

$$\boldsymbol{a}_{{\rm acc},k} = -\boldsymbol{v}_k \frac{\dot{m}_{{\rm BHL},k}}{m_k} p_{{\rm disk},k}. \quad (33)$$

Although gas is considered to be captured at the rate given by Equation (29), the accretion rate onto the BH may be smaller than this value due to radiation feedback and the inefficiency of angular momentum transport. When we calculate the type I/II torque by a circumbinary disk, the accretion rate onto the binary is limited by the Eddington accretion rate (Equation (24)).

We adopt the gas accretion rate onto single BHs and binary BHs using Equation (24). On the other hand, when BHs are in binaries, we apportion the gas accretion rate between the binary

components as

$$\dot{m}_{\mathrm{acc},j_2} = \min\left[\frac{\lambda}{1+\lambda}\dot{m}_{\mathrm{BHL},j}p_{\mathrm{disk},j}, \frac{\Gamma_{\mathrm{Edd,cir}}L_{\mathrm{Edd},j_2}}{\eta_{\mathrm{c}}c^2}\right] \quad (34)$$

$$\dot{m}_{\mathrm{acc},j_1} = \min\left[\dot{m}_{\mathrm{acc},j} - \dot{m}_{\mathrm{acc},j2}, \frac{\Gamma_{\mathrm{Edd,cir}}L_{\mathrm{Edd},j_1}}{\eta_{\mathrm{c}}c^2}\right] \quad (35)$$

where λ is the ratio of the accretion rate onto the j_2th BH to that onto j_1th BH. We adopt the λ given by the fitting formula in Equation (1) of Kelley et al. (2019), based on the results of earlier hydrodynamical simulations (Farris et al. 2014).

3.3.5. Binary–Single Interaction

After a binary–single interaction, the binary separation changes depending on the hardness of the binary (e.g., Heggie 1975; Hills 1975; Binney & Tremaine 2008). We make two types of prescriptions for binary–single interaction according to whether a binary is hard, which satisfies $E_{\mathrm{b},j} > 3m_{\mathrm{c}}\sigma_{\mathrm{c}}^2/2$, or soft, where $E_{\mathrm{b},j} = Gm_{j_1}m_{j_2}/(2s_j)$ is the binding energy of the jth binary.

For soft-binary–single interactions, we employ the prescription for the average softening rate derived in Gould (1991),

$$\frac{ds_j}{dt}|_{\mathrm{BS}} = \frac{16}{3}\frac{Gn_{\mathrm{c}}m_{\mathrm{c}}s_j^2}{m_j\sigma_{\mathrm{c}}^3}\ln\Lambda\left(E_{\mathrm{b},j} - \frac{3}{2}m_{\mathrm{c}}\sigma_{\mathrm{c}}^2\right), \quad (36)$$

where $\Lambda = v_{\mathrm{bin},j}^2/\sigma_{\mathrm{c}}^2$ is the Coulomb factor and $v_{\mathrm{bin},j}$ is the relative velocity of components in the jth binary. We set $v_{\mathrm{bin},j} = (Gm_j/s_j)^{1/2}$ assuming $e_j = 0$. This equation assumes an isotropic Maxwell–Boltzmann distribution for the velocity of the background objects, which is approximately justified for the interaction with the spherical stellar component. We do not account for soft-binary–single interactions with the disk BHs and stellar components because most interactions with these components are not soft, due to the low relative velocity ($\sigma_{\mathrm{c}} < v_{\mathrm{Kep}}h_{\mathrm{AGN}}/r \lesssim Gm_j/r_{\mathrm{Hill},j}$).

On the other hand, for hard binary–single interactions, the hardening rate and the kick velocity after a binary–single encounter are given following Leigh et al. (2018). The binary-hardening rate is given by

$$E_{\mathrm{af},j} = E_{\mathrm{be},j} - (\Delta K_j + \Delta K_{\mathrm{c}}), \quad (37)$$

where $E_{\mathrm{be},j}$ and $E_{\mathrm{af},j}$ are the binding energies of the jth binary, i.e., $Gm_{j_1}m_{j_2}/(2s_j)$, before and after the binary–single interaction, and ΔK_j and ΔK_{c} are the changes in the kinetic energy of the jth binary and the escaping third body, respectively. Because $\Delta v_{\mathrm{BS},j}$ and $\Delta v_{\mathrm{BS,c}}$ are on order of $v_{\mathrm{bin},j}$ and v_j is typically smaller than $v_{\mathrm{bin},j}$, we approximate $\Delta K_j = \frac{1}{2}m_j\Delta v_{\mathrm{BS},j}^2$ and $\Delta K_{\mathrm{c}} = \frac{1}{2}m_{\mathrm{c}}\Delta v_{\mathrm{BS,c}}^2$, where $\Delta v_{\mathrm{BS},j}$ and $\Delta v_{\mathrm{BS,c}}$ are the kick velocities onto the jth binary and the third body, respectively. Due to the conservation of linear momentum, $\Delta \boldsymbol{v}_{\mathrm{BS},j} = -(m_{\mathrm{c}}/m_j)\Delta \boldsymbol{v}_{\mathrm{BS,c}}$. Here, $\Delta v_{\mathrm{BS,c}}$ is set to be the mode of the probability distribution for the kick velocity, which is determined by the energy and the total angular momentum L for the three-body system. Following Leigh et al. (2018), we sample L^2 uniformly from 0 to $(11.5/18)L_{\mathrm{max}}^2$ and set it to zero for the spherical and the disk components, respectively, where L_{max} is the maximum angular momentum of the three-body system (Equation (7.27) in Valtonen & Karttunen (2006). The assumption of the low angular momentum for the disk components is due to the low $v_{\mathrm{rel},j}$, and this assumption increases $\Delta v_{\mathrm{BS},c}$ for the disk components by a factor of $\sim$1.6 compared to $\Delta v_{\mathrm{BS},c}$ for the spherical cases with the typical angular momentum value of $(2/9)L_{\mathrm{max}}^2$ (Leigh et al. 2018). To determine the energy of the three-body system, we set $r_{\mathrm{Hill},j}$ and $v_{\mathrm{rel},j}$ to the initial third-body position and velocity relative to the binary center of mass, respectively. Hence, when a hard binary–single interaction occurs, the binary is hardened as

$$\frac{ds_j}{dt}|_{\mathrm{BS}} = \left(\frac{1}{E_{\mathrm{bf},j}} - \frac{1}{E_{\mathrm{af},j}}\right)\frac{Gm_{j_1}m_{j_2}}{2\Delta t}, \quad (38)$$

and a binary center of mass receives the kinetic energy ΔK_j due to a recoil kick. For the interaction with the disk BH component, we randomly choose the third body k', which is captured by the AGN disk ($h_{k'} < h_{\mathrm{AGN}}$) and resides in the same cell with the binary j, and set $m_c = m_{k'}$. We assign the third body a recoil kick given by ΔK_c. Even when the k'th object is a binary, we treat it as interaction with a single object with the mass $m_{k'}$. We assume that the direction of this kick velocity is random and isotropically distributed. Geller et al. (2019) verified that the binary evolution due to encounters calculated by this semianalytical approach matches the results from direct N-body simulations.

The timescale for the occurrence of a binary–single encounter is given by (e.g., Binney & Tremaine 2008)

$$t_{\mathrm{BS},j} = 1/(n_{\mathrm{c}}\sigma_{\mathrm{coll}}v_{\mathrm{rel},j}p_{\mathrm{c},j}), \quad (39)$$

where

$$v_{\mathrm{rel},j} = \max(\sqrt{3}\sigma_{\mathrm{c}}, v_j, v_{\mathrm{rel,mig},j}, v_{\mathrm{shear},j}) \quad (40)$$

represents the typical velocity of the third body relative to the center of mass for the binary j, σ_{coll} is the cross section, $v_{\mathrm{rel,mig},j}$ is the migration velocity of the binary relative to the third body, $v_{\mathrm{shear},j}$ is the shear velocity between the center of mass for the binary j and the third body, and $p_{\mathrm{c},j}$ is the fraction of time that the jth object spends within the scale height of each component along its orbit around the SMBH. We set $v_{\mathrm{shear},j} = p_{\mathrm{uni}}v_{\mathrm{Kep}}r_{\mathrm{Hill},j}/r_j$ assuming that the difference between the SMBH and the binary j distance and the third object is $p_{\mathrm{uni}}r_{\mathrm{Hill},j}$, where p_{uni} is a random number uniformly distributed between 0 and 1. In Equation (39), we define $p_{\mathrm{c},j}$ using

$$p_{\mathrm{c},k} \equiv \begin{cases} 1 & \text{for } h_k < h_{\mathrm{c}}, \\ \frac{2}{\pi}\arcsin\left[\frac{h_{\mathrm{c}}}{h_k}\right] & \text{otherwise.} \end{cases} \quad (41)$$

For the interaction with the spherical stellar component, we always set $p_{\mathrm{c},j} = 1$. We set the migration velocity of a third body in the disk BH and stellar components by the average of the migration velocity for BHs in a cell hosting BH j, while a third body in the spherical stellar component has no migrating

motion. Here, n_c and σ_c are the number density and velocity dispersion of objects in the cell of the binary, including the spherical stellar component, the disk BH component, and the disk stellar component.[4] The cross section is approximated by

$$\sigma_{\rm coll} = b_{xy,j} b_{z,j}, \tag{42}$$

where $b_{xy,j}$ and $b_{z,j}$ are the effective maximum impact parameters of objects approaching from different directions such that they approach the binary center of mass within a binary separation s_j at closest approach. This is given approximately by

$$b_{xy,j} = \min\left\{ s_j \sqrt{1 + 2\frac{b_{90,j}}{s_j}},\ r_{{\rm Hill},j} \right\}, \tag{43}$$

$$b_{90,j} = \frac{G(m_j + m_c)}{v_{{\rm rel},j}^2}, \tag{44}$$

$$b_{z,j} = \min(b_{xy,j},\ h_{\rm eff}), \tag{45}$$

$$h_{\rm eff} = \max(h_{z,j},\ h_c), \tag{46}$$

where the square-root term accounts for gravitational focusing by the binary's center of mass calculated in the limit where it dominates over the gravity of the SMBH inside the binary's Hill sphere. We conservatively ignore binary–single interactions with objects that have a larger impact parameter than $r_{{\rm Hill},j}$.[5] In Equation (45), we also limit the maximum impact parameter due to the lack of objects moving at the elevation above $h_{\rm eff}$.

When the binary is embedded in the AGN disk, it interacts with both the spherical stellar and the disk stellar and BH components, and otherwise interacts only with the spherical stellar component. We reduce the number of stars in the disk stellar component in the lth cell hosting the binary by one for each BH binary that experiences a hard binary–stellar single interaction with objects in the disk stellar component.

3.3.6. Weak Gravitational Scattering

Weak gravitational scattering is the velocity exchange due to encounters between single objects or between the scattering of the center of mass of a binary with a single object. Based on the Fokker–Planck approximation for an infinite homogeneous medium (Equation (7.92) in Binney & Tremaine 2008), we assume that the mean acceleration due to weak gravitational scattering is

$$\boldsymbol{a}_{{\rm WS},k} = -p_{c,k} \frac{4\pi G^2 (m_k + m_c) m_c n_c \ln\Lambda'}{\sigma_c^2} g(X_k) \hat{\boldsymbol{v}}_k + p_{c,k} \left[\frac{4\sqrt{2}\,\pi G^2 m_c^2 n_c \ln\Lambda'}{\Delta t \sigma_c} \frac{{\rm erf}(X_k)}{X_k} \right]^{1/2} \hat{\boldsymbol{n}} \tag{47}$$

where $p_{c,k}$ sets the fraction of time that the object spends within a scale height for each component, respectively (Equation (41)), the first term corresponds to dynamical friction, and the second term represents Brownian motion,[6] $\hat{\boldsymbol{v}}_k \equiv \boldsymbol{v}_k / v_k$, $\hat{\boldsymbol{n}}$ is a unit vector in a random direction,[7] $X_k \equiv |\boldsymbol{v}_k - \boldsymbol{v}_c| / (\sqrt{2}\sigma_c)$, v_c is the mean velocity of the medium in the comoving Keplerian frame,[8] ${\rm erf}(X)$ is the error function,

$$g(X) = \frac{1}{2X^2}\left[{\rm erf}(X) - \frac{2X}{\sqrt{\pi}} e^{-X^2} \right], \tag{48}$$

and $\ln\Lambda'$ is the Coulomb logarithm. We set $\Lambda' = h_c / b_{90,k}$ following Papaloizou & Larwood (2000), where $b_{90,k}$, given by Equation (44), is the impact parameter at which the direction of particles change by 90° during the encounter. Equation (47) is valid when $\Lambda' > 1$. On the other hand, when $h_c < b_{90,k}$, the scattering is approximately confined within a two-dimensional plane. In this case, we assume that the direction of the acceleration is along the xy plane and set the acceleration according to the Fokker–Planck results for objects confined to an infinite homogeneous two-dimensional medium (B. Kocsis et al. 2020, in preparation),

$$\boldsymbol{a}_{{\rm WS},k} = p_{c,k} \left\{ D[\Delta v_\parallel] \hat{\boldsymbol{v}}_k + \sqrt{\frac{D[\Delta v_\perp^2] + D[\Delta v_\parallel^2]}{\Delta t}} \hat{\boldsymbol{n}}_{xy} \right\}, \tag{49}$$

where $\boldsymbol{n}_{xy}$ is a unit vector in a random direction in the xy (AGN disk) plane, and the dynamical friction and Brownian motion terms are

$$D[\Delta v_\parallel] = -(2\pi)^{3/2} G \Sigma_c x^{1/2} e^{-x} [I_0(x) + I_1(x)] \tag{50}$$

$$D[\Delta v_\perp^2] = D[\Delta v_\parallel^2] = (2\pi)^{3/2} \frac{G\Sigma_c \sigma_c m_c}{m + m_c} x e^{-x} \times \left[\left(1 + \frac{1}{2x}\right) I_0(x) + I_1(x) \right], \tag{51}$$

where $x = v_c^2 / (4\sigma_c^2)$ and $I_0(\cdot)$ and $I_1(\cdot)$ are modified Bessel functions. In practice, we resort to the approximations in Equations (B1)–(B2) of Appendix B.

To simply incorporate the effect of the recoil on a third body due to dynamical friction by the disk BH component, we give the same kinetic energy ($\sum_{k\in l} \boldsymbol{K}_{{\rm WS-DF},k} / N_{{\rm DBH},l}$) to the BHs which are in the AGN disk in the same cell as

$$\boldsymbol{a}_{{\rm WS},k} = \frac{1}{\Delta t} \left(\frac{\sum_{k\in l} \boldsymbol{K}_{{\rm WS-DF},k}}{m_k N_{{\rm DBH},l}} \right)^{1/2}, \tag{52}$$

where $\boldsymbol{K}_{{\rm WS-DF},k}$ is the kinetic energy added onto kth objects due to the dynamical friction by scattering with the disk BH component.

3.3.7. Binary Formation via Three-body Interaction

If three bodies make a close encounter, a binary can form dynamically (e.g., Aarseth & Heggie 1976; Binney & Tremaine 2008). This process can be efficient in very dense or low-velocity dispersion stellar environments.

[4] We calculate the binary–single interaction rate separately for the three components.

[5] Note further that $s_j < r_{{\rm Hill},j}$ holds for stable binaries.

[6] The change in the velocity due to this term after a time step Δt is $\Delta v_k \propto a_{{\rm WS},k} \Delta t \propto \Delta t^{1/2}$ as expected for diffusion. This term is equivalent to $v_k^{-1} \langle \Delta v_k^2 \rangle / \Delta t$, but this representation is numerically more stable for $v_k \ll \sigma_c$.

[7] Note that we assume an isotropic diffusion and averaged Equation (7.92) in Binney & Tremaine (2008) over the direction.

[8] For the BH and stellar disk components $v_c = 0$, while for the stellar spherical component $v_c = v_{\rm Kep}(r_k)$.

For the formation rate of binaries, we extend the rough derivation of Equation (7.111) in Binney & Tremaine (2008) to account for the limitations of a disk geometry and the destructive effect of the SMBH. We assume that binaries can form only when the three bodies undergo a strong encounter. We require an encounter between object i and a second object with impact parameter less than

$$b_i = \min(b_{90,i}, r_{\rm Hill,i}) \tag{53}$$

in a region where there is a third object. Here, $b_{90,i}$ is given by (Equation (44)).[9] For a given BH i, the mean rate of strong single–single scattering encounters is given by $p_{{\rm c},i} n_{\rm c} b_i b_{z,{\rm eff},i} v_{\rm rel,i}$, where $b_{z,{\rm eff},i} = \min(b_i, h_{{\rm eff},i})$ and $h_{{\rm eff},i}$ is given by Equation (46). In each encounter, the probability that a single third BH lies within a distance b_i is of order $n_{\rm c} b_i^2 b_{z,i}$ (Binney & Tremaine 2008), where $b_{z,i} = \min(b_i, h_{\rm c})$. Thus, the mean rate for two single bodies to come within a distance b_i to the ith BH is

$$\Gamma_{\rm 3bbf,i} = \frac{1}{3} p_{{\rm c},i} n_{\rm c}^2 b_i^3 b_{z,{\rm eff},i} b_{z,i} v_{{\rm rel},i} \tag{54}$$

(Binney & Tremaine 2008). The factor of $1/3$ in Equation (54) compensates for triple-counting each three-body pair.

To get a rough understanding of the rate of binary formation per BH via three-body encounters, let us evaluate the order of magnitude of Equation (54), assuming that the mass of objects in the nuclear star cluster is $M_{\rm NSC}$ within an effective radius $r_{\rm NSC}$, with the density profile in Equation (1). We approximate the BH density as

$$n_{\rm BH} = n_0 \left(\frac{r}{r_{\rm NSC}}\right)^{\gamma_\rho - 2}, \quad n_0 = f_0 \frac{\gamma_p}{4\pi} \frac{\eta_{\rm n,BH} M_{\rm NSC}}{r_{\rm NSC}^3} \frac{r}{h}, \tag{55}$$

where $\gamma_\rho = 0$, $f_{\rm DBH}$ is the fraction of BHs in the AGN disk,[10] $v_{\rm rel} \sim \sqrt{3}\, v_{\rm Kep}(r) h/r$, and for simplicity we approximated all height-related quantities with the disk scale height h assuming that $h \equiv h_c \sim h_{z,i} \sim h_{{\rm eff},i}$ in the radial cell of the object i. Furthermore, we use the empirical $M_{\rm SMBH}$–σ, $M_{\rm NSC}$–σ–$r_{\rm NSC}$ relations given below in Equations (78), (77), and (79) and the number of BHs per unit stellar mass is assumed to be $\eta_{\rm n,BH} = 0.002\, M_\odot^{-1}$ in Equation (76). This leads to

$$\begin{aligned}\Gamma_{\rm 3bbf,i} &\sim n_{\rm c}^2 \min(b_{90,i}^3, r_{{\rm Hill},i}^3) \min(b_{90,i}^2, r_{{\rm Hill},i}^2, h^2) v_{{\rm rel},i} \\ &= \min(\Gamma^{(1)}_{\rm 3bbf,i}, \Gamma^{(2)}_{\rm 3bbf,i}, \Gamma^{(3)}_{\rm 3bbf,i}, \Gamma^{(4)}_{\rm 3bbf,i}),\end{aligned} \tag{56}$$

where the four cases are

$$\begin{aligned}\Gamma^{(1)}_{\rm 3bbf,i} &\sim n_{\rm BH}^2 b_{90,i}^5 v_{{\rm rel},i} = n_{\rm BH}^2 \frac{2^5 G^5 m_i^5}{v_{{\rm rel},i}^9} \\ &\sim 7\ {\rm Myr}^{-1} r_{1\,{\rm pc}}^{1/2} \left(\frac{h/r}{0.01}\right)^{-11} m_{i,10}^5 M_{\rm SgrA}^{-3.85} f_{\rm DBH}^2, \\ &\quad \text{if } b_{90,i} \leqslant \min(h, r_{{\rm Hill},i}),\end{aligned} \tag{57}$$

$$\begin{aligned}\Gamma^{(2)}_{\rm 3bbf,i} &\sim n_{\rm BH}^2 r_{{\rm Hill},i}^5 v_{{\rm rel},i} \\ &\sim 0.2\ {\rm Myr}^{-1} r_{1\,{\rm pc}}^{1/2} \left(\frac{h/r}{0.01}\right)^{-1} m_{i,10}^{5/3} M_{\rm SgrA}^{-0.51} f_{\rm DBH}^2, \\ &\quad \text{if } r_{{\rm Hill},i} \leqslant h \leqslant b_{90,i},\end{aligned} \tag{58}$$

$$\begin{aligned}\Gamma^{(3)}_{\rm 3bbf,i} &\sim n_{\rm BH}^2 r_{{\rm Hill},i}^3 h^2 v_{{\rm rel},i} \\ &\sim 0.2\ {\rm Myr}^{-1} r_{1\,{\rm pc}}^{1/2} \left(\frac{h/r}{0.01}\right) m_{i,10} M_{\rm SgrA}^{0.153} f_{\rm DBH}^2, \\ &\quad \text{if } h \leqslant r_{{\rm Hill},i} \leqslant b_{90,i},\end{aligned} \tag{59}$$

$$\begin{aligned}\Gamma^{(4)}_{\rm 3bbf,i} &\sim n_{\rm BH}^2 b_{90,i}^3 h^2 v_{{\rm rel},i} = n_{\rm BH}^2 \frac{2^3 G^3 m_i^3}{v_{{\rm rel},i}^5} h^2 \\ &\sim 2\ {\rm Myr}^{-1} r_{1\,{\rm pc}}^{1/2} \left(\frac{h/r}{0.01}\right)^{-5} m_{i,10}^3 M_{\rm SgrA}^{-5.85} f_{\rm DBH}^2, \\ &\quad \text{if } h \leqslant b_{90,i} \leqslant r_{{\rm Hill},i},\end{aligned} \tag{60}$$

where we used the abbreviated labels defined under Equation (26). Thus, the three-body binary formation rates are greatly increased in the AGN disk because gas reduces the velocity dispersion of the particles. This leads to a strong dependence on h/r in Equation (57). However, because

$$\frac{r_{\rm Hill}}{r} = 0.0094 \frac{m_{i,10}^{1/3}}{M_{\rm SgrA}^{1/3}}, \quad \frac{b_{90}}{r} \simeq 0.02 \frac{m_{i,10}}{M_{\rm SgrA}} \left(\frac{h/r}{0.01}\right)^{-2}, \tag{61}$$

and typically $h/r < h_{\rm AGN}/r \sim 0.01$–$0.001$, Equation (59) represents the most typical case of the binary formation rate via three-body encounters after the BHs are captured by the AGN disk. Equations (57)–(60) show that the binary formation rate is high compared to the AGN lifetime; BHs are expected to form binaries outside of 0.01 pc.

We form a binary due to this dynamical three-body binary formation mechanism in the simulation with probability $P_{{\rm 3bbf},i} = \Gamma_{{\rm 3bbf},i} \Delta t$ using Equation (54). We assume that the initial separation of the newly formed binary is $s_i \equiv b_i$ (Equation (53)). This approximation is justified by the fact that in reality the distribution scales with $s^{9/2}$ for $s \lesssim b_{90}$, and it is exponentially suppressed above b_{90} (see Equation (7.175) in Binney & Tremaine 2008).

When the binary formation criteria are satisfied for some BH i, we search for a binary counterpart i' in the same cell l. The binary mass is given by $m_i + m_{i'}$, and the binary has a velocity of $\boldsymbol{v}_j = \boldsymbol{v}_{\rm kick} + \boldsymbol{v}_{\rm cen}$, where $\boldsymbol{v}_{\rm cen} = (m_i \boldsymbol{v}_i + m_{i'} \boldsymbol{v}_{i'} + m_{\rm c} \boldsymbol{\sigma}_{\rm c} \hat{\boldsymbol{n}})/(m_i + m_{i'} + m_{\rm c})$ is the center-of-mass velocity of the three-body system, and $\boldsymbol{v}_{\rm kick} = [m_{\rm c}/(m_i + m_{i'} + m_{\rm c})](G m_i m_{i'}/d) \hat{\boldsymbol{v}}_{\rm kick}$ is the kick velocity due to the binary formation, where $\hat{\boldsymbol{n}}$ and $\hat{\boldsymbol{v}}_{\rm kick}$ are unit vectors drawn randomly from the isotropic distribution.

We also consider cases in which the third body is a member of the disk stellar component. In this case, we substitute $(n_{\rm c})_{{\rm DBH},l} (n_{\rm c})_{{\rm Dstar},l}$ into $n_{\rm c}^2$ in Equation (54), which further increases the binary formation rate compared to Equations (57)–(60). We assume that all newly formed binaries are BH–BH binaries, and due to the steep scaling of the formation rate with mass we do not consider the formation of BH–stellar binaries or stellar–stellar binaries in this study. The formation of BH–stellar or stellar–stellar binaries may further increase the rate of BH–BH mergers as such binaries are plausibly exchanged with BH–BH binaries after several binary–single interactions with BHs.

[9] A binary can also form if $b_i > b_{90,i}$, but in this case the initial binary separation is typically large, and the binaries are soon disrupted by a soft-binary–single interaction (Aarseth & Heggie 1976). For simplicity, we ignore such soft-binary formation.

[10] Note that all BHs have their own orbital height in the simulation, which changes in time. Here, $f_{\rm DBH}$ labels the objects whose height is at most that of the AGN disk, which is often higher than 10% of the total population.

3.3.8. Gas-capture Binary Formation

Generally, if any form of dissipation removes a sufficient amount of energy during the passage of two bodies inside their mutual Hill sphere, the two objects may not travel back to infinity following the encounter, and a binary forms. In the AGN disk, gas dynamical friction serves as a dissipation mechanism. Goldreich et al. (2002) confirmed that the fraction of two bodies passing within their Hill radius, which becomes bound ($P_{\rm cap,}i$, C in Goldreich et al. 2002), is roughly coincident with the fractional decrease in the binding energy during a passage through the mutual Hill sphere (D in Goldreich et al. 2002). Assuming that the latter is approximated as $t_{\rm pass,}i/t_{\rm GDF,}i$, where

$$t_{{\rm pass},i} = \frac{r_{{\rm Hill},i}}{v_{{\rm rel},i}} \tag{62}$$

is the crossing timescale across the Hill radius, and

$$t_{{\rm GDF},i} = \frac{v_{{\rm rel},i}}{a_{{\rm GDF},i}(v_{{\rm rel},i})} \tag{63}$$

is the timescale of damping of the relative velocity between two bodies by gas dynamical friction (Equation (25)), the probability for binary formation by the gas-capture mechanism during a single BH encounter is

$$P_{{\rm cap},i} = \min(1,\, t_{{\rm pass},i}/t_{{\rm GDF},i}). \tag{64}$$

The binary formation timescale due to the gas-capture mechanism is

$$t_{{\rm cap},i} = \frac{t_{{\rm enc},i}}{P_{{\rm cap},i}}, \tag{65}$$

where

$$t_{{\rm enc},i}^{-1} = p_{{\rm c},i} n_{\rm DBH} r_{{\rm Hill},i} z_{{\rm Hill},i} v_{{\rm rel},i} \tag{66}$$

defines the rate of objects within the disk BH component entering the Hill sphere of BH i, where

$$z_{{\rm Hill},i} = \min(r_{{\rm Hill},i},\, h_{{\rm eff},i}) \tag{67}$$

is the maximum height within the Hill sphere, and $h_{{\rm eff},i}$ is given by Equation (46). Thus, the binary formation rate for the ith BH is $\Gamma_{{\rm gas},i} = \frac{1}{2} t_{{\rm cap},i}^{-1} = \frac{1}{2} t_{{\rm enc},i}^{-1} P_{{\rm cap},i}$, where the $1/2$ factor compensates for double-counting each two-body pair. The probability of binary formation for the ith BH within the simulation time step is $P_{{\rm gas},i} = \Delta t/(2 t_{{\rm cap},i})$. Because the gas-capture mechanism is caused by gas dynamical friction, we assume that it operates only within the AGN disk (Section 3.3.3) and when radiation feedback is inefficient (Section 3.3.3). We set the initial separation to be $s_j = r_{{\rm Hill},i}$. As in the case of the three-body binary formation, after the binary formation criteria are satisfied for some BH i, we search for a binary counterpart i' in the same cell l in the AGN disk. The binary mass is given by $m_i + m_{i'}$ and its velocity by $v_j = v_i$ because the velocity of a counterpart i' is dissipated during the passing time.

Let us estimate the rough timescale for gas-capture binary formation as in Section 3.3.7. The capture fraction $P_{{\rm cap},i} = \min(1,\, t_{{\rm pass},i}/t_{{\rm GDF},i})$ is ~ 1 in the ranges we calculate (10^{-4} pc $< r <$ 5 pc) as

$$\frac{t_{{\rm pass},i}}{t_{{\rm GDF},i}} \sim 9.9 \times 10^5 r_{1\,{\rm pc}}^4 \left(\frac{h/r}{0.01}\right)^{-4} m_{i,10} M_{\rm SgrA}^{-4/3} \rho_{\rm gas,6}, \tag{68}$$

where $\rho_{\rm gas,6} \equiv \rho_{\rm gas}/(10^6\, M_\odot\ {\rm pc}^{-3}) \propto r_{1\,{\rm pc}}^{-3}$ in the fiducial model according to Figure 4, and we assume $f \sim 1$ in $a_{\rm GDF}$. The rate of gas-capture binary formation per BH is roughly estimated as

$$\begin{aligned}\Gamma_{{\rm cap},i} &\sim t_{{\rm cap},i}^{-1} \\ &\sim t_{{\rm enc},i}^{-1} \sim 7\ {\rm Myr}^{-1} r_{1\,{\rm pc}}^{-1/2} \frac{h/r}{0.01} m_{i,10} M_{\rm SgrA}^{0.494} f_0, \end{aligned} \tag{69}$$

where we use $h < r_{\rm Hill}$. By comparing Equation (59) with Equation (69), $\Gamma_{{\rm 3bbf},i} \propto r_{1\,{\rm pc}}^{1/2}$, $\Gamma_{{\rm cap},i} \propto r_{1\,{\rm pc}}^{-1/2}$, and $\Gamma_{{\rm cap},i} \sim 30\, \Gamma_{{\rm 3bbf},i}$ at $r = 1$ pc, we conclude that the rate of gas-capture binary formation dominates the rate of three-body binary formation.

If the center of mass of a binary makes a close encounter with a third object, it may undergo a gas-capture interaction to form a hierarchical triple. In such a case, the Kozai–Lidov effect may facilitate the merger of the inner binary (e.g., Silsbee & Tremaine 2017; Liu & Lai 2018). Additionally, perturbations caused by density inhomogeneities may lead to a close binary–single encounter, which may contribute to the hardening of the binary. We conservatively ignore these merger pathways in the simulation. This subject merits future investigation.

3.3.9. Time Step

We use a shared time step

$$\begin{aligned}\Delta t = \eta_t \min_k \Bigg(& \frac{s_k}{ds/dt|_{{\rm GW},k}},\, \frac{s_k}{ds/dt|_{{\rm typeII},k}}, \\ & \frac{s_k}{ds/dt|_{{\rm GDF},k}},\, t_{{\rm BS},k},\, t_{{\rm GBS},k}, \\ & \frac{r_k}{dr_k/dt|_{{\rm typeI/II}}} \Bigg), \end{aligned} \tag{70}$$

where $\eta_t = 0.1$ is a constant in the fiducial model, but is varied below.

3.3.10. Merger Prescription

Because N-body particles represent stellar-mass BHs, a merger occurs when the separation of a binary becomes smaller than the sum of the innermost stable circular orbits ($6Gm_j/c^2$) of the binary components. During a BH merger, the merged remnant recoils due to anisotropic GW emission. The GW recoil kick velocity depends on the mass ratio, spin magnitude, and spin direction of the merged BHs (e.g., Baker et al. 2007; Campanelli et al. 2007; Herrmann et al. 2007; Koppitz et al. 2007). In the fiducial model, we assume that the BH spins are zero and set the recoil velocity to

$$v_{\rm GW} = 8830\ {\rm km\ s^{-1}} \frac{q^2(1-q)}{(1+q)^5}, \tag{71}$$

whose functional form and normalization are derived by post-Newtonian predictions and fits to numerical relativity simulations, respectively, where q is the mass ratio of merged BHs (Baker et al. 2007). This formula gives a maximum kick

Table 2
Fiducial Values for the Model Parameters

Parameter	Fiducial Value
Mass of the central SMBH	$M_{\rm SMBH} = 4 \times 10^6\,M_\odot$
Gas accretion rate from the outer radius	$\dot{M}_{\rm out} = 0.1\,\dot{M}_{\rm Edd}$
Fraction of preexisting binaries	$f_{\rm pre} = 0.15$
Power-law exponent for the initial density profile for BHs	$\gamma_\rho = 0$
Parameter setting the initial velocity anisotropy for BHs	$\beta_{\rm v} = 0.2$
Efficiency of angular momentum transport in the α-disk	$\alpha_{\rm SS} = 0.1$
Stellar mass within 3 pc	$M_{\rm star,3\,pc} = 10^7\,M_\odot$
Initial mass function slope	$\delta_{\rm IMF} = 2.35$
Angular momentum transfer parameter in the outer disk	$m_{\rm AM} = 0.15$
Accretion rate in Eddington units onto stellar-mass BHs	$\Gamma_{\rm Edd,cir} = 1$
Numerical time-step parameter	$\eta_t = 0.1$
Number of radial cells storing physical quantities	$N_{\rm cell} = 120$
Maximum and minimum r for the initial BH distribution	$r_{\rm out,BH} = 3$ pc, $r_{\rm in,BH} = 10^{-4}$ pc

velocity of $v_{\rm GW} \simeq 160\,{\rm km\,s^{-1}}$ at $q \sim 0.4$. However, because the kick velocity is very sensitive to BH spins, we also investigate cases with a constant kick velocity of $v_{\rm GW} = 400$, 600, and 1000 km s^{-1} in models 26, 27, and 28, respectively. We add the recoil velocity to the velocity of the merged remnant v_i, and the direction is assumed to be random and isotropically distributed. We set the mass loss due to GW radiation at mergers assuming zero spins for BHs as

$$m_{\rm GW} = m_j(1 - 0.2\eta) \tag{72}$$

(Tichy & Marronetti 2008), where $\eta = q/(q+1)^2$ is the symmetric mass ratio.

4. Results

We start this section by describing an illustrative example of a binary that formed and merged in our fiducial model (Section 4.1). We then present the demography and various physical properties of the entire binary population in the fiducial model (Sections 4.2 and 4.3), and discuss how the most important quantities change when model parameters are varied (Section 4.4).

4.1. Formation and Evolution of Binaries

We first present the evolution of a binary in the fiducial model (labeled as model 1 in Table 3, whose parameter values are listed in Table 2) in Figure 5. The binary in this figure forms at 0.74 Myr with an initial separation of 8.9×10^{-3} pc at $r_j = 1.8$ pc by the gas-capture mechanism. The masses of the binary components are 9.9 $M_\odot$ and 9.1 $M_\odot$. In the early phase, the binary separation decreases significantly due to gas dynamical friction of the AGN disk (blue line in panel (b)). The binary also migrates toward the SMBH due to type I/II torque of the AGN disk (orange line in panel (a)). Affected by gas dynamical friction, accretion torque, and weak gravitational scattering, v_j settles to a stochastic equilibrium between heating and damping (i.e., dashed blue, dashed cyan, purple, pink, and gray lines in panel (d)) and v_j fluctuates stochastically around the equilibrium. The binary experiences several hard binary–single interactions with a disk BH and star (brown and orange lines in panels (b) and (d)). During the interaction, the binary receives recoil kicks due to the binary–single interaction in a random direction (black and blue lines in panel (c) and brown and orange lines in panel (d)). In some interactions, this binary is chosen as a third object for the binary–single interaction with other binaries. For simplicity, we assume that this third object receives a recoil kick, even though it is a binary (Section 3.3.5). Following a recoil kick, the binary's radial migration is delayed (orange line in panel (c)) as the binary moves out of the AGN disk. Then, v_j is damped by gas dynamical friction and the accretion torque of the AGN disk (dashed blue and cyan lines in panel (d)). After the binary migrates to $r_j \lesssim 6 \times 10^{-2}$ pc, and the separation reaches $s_j \sim 10^{-6}$ pc ~ 0.2 au, binary–single interactions become frequent with disk BHs (brown line in panel (b)). After the binary is hardened to $s_j \sim 1.8 \times 10^{-8}$ pc, GW radiation drives it to merge (purple line in panel (b) of Figure 5) at 4.8 Myr. This binary merges outside of the AGN disk as the merger takes place soon after a binary–single interaction. During the evolution, 0.8 $M_\odot$ and 0.9 $M_\odot$ gas mass is accreted onto the primary and secondary BHs, respectively. In summary, this binary, formed via the gas-capture mechanism, is initially mostly hardened by gas dynamical friction, and later by a series of binary–single interactions with other BHs in the AGN disk, and finally by GW radiation.

4.2. Demography of the BH Binary Population

Figure 6 shows the evolution of the number of BHs (dotted black), mergers (dotted red), all binaries (dotted purple), BHs (cyan) and binaries (green) in the AGN disk, BHs that migrated within the inner radius $r_{\rm in} = 10^{-4}$ pc (brown), and in situ formed BHs (gray) in the fiducial model. Initially, the number of binaries is 1.5×10^3, and the number of BHs and binaries in the AGN disk are 3.3×10^2 and 35, respectively. The number of BHs and binaries in the AGN disk increase for $\sim$3 Myr (cyan and green lines), and then these quantities decrease due to the reduction of the number of BHs due to mergers. The reduction due to binary disruption (orange dashed curve labeled "ionization") is relatively less important. The number of mergers and in situ formed BHs keep increasing for 100 Myr (dashed red and gray lines). Up to 100 Myr, 1.2×10^4 mergers occur and 1.0×10^3 BHs are formed in situ. This implies that some fraction of BHs merged several times within 100 Myr.

Figure 7 shows the evolution of mergers among binaries formed by the different mechanisms in the simulation. Mergers among gas-capture binaries, preexisting binaries, and dynamically formed binaries start to take place from $\gtrsim$0.05, $\gtrsim$0.2, and $\gtrsim$0.3 Myr (solid cyan, purple, and orange lines), respectively. In the fiducial model, mergers among the binaries formed by the gas-capture mechanism dominate over the other formation channels (cyan line). This highlights the importance of gas-capture binary formation when discussing compact-object

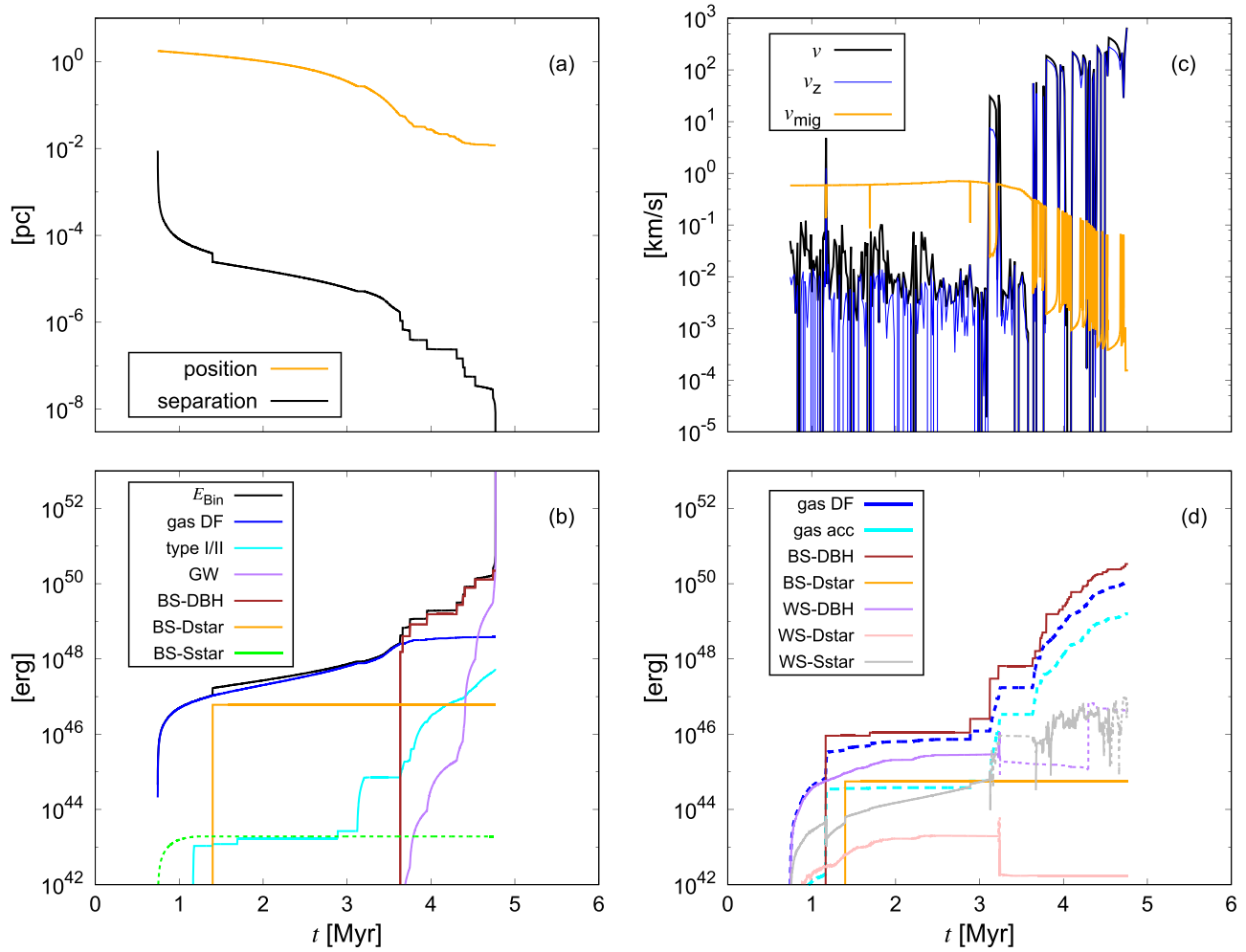

Figure 5. Time evolution of the physical quantities describing a typical binary that formed in the fiducial model by the gas-capture mechanism. (a) The evolution of the binary separation (black) and the radial distance from the SMBH (orange). (b) The black line shows the evolution of the binding energy of the binary. The other lines show the cumulative contributions of gas dynamical friction (blue), type I/II torque (cyan), gravitational wave radiation (purple), and binary–single interactions with the disk BH (brown) and stellar (orange) and spherical stellar (green) components. Negative values are indicated by dashed curves in panels (b) and (d). (c) The evolution of the velocity of the center of the binary relative to the local motion of the AGN disk v_j (black), the z-direction velocity $v_{z,j}$ (blue), and the migration velocity (orange). (d) The cumulative change in the binary's center-of-mass kinetic energy due to dynamical friction by gas (dashed blue), gas accretion torque (dashed cyan), binary–single interactions with the disk BH (brown) and disk stellar (orange) components, and weak gravitational scattering with disk BHs (purple), disk stars (pink), and the spherical stellar (gray) components.

mergers in AGN disks. Mergers among in situ formed BHs contribute only 4.1% of the total number of mergers at 100 Myr (dashed black line). Of the mergers at 100 Myr, 0.85, 0.11, and 0.04 are gas-capture binaries, preexisting binaries, and dynamically formed binaries (solid cyan, purple, and orange lines), respectively, and 0.64, 0.27, and 0.09 of mergers among in situ formed BHs at 100 Myr are gas-capture binaries, preexisting binaries, and dynamically formed binaries (dashed cyan, purple, and orange lines), respectively.

Figure 8 shows the distribution of binaries in binary separation (s_j) and distance from the SMBH (r_j). At $t = 0$ yr (panel (a)), 1462 preexisting binaries are distributed according to the initial condition. The upper bound on s arises from the assumption that soft binaries are disrupted prior to the AGN phase, and the lower bound on s comes from the assumption that the initial binary separation must be larger than the sum of the radii of the progenitor stars to survive without merging during the main-sequence stellar phase.

Because gas-capture binaries form within the AGN disk, they spend a large fraction of their time within the AGN disk. Both the radial position (r_j) and the binary separation (s_j) evolve simultaneously for such binaries (Figure 5).

Figure 9 shows the dominant binary-hardening mechanisms at two different times. Gas-capture binaries (cyan circles in Figure 8) are hardened mostly by gas dynamical friction (blue circles in Figure 9) before binaries migrate to $r \sim 10^{-2}$ pc and their separation reduces to $s \sim 10^{-6}$ pc ~ 0.2 au. At smaller r, gas-capture binaries are hardened mostly by binary–single interaction with the disk BH component (brown triangles in Figure 9) and reach merger (cyan line in panel (b) of Figure 10).

Most prexisting binaries (purple squares in Figure 8) are hardened mostly by type I/II torque of a circumbinary disk (cyan squares in Figure 9). Preexisting binaries also merge after migrating to $\sim 10^{-2}$ pc (purple line in panel (b) of Figure 10).

Panels (a) and (b) of Figure 10 show the number of BHs, stars, and mergers as a function of the distance from the

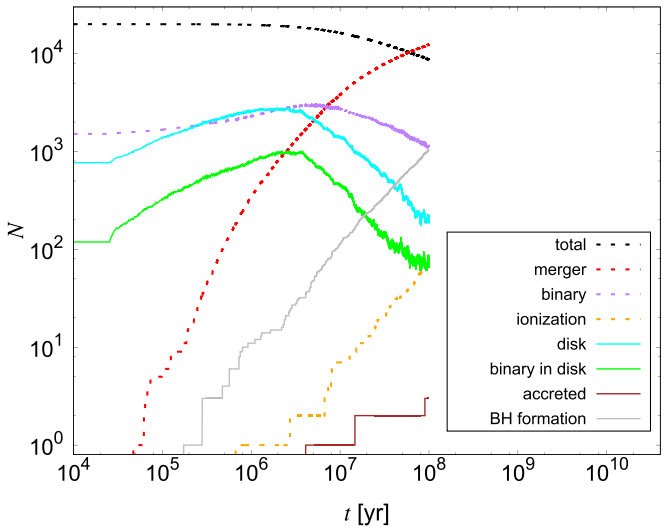

Figure 6. Time evolution of the number of various types of objects in the fiducial model: the total number of BHs (dotted black), BH binaries (dotted purple), cumulative number of BH mergers (dotted red), the AGN disk's objects shown with solid lines including the BHs (cyan), BH binaries (green), and in situ formed BHs (gray), and BHs that migrated within the inner radius $r_{\rm in} = 10^{-4}$ pc (brown). The number of BHs is significantly reduced by frequent repeated mergers. The reduction of binaries due to disruption (orange dashed curve labeled "ionization") is relatively less important.

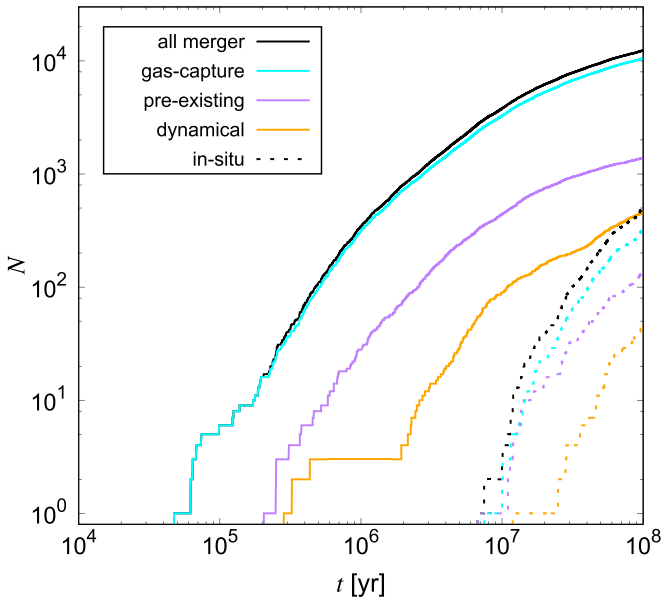

Figure 7. Time evolution of the cumulative number of mergers among binaries formed by different mechanisms in the fiducial model. The total number of mergers (black), mergers among gas-capture binaries (cyan), preexisting binaries (purple), and dynamically formed binaries (orange) are shown by solid lines. Dashed lines represent the contribution from in situ formed BHs. Mergers from gas-capture binaries dominate over other binary formation channels.

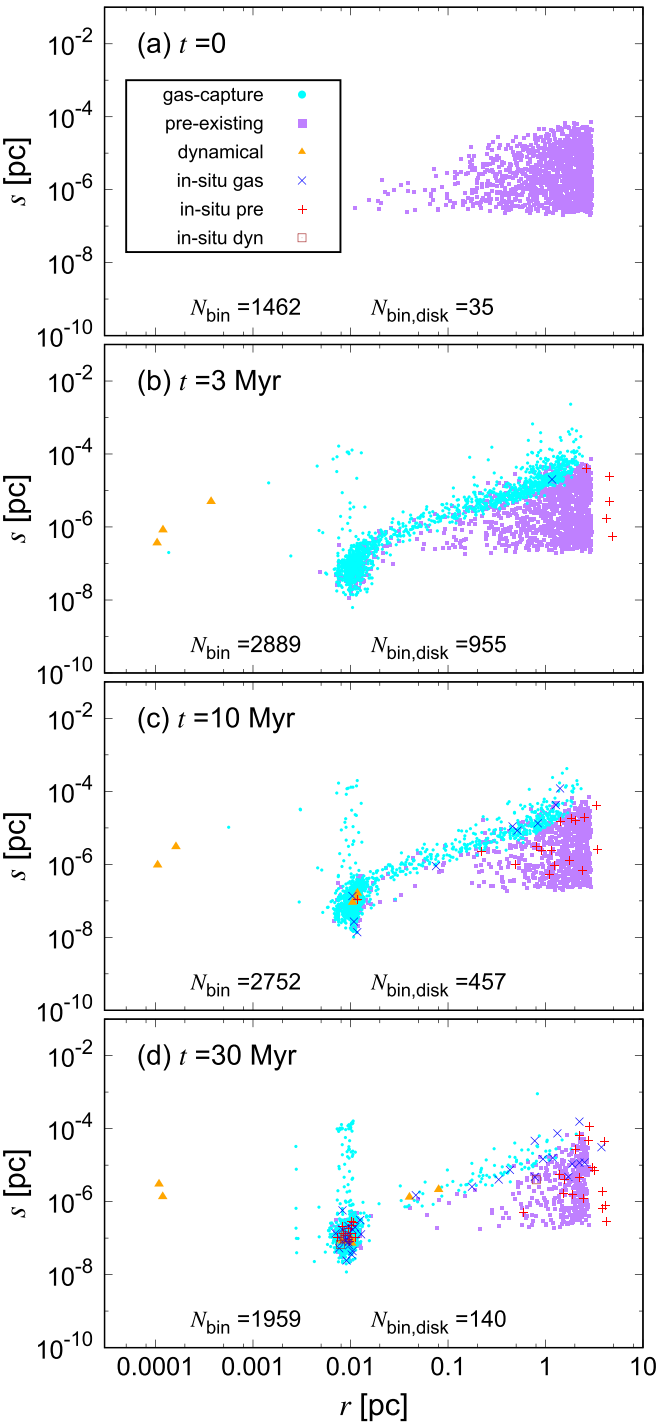

Figure 8. Distribution of binaries in binary separation and distance from the SMBH at four different times. Cyan circles, purple squares, and orange triangles represent gas-capture binaries, preexisting binaries, and dynamically formed binaries, respectively. Blue crosses, red pluses, and brown squares represent gas-capture binaries, preexisting binaries, and dynamically formed binaries for in situ formed BHs, respectively. Panels (a)–(d) show the distribution at $t = 0$, 3, 10, and 30 Myr, respectively. Binaries formed by different mechanisms have distinct spatial and separation distributions.

SMBH, respectively. Black, brown, and blue lines in panel (a) are all BHs, and stars and BHs in the AGN disk at 30 Myr, respectively. At $r \sim 0.01$–0.1 pc, most of the BHs are captured in the AGN disk due to the strong gaseous drag from the high-density AGN disk.

Most mergers occur in $r \lesssim 0.01$ pc (panel (b) of Figure 10). In this region, the surface density of the AGN disk $\Sigma_{\rm disk,min}$ is reduced by torques from stellar-mass BHs (Equation (19)) due to the low scale height for the AGN disk (blue line in Figure 4), and the migration timescale increases by a factor of a few (blue line in panel (c) of Figure 10).

Panel (c) of Figure 10 shows the relevant timescales affecting the evolution of a BH binary with $m_k = 10\,M_\odot$ in the simulation. Black and gray lines show the timescale for the initial supersonic velocity of BHs relative to the local AGN

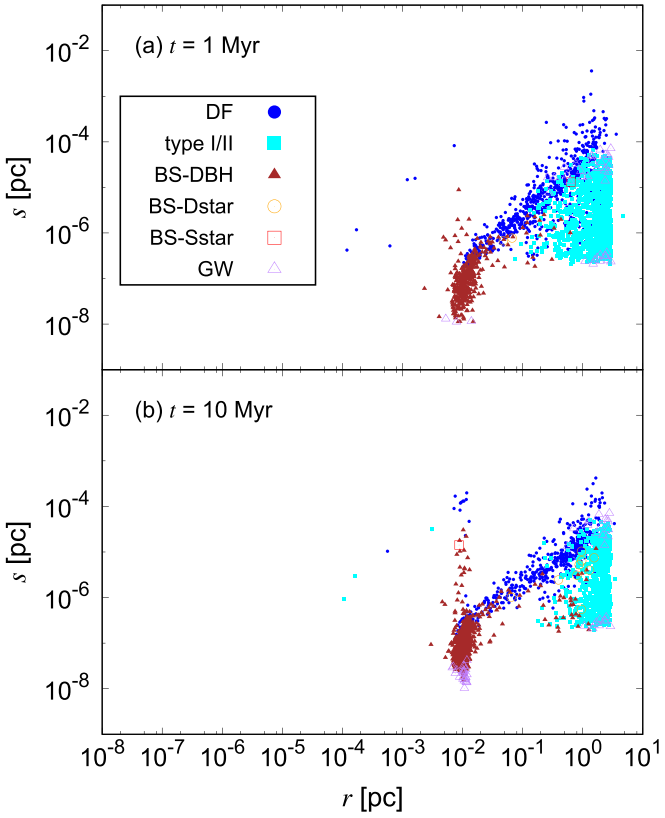

Figure 9. Dominant hardening mechanism is indicated for each binary in the fiducial model at 1 Myr (top panel) and 10 Myr (bottom panel) in the plane of the in-cluster location r vs. the binary separation s. Different colored points represent binaries hardened mostly by GW (purple triangles), gas dynamical friction (blue circles), type I/II torque of a circumbinary disk (cyan squares), and binary–single interaction with the disk BH (brown triangles) and stellar (orange circles) components and the spherical stellar component (red squares). Panels (a) and (b) show the distributions at $t = 1$ and 10 Myr, respectively. The dominant hardening mechanism changes with the binary's location.

motion $v_{\mathrm{ini},k}$ to decay due to gas dynamical friction and for the BH binary to be captured in the AGN disk, t_{capAGN}, for $v_{\mathrm{ini},k} = 0.2\, v_{\mathrm{Kep}}$ and $v_{\mathrm{ini},k} = 0.3\, v_{\mathrm{Kep}}$ (Equation (26)).

The blue line in panel (c) of Figure 10 shows the migration timescale given by Equation (18). The orange line in panel (c) of Figure 10 is the timescale on which the binary is hardened by gas dynamical friction, $t_{\mathrm{GDF,HS}}$, given by Equation (27). The cyan line marks 100 Myr, which roughly corresponds to the upper limit for the typical lifetime of AGN disks (e.g., Martini 2004). We do not show the hardening timescale of binaries due to type I/II torque of a circumbinary disk surrounding the binary because it depends on the binary separation (Bartos et al. 2017). For example, the hardening timescale by type I/II torque of a circumbinary disk around a binary with $m_{j_1} = m_{j_2} = 5\, M_\odot$ and the Eddington accretion rate is ∼100 Myr at $s_j = 1$ au and ∼200 Myr at $s_j = 0.1$ au. In Figure 9, we have shown that binary hardening by type I/II migration dominates over gas dynamical friction for small binary separations at a fixed location in the AGN disk beyond 0.05 pc, but it is subdominant at nearly all separations for $r \lesssim 0.05$ pc. Note that recently revised type I/II migration timescales (e.g., Duffell et al. 2014; Kanagawa et al. 2018) are longer than the previously used type II migration timescale in which a clear gap is assumed. At around 1 pc, t_{mig} and $t_{\mathrm{GDF,HS}}$ intersect (orange and blue line in panel (c)). Most outer binaries in the AGN disk migrate within this radius before they are

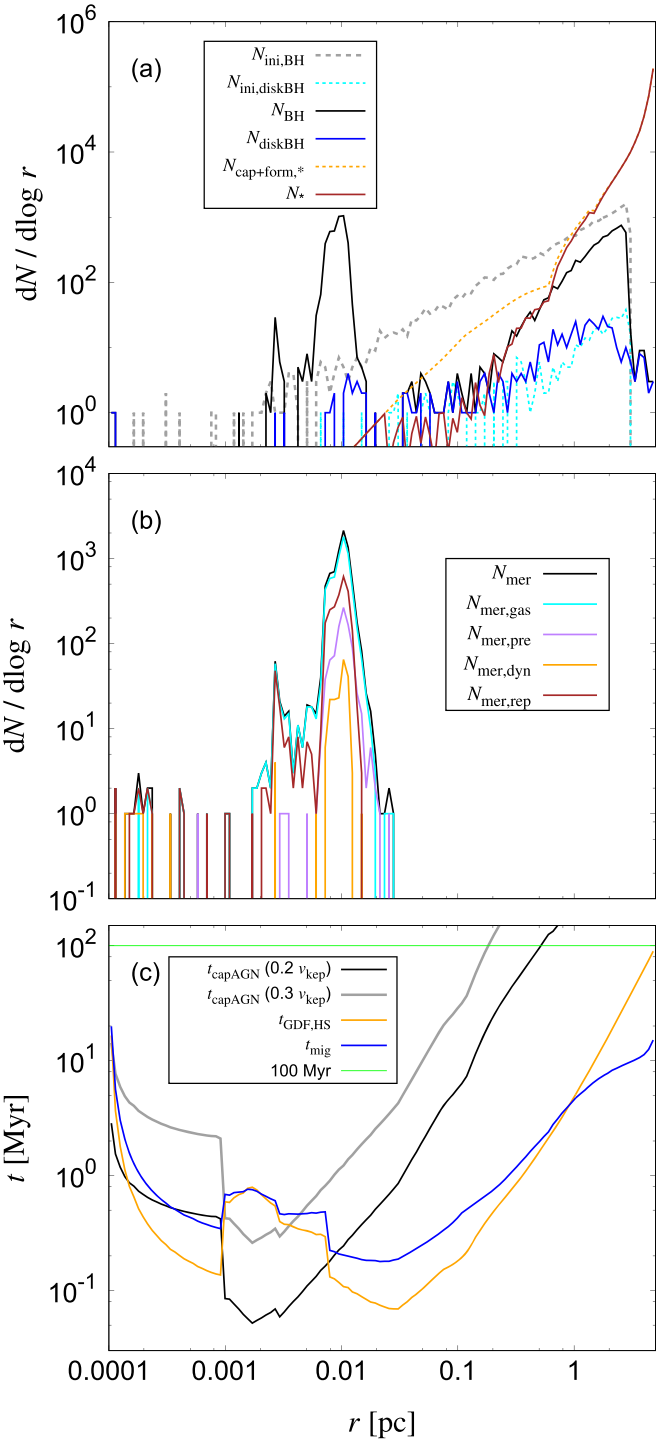

Figure 10. Radial distribution of several quantities measured in different simulation cells. (a) The number of BHs at $t = 0$ (dashed gray) and 30 Myr (solid black), the number of BHs in the AGN disk at $t = 0$ (dashed cyan) and 30 Myr (solid blue), and the number of stars in the AGN disk (solid brown) and stars which are formed and captured in the AGN disk (dashed orange) at 30 Myr. (b) The total number of mergers for all binaries (black), mergers of gas-capture-formed binaries (cyan), preexisting binaries (purple), and dynamically formed binaries (orange) at 30 Myr. (c) The relevant timescales for an $m_k = 10\, M_\odot$ binary as a function of radial distance from the SMBH. Lines represent the decay timescale of the BH velocity while crossing the disk due to gas dynamical friction (t_{capAGN}; Equation (26)) for $v_{\mathrm{ini},k} = 0.2\, v_{\mathrm{Kep}}$ (black) and $v_{\mathrm{ini},k} = 0.3\, v_{\mathrm{Kep}}$ (gray), the timescale for binary hardening by gas dynamical friction to the hard–soft boundary ($t_{\mathrm{GDF,HS}}$; Equation (27), orange), the migration timescale (Equation (18), blue), and the typical maximum lifetime of AGN disks (100 Myr, cyan). Binaries migrate to $\lesssim$ parsec before they become hard binaries.

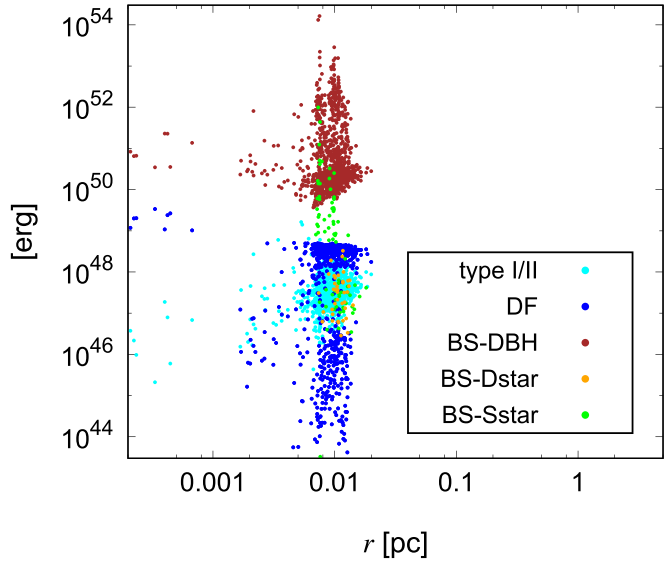

Figure 11. Total binding energy lost to different mechanisms as a function of the distance from the central SMBH at merger for all successfully merged binaries over 30 Myr in the fiducial model (model 1). Points represent hardening by the type I/II torque of a circumbinary disk (cyan), gas dynamical friction (blue), and binary–single interactions with the disk BH (brown) and stellar (orange) and spherical stellar (green) components. Binary–single interactions dominate the total energy lost during the binary hardening.

hardened by gas dynamical friction. Also outside of ∼1 pc, BHs are not captured by the AGN disk if the initial relative velocity of BHs $v_{\mathrm{ini},k}$ is higher than 0.2–0.3 v_{Kep}.

4.3. Binary-hardening Mechanisms

To clarify the relative importance of different binary-hardening mechanisms for the merging binary population in the fiducial model, Figure 11 shows the binding energy lost to several mechanisms as a function of the distance from the central SMBH (r_j) at merger for all successfully merging binaries (see Figure 9 showing the instantaneous dominant mechanism for all binaries). Most merged binaries are hardened mostly by binary–single interactions with the disk BH component (brown dots in Figure 11). Some fraction of mergers are hardened by $\gtrsim 10^{51}$ erg due to binary–single interaction. The masses of these merged binaries are very high, $\sim 10^2$–$10^3\,M_\odot$, due to repeated mergers (Figure 12 below and panel (b) of Figure 10). For comparison, note that the separation as a function of binding energy E of a binary with total mass $10m_{j,10}M_\odot$ and symmetric mass ratio $\eta_j = q_j(1+q_j)^{-2}$ is $s_j = 10^{-6}\,\mathrm{pc}\, m_{j,10}^2(4\eta_j)(E/10^{48}\,\mathrm{erg})^{-1}$, where $10^{-6}\,\mathrm{pc} = 0.2\,\mathrm{au}$.

Gas dynamical friction also contributes $\sim 10^{48}$–10^{49} erg to binary hardening. As seen in the Figure 9, gas dynamical friction hardens binaries during the early phases of their evolution.

For mergers at $r_j \sim 0.01$ pc from the SMBH, binary–single interactions with the disk stellar component contribute 10^{46}–10^{48} erg to binary hardening (orange dots in Figure 11). Because stars in the AGN disk are distributed at $r \gtrsim 0.01$ pc (panel (a) of Figure 10), interactions with the disk stellar component occur before binaries migrate to $\lesssim$0.01 pc.

4.4. Dependence on Model Parameters

Table 3 shows the results for several different variations with respect to the fiducial model. The input represents the settings for parameters and mechanisms in each model. In the output columns, we show the properties of the system at 30 Myr, namely, the number of merged binaries (N_{mer}), surviving binaries (N_{bin}), the fraction of mergers among preexisting binaries ($f_{\mathrm{mer,pre}}$), gas-capture-formed binaries ($f_{\mathrm{mer,gas}}$), and dynamically formed binaries ($f_{\mathrm{mer,dyn}}$) compared to the total number of mergers, the fraction of repeated mergers to total mergers ($f_{\mathrm{mer,rep}}$), the number of BHs that migrate within the inner boundary r_{in} (N_{acc}), and the number of mergers among BHs formed in situ due to the fragmentation of the AGN disk ($N_{\mathrm{mer,SF}}$).

4.4.1. Number and Fraction of Mergers

The fraction of the merger number (N_{mer}) from the initial BH number ($N_{\mathrm{totBH,ini}}$; $f_{\mathrm{BH,mer}} \equiv N_{\mathrm{mer}}/N_{\mathrm{totBH,ini}}$) at $t = 30$ Myr is $\sim 0.02 - 0.8$ for models 1–37, where $N_{\mathrm{totBH,ini}} = 2\times10^4$ in models 1–16 and 22–37, and $N_{\mathrm{totBH,ini}} = 1.0\times10^5$, 6.2×10^4, 2.0×10^3, 6.6×10^3, and 6.0×10^3 for models 17, 18, 19, 20, and 21, respectively. We find that the merger fraction is almost unaffected by hardening due to gaseous processes (models 1, 3–6), the recoil kick velocity at mergers (models 26–28), or the preexisting binary fraction (models 29–31). On the other hand, the merger fraction is lowest when migration does not operate (model 2) and highest when we only consider the evolution for BHs in the inner regions ($r_{\mathrm{out,BH}} = 0.3$ pc, model 19). This is because mergers require BHs to migrate to the inner regions of $\lesssim$0.01 pc where the hardening by binary–single interaction is efficient. In the cases of lower β_{v}, which determines the dispersion of the initial BH velocity distribution, the number of mergers is higher (models 1, 13–16) because a larger fraction of BHs is captured in the AGN disk where binary formation and hardening are efficient. Also the merger fraction is low in the high SMBH mass case (model 12) because the high Keplerian velocity enhances the decay timescale of the BH velocity v_k (see Equation (26)). Note that high-mass SMBHs tends to have larger AGN disks and nuclear star clusters, which also needs to be considered for the estimate of the merger rate (see Section 5.5 below). If we take into account interactions with BHs outside the AGN disk (model 37), the merger fraction is enhanced by a factor of 1.4. This is because the high-density BHs in the inner regions ($\lesssim 10^{-2}$ pc) outside the AGN disk (black line in panel (a) of Figure 10) enhance the rate of hard binary–single interactions.

The number of mergers from in situ formed BHs ($N_{\mathrm{mer,SF}}$) depends strongly on the accretion rate of the AGN disk $\dot{M}_{\mathrm{out}}$ (models 1, 9, 10) and the angular momentum transfer parameter m_{AM} (models 23–25). This is because the star formation rate depends on $\dot{M}_{\mathrm{out}}$ and m_{AM}. The rate of mergers among in situ formed BHs is estimated in Section 5.6.

4.4.2. Convergence Test

We checked whether the results change due to the time-step parameter (models 1, 35, 36) or the size of cells (models 1, 33, 34) in which physical quantities for the components (Equations (6), (8), and (9)), and the AGN disk (Figure 4) are stored. The number of mergers (N_{mer}) is not significantly affected by these parameters at around the fiducial values (see N_{mer} for models 1 and 34 or models 1 and 36). Hence, the

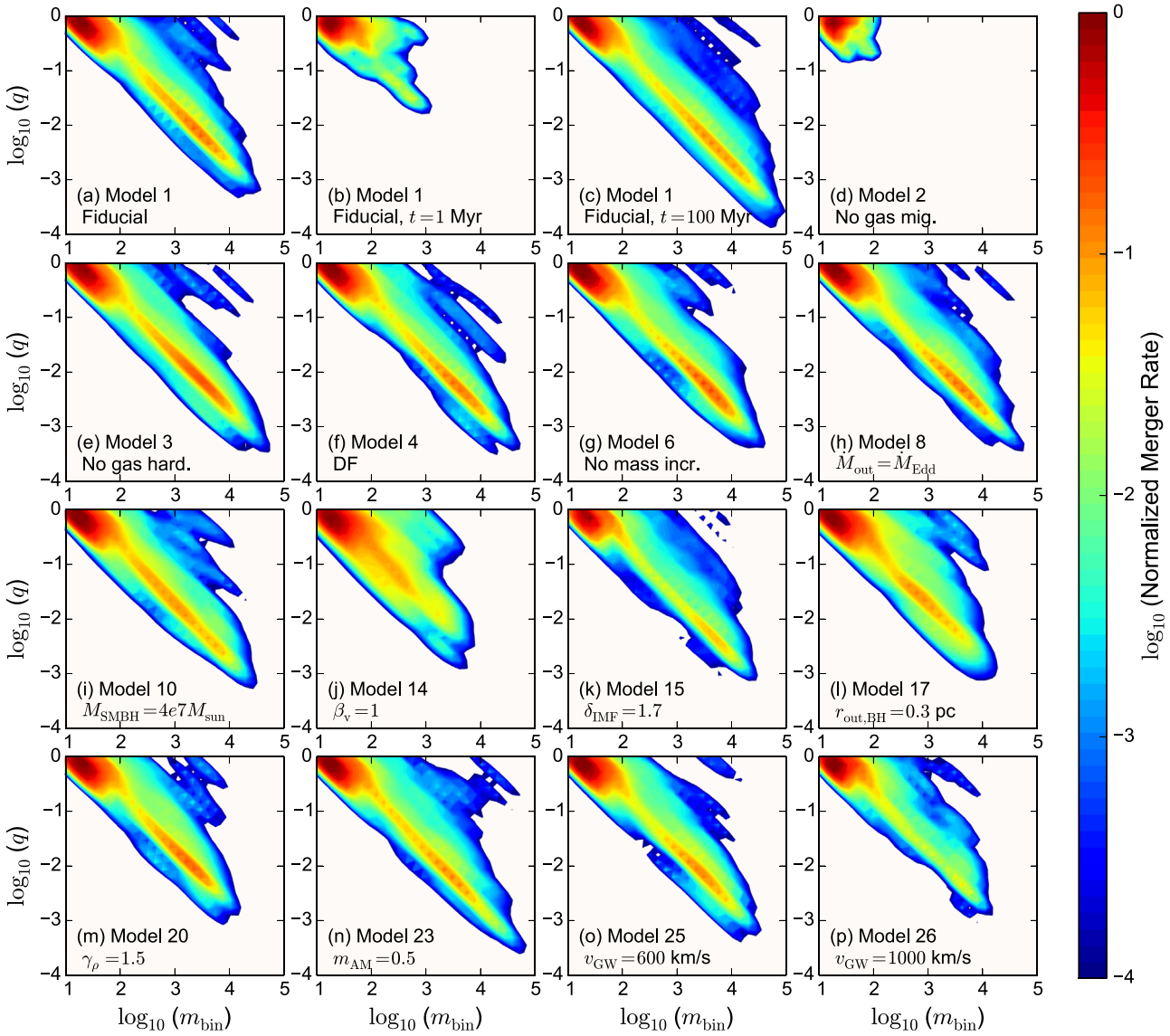

Figure 12. Distribution of mergers in the binary mass vs. binary mass ratio plane is shown for different models and times as labeled. Panels (a) and (d)–(l) show the merger rate distribution at 10 Myr, and panels (b) and (c) show the distribution at 1 and 100 Myr, respectively. The merger rate is normalized by the maximum value in the plane. IMBHs form due to repeated mergers in most models.

merger fraction, which we are interested in, is not influenced by the numerical resolution.

4.4.3. Repeated Mergers

In the fiducial model, the fraction of repeated mergers is as high as $\sim$0.26 at 30 Myr, allowing massive BHs to form. Figure 12 shows the distribution of merged BHs in the binary mass versus binary mass ratio plane, and Figure 13 shows the cumulative distribution of the merged mass of binaries. Figures 12 and 13 show that BHs can grow to $\sim 10^2$–$10^4\,M_\odot$ by repeated mergers in most models. In the fiducial model at 30 (10) Myr, the maximum BH mass is $1.4\times10^4\,M_\odot$ ($8.6\times10^3\,M_\odot$), and 14 (9) and 1 (2) BHs are more massive than $10^2\,M_\odot$ and $10^3\,M_\odot$, respectively. In model 17 ($\delta_{\rm IMF}=-1.7$) at 30 (10) Myr (panel (k) of Figure 12) in which the initial number of BHs is higher ($N_{\rm totBH,ini}=10^5$), the maximum BH mass is $2.2\times10^4\,M_\odot$ ($1.2\times10^4\,M_\odot$), and 128 (81) and 6 (4) BHs are more massive than 10^2 and $10^3\,M_\odot$, respectively. Thus, we find that a lot of IMBHs of $\gtrsim 10^2\,M_\odot$ are reproduced by repeated mergers.

4.4.4. BH Binary Parameter Distributions

Figure 14 shows the normalized detection rate in the binary mass versus mass ratio plane for several models in Table 3. The normalized detection rate is calculated as the product of the merger rate and the detection volume (e.g., Equation (6) of The LIGO Scientific Collaboration & The Virgo Collaboration 2012). We use the noise spectral density from the calibrated sensitivity spectra of aLIGO Hanford on 2018 November 8 (Kissel & Betzwieser 2018). Note that our simulations can only roughly estimate the total binary mass and mass ratio distribution of mergers as we do not take into account the exchange interactions during binary–single and binary–binary interactions.

In Figure 14, panel (a), we have overlaid the mass distribution of the observed LIGO/VIRGO sources during the O1 and O2 observing runs (gray points). Interestingly,

Table 3
Summary of Results in Different Models

Input			Output							
M	Gas	Parameter	$N_{\rm mer}$	$N_{\rm bin}$	$f_{\rm mer,pre}$	$f_{\rm mer,gas}$	$f_{\rm mer,dyn}$	$f_{\rm mer,rep}$	$N_{\rm acc}$	$N_{\rm mer,SF}$
1	max	Fiducial	7.7×10^{3}	2.0×10^{3}	0.12	0.85	0.026	0.31	2	93
2	No gas mig.	Fiducial	4.0×10^{2}	6.6×10^{3}	0.092	0.91	2.5×10^{-3}	0.21	0	0
3	No gas hard.	Fiducial	6.5×10^{3}	2.9×10^{3}	0.13	0.83	0.032	0.35	2	49
4	DF	Fiducial	7.8×10^{3}	2.0×10^{3}	0.12	0.86	0.028	0.33	1	97
5	type I/II	Fiducial	6.9×10^{3}	2.6×10^{3}	0.13	0.84	0.029	0.35	2	48
6	Negative type I/II	Fiducial	6.8×10^{3}	2.8×10^{3}	0.14	0.82	0.035	0.36	9	56
7	No mass incr.	Fiducial	7.4×10^{3}	2.1×10^{3}	0.12	0.85	0.031	0.31	2	78
8	No acc tor.	Fiducial	7.8×10^{3}	1.9×10^{3}	0.12	0.86	0.023	0.33	1	1.0×10^{2}
9	max	$\dot{M}_{\rm out}=0.4\,\dot{M}_{\rm Edd}$	8.3×10^{3}	2.4×10^{3}	0.12	0.85	0.038	0.33	2	3.9×10^{2}
10	max	$\dot{M}_{\rm out}=\dot{M}_{\rm Edd}$	8.6×10^{3}	3.8×10^{3}	0.12	0.82	0.058	0.32	1	6.7×10^{2}
11	max	$M_{\rm SMBH}=4\times10^{5}\,M_{\odot}$	6.3×10^{3}	4.0×10^{3}	0.12	0.85	0.026	0.35	0	0
12	max	$M_{\rm SMBH}=4\times10^{7}\,M_{\odot}$	5.2×10^{3}	3.2×10^{3}	0.078	0.91	0.011	0.33	3	47
13	max	$\beta_{\rm v}=0.1$	1.0×10^{4}	2.5×10^{3}	0.11	0.86	0.037	0.31	2	88
14	max	$\beta_{\rm v}=0.3$	5.4×10^{3}	1.7×10^{3}	0.13	0.85	0.019	0.32	1	91
15	max	$\beta_{\rm v}=0.5$	3.2×10^{3}	1.4×10^{3}	0.13	0.84	0.023	0.36	2	98
16	max	$\beta_{\rm v}=1$	1.6×10^{3}	1.5×10^{3}	0.14	0.83	0.033	0.45	3	1.2×10^{2}
17	max	$\delta_{\rm IMF}=-1.7$	3.8×10^{4}	1.2×10^{4}	0.079	0.86	0.063	0.32	3	5.7×10^{2}
18	max	$\delta_{\rm IMF}=-2$	2.2×10^{4}	7.7×10^{3}	0.11	0.86	0.036	0.30	3	3.2×10^{2}
19	max	$r_{\rm out,BH}=0.3$ pc	1.5×10^{3}	1.9×10^{2}	0.084	0.89	0.024	0.40	2	1.3×10^{2}
20	max	$r_{\rm out,BH}=1$ pc	3.5×10^{3}	5.6×10^{2}	0.10	0.87	0.032	0.34	2	86
21	max	$M_{\rm star,3pc}=3\times10^{6}\,M_{\odot}$	2.6×10^{3}	8.3×10^{2}	0.12	0.84	0.037	0.32	5	36
22	max	$\gamma_{\rho}=-0.5$	6.8×10^{3}	2.0×10^{3}	0.12	0.85	0.025	0.31	4	87
23	max	$m_{\rm AM}=0.1$	6.5×10^{3}	2.8×10^{3}	0.11	0.86	0.026	0.33	1	57
24	max	$m_{\rm AM}=0.3$	8.9×10^{3}	1.2×10^{3}	0.11	0.86	0.027	0.33	4	39
25	max	$m_{\rm AM}=0.5$	8.9×10^{3}	1.1×10^{3}	0.12	0.86	0.027	0.33	3	2
26	max	$v_{\rm GW}=400$ km s^{-1}	7.9×10^{3}	1.9×10^{3}	0.11	0.86	0.024	0.32	2	90
27	max	$v_{\rm GW}=600$ km s^{-1}	8.0×10^{3}	1.8×10^{3}	0.12	0.86	0.024	0.31	2	99
28	max	$v_{\rm GW}=1000$ km s^{-1}	8.5×10^{3}	1.6×10^{3}	0.12	0.86	0.019	0.33	2	86
29	max	$f_{\rm pre}=0$	7.4×10^{3}	1.6×10^{3}	0	0.97	0.028	0.31	2	98
30	max	$f_{\rm pre}=0.3$	7.9×10^{3}	2.2×10^{3}	0.21	0.76	0.027	0.31	2	93
31	max	$f_{\rm pre}=0.7$	8.1×10^{3}	3.1×10^{3}	0.39	0.58	0.027	0.32	2	76
32	max	$\alpha_{\rm SS}=0.01$	7.9×10^{3}	2.0×10^{3}	0.11	0.86	0.025	0.33	2	1.2×10^{2}
33	max	$N_{\rm cell}=80$	7.2×10^{3}	2.4×10^{3}	0.11	0.85	0.036	0.33	1	89
34	max	$N_{\rm cell}=160$	7.8×10^{4}	1.9×10^{3}	0.12	0.85	0.028	0.31	1	99
35	max	$\eta_{t}=0.4$	8.4×10^{3}	1.6×10^{3}	0.12	0.83	0.056	0.33	1	1.2×10^{2}
36	max	$\eta_{t}=0.2$	7.9×10^{3}	1.8×10^{3}	0.12	0.84	0.040	0.31	3	1.1×10^{2}
37	Fiducial	anisotropic BH component	1.1×10^{4}	6.9×10^{2}	0.11	0.85	0.042	0.40	2	1.2×10^{2}

Table 3
(Continued)

Input			Output							
M	Gas	Parameter	$N_{\rm mer}$	$N_{\rm bin}$	$f_{\rm mer,pre}$	$f_{\rm mer,gas}$	$f_{\rm mer,dyn}$	$f_{\rm mer,rep}$	$N_{\rm acc}$	$N_{\rm mer,SF}$
1	max	$t = 1$ Myr	3.4×10^2	2.3×10^3	0.081	0.91	8.7×10^{-3}	0.29	0	0
1	max	$t = 100$ Myr	1.2×10^4	1.2×10^3	0.11	0.85	0.037	0.34	3	5.1×10^2

Note. The first column indicates the model number. "DF," "type I/II," "max," "No gas hard.," and "Negative type I/II" in the "Gas" column represent models in which binaries are hardened by gas dynamical friction, type I/II torque, maximum of gas dynamical friction and type I/II torque, not hardened by gas interaction, and type I/II torque whose direction is opposite (negative), respectively. "No gas mig.," "No mass incr.," and "No acc tor." in the "Gas" column mean models without the type I/II torque of the AGN disk, without the mass increase by gas accretion, and without velocity damping by gas accretion torque, respectively. In the "parameter" column, we indicate parameters that deviate from the fiducial model, while "anisotropic BH component" refers to a model (#37) in which this component is also taken into account. In the output columns, we summarize the main results in each model: $N_{\rm mer}$ is the merged number; $N_{\rm bin}$ is the binary number; $f_{\rm mer,pre}$, $f_{\rm mer,gas}$ and $f_{\rm mer,dyn}$ are, respectively, the fraction of mergers from preexisting binaries, gas-capture binaries, and dynamically formed binaries compared to total mergers; $f_{\rm mer,rep}$ is the fraction of repeated mergers over total mergers; $N_{\rm acc}$ is the number of BHs that migrate within $r_{\rm in}$; and $N_{\rm mer,SF}$ is the merged number from in situ formed BHs at $t = 30$ Myr for the upper 37 rows and $t = 1$ and $t = 100$ Myr for rows 38 and 39, respectively.

despite the fact that the expected maximum BH mass at birth is limited to $\lesssim 15\,M_\odot$ due to the solar-metallicity environment in galactic nuclei, our results in Figure 14 suggest that the total mass of the detectable merging binaries in AGN extends to masses of $250\,M_\odot$. This is beyond the mass of the detected sources announced to date (but also see Udall et al. 2019). In the fiducial model, the fraction of mergers with $m_{\rm bin} > 200\,M_\odot$ is 8.1%, that with $q < 0.1$ is 2.8%, and that with $m_{\rm bin} > 200\,M_\odot$ and $q < 0.1$ is 2.2%. If such mergers will be discovered in the future, it can be a possible signature that mergers are originating in AGN disks.

The hardening of the mass function of mergers in AGN migration traps, if they exist, was previously pointed out by Yang et al. (2019b). Our results confirm the assumption of the existence of a region similar to a migration at ∼0.01 pc. The hardening of the mass function seen in Figure 12 is more prominent than previously thought, due to the relatively high likelihood of multiple generations of mergers.

4.4.5. Impact of the GW Recoil Velocity

In the case where the recoil velocity at mergers due to anisotropic GW radiation is 600 km s^{-1} (model 27), 19 (19) BHs grow to $\gtrsim 10^2\,M_\odot$ by repeated mergers at 30 (10) Myr in a single AGN, which is similar to our fiducial model assuming much lower GW kicks. To realize the high kick velocity of $v_{\rm GW} \gtrsim 600$ km s^{-1}, the BHs need to be rapidly spinning and the directions of BH spins must be misaligned with the angular momentum direction of a binary. Hence, even if the recoil kick velocity is very high, repeated mergers build up binaries with total masses of $\gtrsim 100\,M_\odot$, which contribute moderately to the detection rate.

Our simulation results confirm previous assumptions on the possibility of mass growth of BHs through mergers in AGN disks (McKernan et al. 2012, 2014; Yang et al. 2019a). Mergers of massive BHs in the pair-instability supernova mass gap such as in Zackay et al. (2020) can provide a compelling case that mergers are facilitated by AGN disks, although masses in some cases can be significantly overestimated due to statistical noise fluctuations (Fishbach et al. 2020).

4.4.6. BH Growth by Gas Accretion

Figure 15 shows the ratio of the accreted mass to the BH mass for the fiducial model. Gas accretion contributes to the BH masses by less than several tens of percent. Thus, gas accretion is not a dominant mechanism for BH growth. The contribution of gas accretion decreases as the BH mass increases. This suggests that BHs violently grow through repeated mergers. Figure 16 shows the merger number as a function of the generation of primary and secondary BHs for the fiducial model. The generation of a BH is defined as the number of mergers that the BH has experienced in the past plus one. Some BHs have experienced hundreds of mergers in their past, during which the masses of BHs are also increased by a factor of about hundreds due to repeated mergers. Hence, BHs grow mainly due to repeated mergers. Figure 17 shows the merger number as a function of the generation of primary BHs for several generations of secondary BHs. Most mergers are between first-generation BHs (orange histogram), while the growth of massive BHs (large $N_{\rm g,p}$) is dominated by mergers with second-generation BHs (cyan histogram).

5. Discussion

5.1. Spin of Merging Binaries

The binary in Figure 5 merges outside of the AGN disk ($h_{z,k} > h_{{\rm AGN},l}$). In the fiducial model, 81%, 80%, 97%, and 19% of mergers—all mergers among gas-capture binaries, preexisting binaries, and dynamically formed binaries, respectively—occur outside of the AGN disk (evaluated at 30 Myr). At $t = 1$, 10, and 100 Myr, the fractions of mergers outside of the AGN disk are 0.84, 0.81, and 0.78, respectively, and less massive BHs tend to merge outside of the AGN disk (orange regions in Figure 13). The direction of the internal orbital angular momentum of binaries orbiting outside of the AGN disk may be misaligned in a random direction following hard binary–single interactions for kicked binaries. Similarly, vector resonant relaxation and flyby encounters may reorient the preexisting orbital-plane binaries. In these cases, the correlation between the direction of BH spins and the angular momentum of binaries vanishes, which can produce mergers with low values of the effective spin parameter. GW observations may statistically distinguish a population of higher-generation mergers based on the measurement of the effective spin (Fishbach et al. 2017; Gerosa & Berti 2017). Note that 91% of mergers among dynamically formed binaries that merged in the AGN disk are mergers of $\gtrsim 10^3\,M_\odot$ BHs, which are not observed by LIGO.

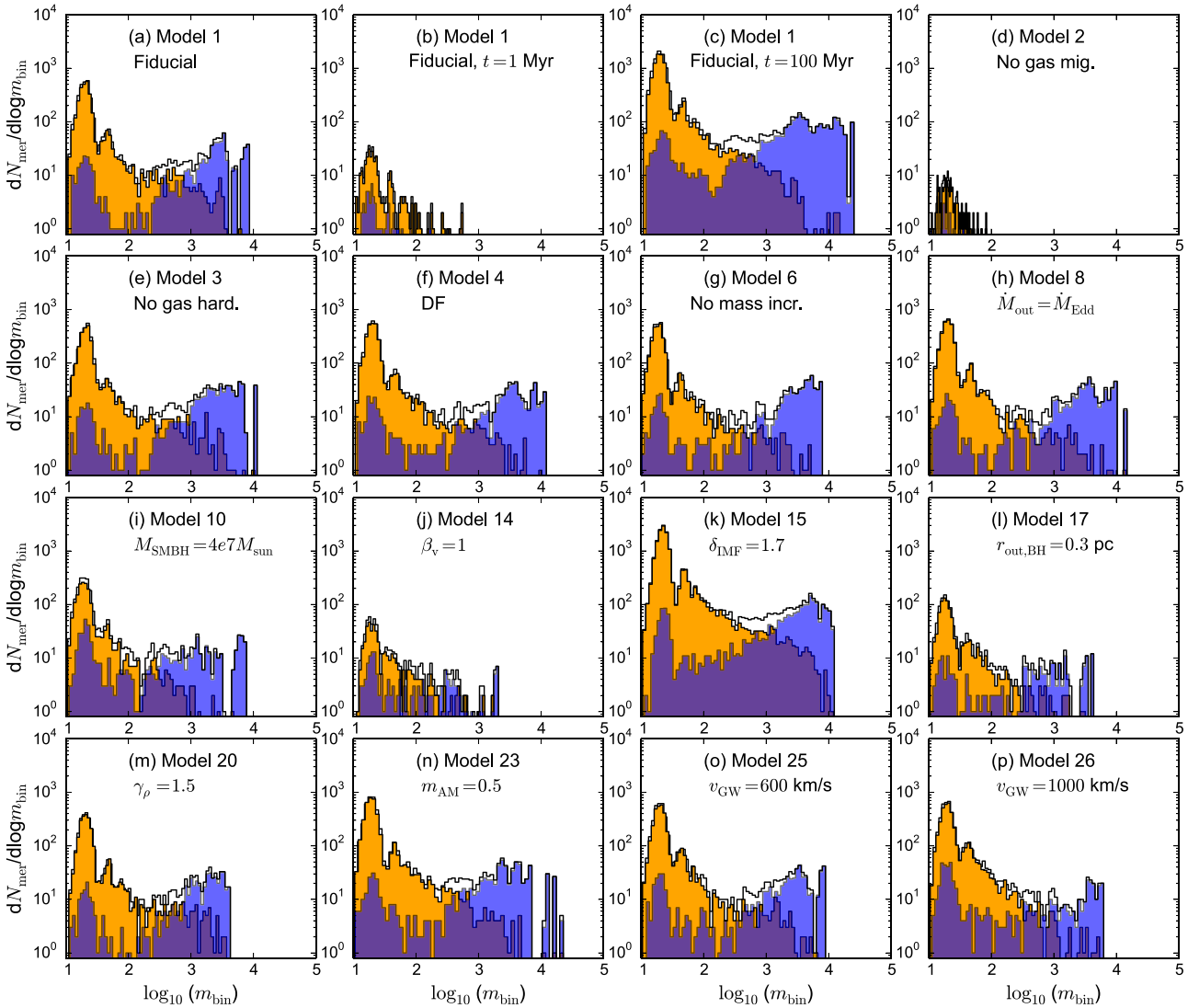

Figure 13. Distribution of binary masses at mergers. The layout of models in the different panels is the same as in Figure 12. The orange and blue regions present the distribution for mergers outside and inside the AGN disk, respectively.

Furthermore, 19% of mergers occur within the AGN disk in the fiducial model. In these mergers, the binary's orbital angular momentum is expected to be aligned or antialigned with the angular momentum direction of the AGN disk (McKernan et al. 2018, 2020; Secunda et al. 2019; Yang et al. 2019a). Previous studies also suggest that a few to 10% mass increase by gas accretion might be sufficient to align the spin directions of BHs in a binary with the angular momentum direction of a circumbinary disk (e.g., Scheuer & Feiler 1996; Natarajan & Pringle 1998; Ogilvie 1999; Hughes & Blandford 2003; King et al. 2005; Bogdanovic et al. 2007; Volonteri et al. 2007; Lodato & Gerosa 2013), and the angular momentum direction of a circumbinary disk is suggested to be the same as for the AGN disk (e.g., Lubow et al. 1999). GW sources with a moderate to high effective spin such as GW 151216, GW 170403, and GW 170817A (Zackay et al. 2019, 2020; The LIGO Scientific Collaboration & the Virgo Collaboration 2020; Venumadhav et al. 2020) may represent mergers with multiple-generation mergers in AGN disks (see also McKernan et al. 2018; Gayathri et al. 2020; Tagawa et al. 2020).

5.2. Doppler Acceleration and Gravitational Lensing

Figure 11 and panel (b) of Figure 10 shows that most mergers occur between 0.001 and 0.02 pc from the SMBH. Due to the high acceleration in the gravitational field of the SMBH in these regions, the effect of Doppler acceleration may be detectable in a multiyear detection campaign. The resulting frequency drift (or change in apparent redshift) allows the binary's distance from the SMBH to be estimated from the LISA GW waveforms (Inayoshi et al. 2017b; Meiron et al. 2017; Wong et al. 2019). Inayoshi et al. (2017b) found that when the projected separation $r \sin I$ of a 10–10 $M_\odot$ BH binary from a 4×10^6 SMBH is smaller than $\sim$0.2 pc (where I is the inclination of the orbital plane of the center of mass for a binary), the strain perturbation by Doppler acceleration is detectable. Wong et al. (2019) estimated that when $r \sin I$ is smaller than $\sim$0.01–0.03 pc for such binaries, the orbital period and velocity around the SMBH are determined with $\lesssim$10% uncertainties. In the fiducial model of a single AGN until 30 Myr, the expected number of mergers within 0.001, 0.003, 0.01, and 0.03 pc from the SMBH is 0.25%, 1.4%, 45%, and 100%, respectively. Even in the case where migration does not

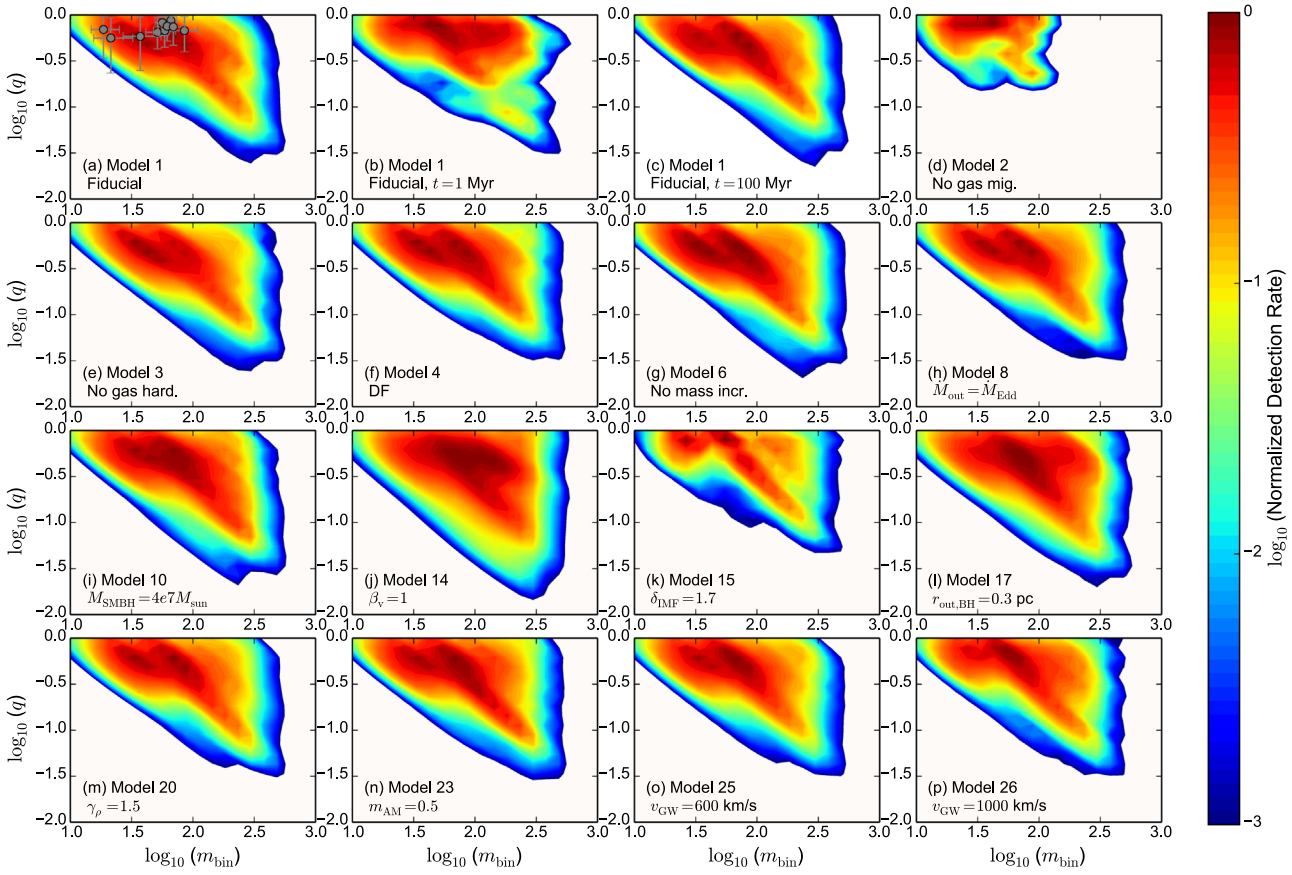

Figure 14. Similar to Figure 12, but showing the normalized detection rate of mergers in the binary mass vs. binary mass ratio plane in several models. We use the noise spectral density of the ER13 (prior to the O3) run of LIGO Hanford (Kissel & Betzwieser 2018). The merger rate is normalized by the maximum value in the plane. In panel (a), the GW events detected to date are overplotted (Abbott et al. 2019a). The mass and mass ratio distribution can well match the observed distribution in some parameter regions. Because our simulations do not take into account the exchange of binary components during interactions, this figure presents rough estimates of the mass ratio.

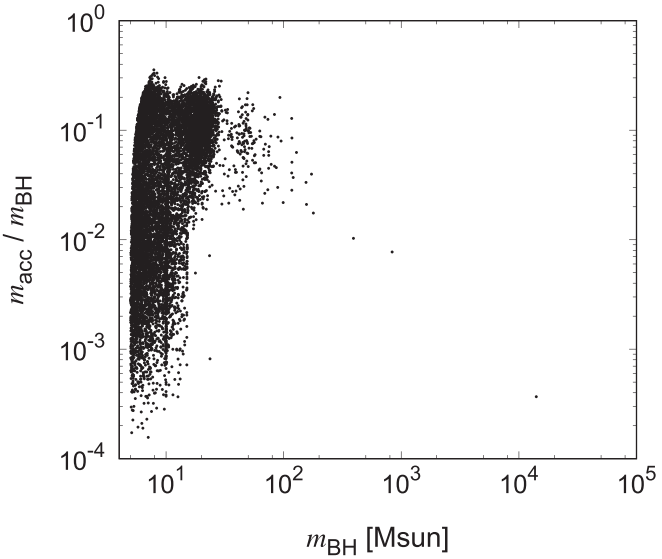

Figure 15. Ratio of the accreted mass to the BH mass as a function of the BH mass at 30 Myr in the fiducial model. BHs typically gain several tens of percent of their final mass via gas accretion.

operate (model 2), the fraction of all mergers within 0.003, 0.01, 0.03, 0.1, and 0.3 pc from the SMBH at 30 Myr is 0.50%, 5.0%, 25%, 78%, and 99%, respectively.

Furthermore, for configurations in which the binary's orbit around the SMBH is not too far from edge on, the GW emission from the binary can be lensed by the SMBH (Kocsis 2013). D'Orazio & Loeb (2020) found that GW wave signals for a tight orbit, repeatedly lensed by an SMBH, are observable with the probability of more than a few percent by LISA if the orbital period around an SMBH is less than $\sim$1 yr. In our fiducial model, a fraction of 0.25% of all mergers satisfies this condition. Thus, perturbations in the GW waveforms due to Doppler acceleration and gravitational lensing are expected to be observable by future GW instruments, provided that the rates in this channel are sufficiently high for detections.

5.3. Eccentricity of Merging Binaries

When mergers are facilitated by binary–single interactions, mergers may have some residual binary eccentricities (e.g., Heggie 1975; Hills 1975; Trani et al. 2019), which are expected to be observed by future low-frequency GW instruments (Brown & Zimmerman 2010; Nishizawa et al. 2016; Gondan et al. 2018a; Hinder et al. 2018; Huerta et al. 2018; Klein et al. 2018; Lower et al. 2018; Abbott et al. 2019b; Gondan & Kocsis 2019; Romero-Shaw et al. 2019). Also, when mergers are initially driven by type I/II torque, a significant binary eccentricity is expected to remain at mergers (e.g., Artymowicz et al. 1991;

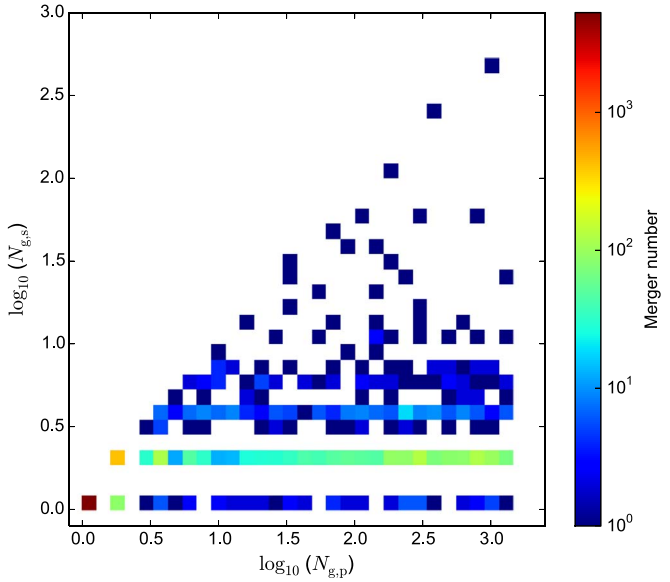

Figure 16. Number of mergers as a function of the generation of the primary ($N_{\rm g,p}$) vs. the secondary ($N_{\rm g,s}$) BH in the fiducial model up to 30 Myr. The generation of a BH is defined as the number of mergers that its progenitor BHs have experienced in the past (plus one). Here, "primary" and "secondary" refer to the BHs for which $N_{\rm g,p} \geqslant N_{\rm g,s}$. Most mergers are between first-generation BHs, but some BHs experience over a thousand mergers.

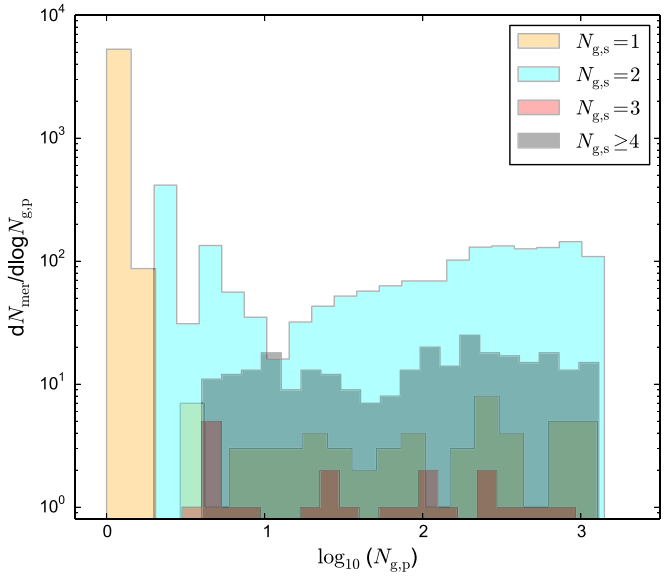

Figure 17. Distribution of the generation of the primary ($N_{\rm g,p}$) for several values of the secondary ($N_{\rm g,s}$) in the fiducial model up to 30 Myr. Orange, blue, red, and gray histograms represent the distribution for $N_{\rm g,s} = 1$, 2, 3, and $N_{\rm g,s} \geqslant 4$, respectively.

Armitage & Natarajan 2005; Cuadra et al. 2009; Rödig et al. 2011; Fleming & Quinn 2017; Muñoz et al. 2019).

The binary eccentricity can be enhanced to typically around 0.7 during binary–single interactions if the eccentricity distribution approaches a thermal shape (e.g., Geller et al. 2019).[11] Once the binaries are driven by GWs, the eccentricity

[11] For an isotropic thermal distribution, e^2 is uniformly distributed. The median eccentricity is $1/\sqrt{2} \sim 0.7$, and 19% of sources have $e > 0.9$.

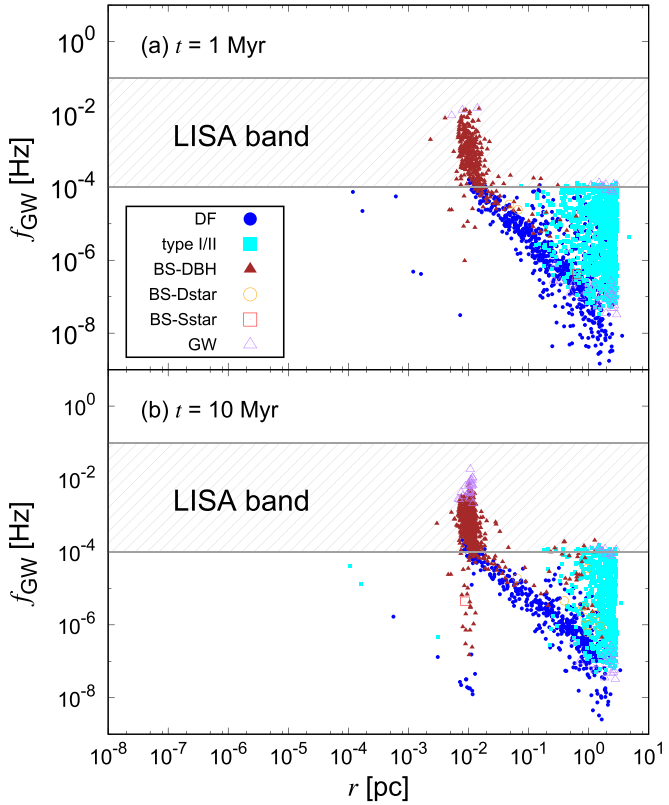

Figure 18. Same as Figure 9, but the vertical axis represents the peak GW frequency $f_{\rm GW}$. To calculate $f_{\rm GW}$, we assume the eccentricity of the binary to be 0.7, which is the median value of the thermal distribution. The hatched gray regions enclose 10^{-1} and 10^{-4} Hz, in which LISA is sensitive to GWs (Amaro-Seoane et al. 2017).

decreases (Peters 1964). To highlight an example, consider a $5 + 5\,M_\odot$ BH binary, whose initial binary separation is 3×10^{10} cm, and the initial binary eccentricity is 0.7. This setting corresponds to the typical binding energy ($\sim 2 \times 10^{50}$ erg) down to which first-generation binaries in an AGN disk can be hardened by binary–single interactions. The orbital frequency of such a binary is 1.1×10^{-3} Hz, and the peak GW frequency is $f_{\rm GW} = 1.2 \times 10^{-2}$ Hz (Wen 2003). Because LISA will be able to detect the eccentricity of $\gtrsim 10^{-3}$ at $f_{\rm GW} \sim 0.01$ Hz (Nishizawa et al. 2016), a nonzero eccentricity is expected to be measurable if BH mergers originate from AGN disks. Following Peters (1964), the binary eccentricity subsequently evolves by GW radiation to $\sim 3 \times 10^{-4}$ at $f_{\rm GW} = 10$ Hz. The eccentricity is slightly higher than typical values for in-cluster mergers in globular clusters and somewhat smaller than for GW capture binaries in galactic nuclei (e.g., Gondán et al. 2018b; Rodriguez et al. 2018; Zevin et al. 2019). Thus, the value of the eccentricity along with masses and spins may provide distinctive footprints to identify BH binaries in AGNs.

5.4. GW Phase Shift and Population Distribution

Figure 18 shows the dominant hardening mechanism as a function of distance from the SMBH and the peak GW frequency $f_{\rm GW}$ (Wen 2003) at two snapshots, 1 Myr (top panel) and 10 Myr (bottom panel), for the fiducial model assuming an eccentricity of 0.7. Most binaries are hardened predominantly by

binary–single interactions in the LISA band at $\sim 10^{-2}$–10^{-4} Hz peak frequencies before GWs drive the binaries to merger.[12]

5.5. GW Event Rates

5.5.1. Stellar-mass BH–BH Mergers in AGNs

Here we estimate the merger rate among stellar-mass BHs in AGN disks. We calculate the merger rate density $\mathcal{R}_{\rm sBH}$ for stellar-mass BH mergers as

$$\mathcal{R}_{\rm sBH} = \int_{M_{\rm SMBH,min}}^{M_{\rm SMBH,max}} \frac{dn_{\rm AGN}}{dM_{\rm SMBH}} \frac{f_{\rm BH,mer} N_{\rm BH,cross}}{t_{\rm AGN}} dM_{\rm SMBH}, \quad (73)$$

where $N_{\rm BH,cross}$ is the number of BHs crossing AGN disks, $t_{\rm AGN}$ is the average lifetime of AGN disks, $n_{\rm AGN}$ is the average number density of AGNs in the universe, $f_{\rm BH,mer}$ is the merger fraction per BH in an AGN given by Table 3, and $M_{\rm SMBH,min}$ and $M_{\rm SMBH,max}$ are the minimum and maximum SMBH masses we consider here.

To derive $N_{\rm BH,cross}$, we assume that the power-law exponent of the probability distribution function of the BH orbital radii around the SMBH (Equations (1) and (55)) is $\gamma_\rho = 0$ on large scales (100 pc). Within parsec scales, this value is motivated by theoretical studies of a relaxed mass-segregated cluster (e.g., Hopman & Alexander 2006; Antonini 2014). Outside of the radius of a nuclear cluster, the slope of the one-dimensional stellar density is observed to be $\gamma_\rho \sim 0$ up to $\sim$100 pc (Feldmeier et al. 2014; Schödel et al. 2014), although some fluctuation exists at each r. In the case of $\gamma_\rho = 0$, the number of BHs that exist within r is given by $N_{\rm BH,NSC} \times r/r_{\rm eff,NSC}$, where $N_{\rm BH,NSC}$ is the number of BHs in a nuclear star cluster, and $r_{\rm eff,NSC}$ is the effective (half-mass) radius of a nuclear star cluster. Also in this distribution ($\gamma_\rho = 0$), the number of BHs crossing the AGN disk for a thermal eccentricity distribution is enhanced by a factor of $\sim$10 compared to the number of BHs on strictly circular orbits (see Equation (7) in Bartos et al. 2017). Conservatively ignoring this enhancement due to eccentricity, we assume that the number of BHs crossing the AGN disk is

$$N_{\rm BH,cross} = N_{\rm BH,NSC} \frac{r_{\rm AGN}}{r_{\rm eff,NSC}}, \quad (74)$$

where $r_{\rm AGN}$ is the typical size of the AGN disk. The sizes of the AGN disks are highly uncertain. Radiation hydrodynamical simulations suggest that thin dense gas disks extend to parsec scales, which are beyond the dust sublimation radius (e.g., Namekata & Umemura 2016; Wada et al. 2016; Williamson et al. 2019). Mid-infrared observations show that the sizes of AGN disks are

$$r_{\rm AGN} \sim {\rm pc} \left(\frac{L_{\rm bol}}{10^{45}\,{\rm erg}} \right)^{1/2} \sim 0.1\ {\rm pc} M_{\rm SgrA}^{1/2} \left(\frac{f_{\rm Edd}}{0.03} \right)^{1/2} \quad (75)$$

(see Figure 36 in Burtscher et al. 2013), where $L_{\rm bol}$ is the bolometric luminosity of an AGN disk. We set $r_{\rm AGN} = r_{\rm AGN,MW} (M_{\rm SMBH}/4 \times 10^6\,M_\odot)^{1/2}$ assuming a fixed Eddington accretion rate as in Equation (75), where $r_{\rm AGN,MW}$ is the size of the AGN disk for $M_{\rm SMBH} = 4 \times 10^6\,M_\odot$.

We substitute the $M_{\rm SMBH}$ dependence of $r_{\rm eff,NSC}$ and $N_{\rm BH,NSC}$ in Equation (74) using empirical correlations as follows. The number of BHs may be expressed with the stellar mass of the nuclear star cluster as

$$N_{\rm BH,NSC} = \eta_{\rm n,BH} M_{\rm NSC}, \quad (76)$$

where the parameter $\eta_{\rm n,BH} \sim 0.002\,M_\odot^{-1}$ represents the number of BHs per unit stellar mass for a Salpeter IMF (but see the discussion below for BHs in nuclear star clusters). The mass of the nuclear star cluster follows

$$M_{\rm NSC} = 4.3 \times 10^6\,M_\odot \left(\frac{\sigma_{\rm Bulge}}{54\ {\rm km\ s^{-1}}} \right)^{2.11} \quad (77)$$

(Scott & Graham 2013), where the velocity dispersion of the bulge is given by (Kormendy & Ho 2013)

$$\sigma_{\rm Bulge} = 200\ {\rm km\ s^{-1}} \left(\frac{M_{\rm SMBH}}{3.1 \times 10^8\,M_\odot} \right)^{0.228}. \quad (78)$$

The radius of the nuclear star clusters in late-type galaxies is expressed as (Georgiev et al. 2016)

$$r_{\rm eff,NSC} = 3.23\ {\rm pc} \left(\frac{M_{\rm NSC}}{3.6 \times 10^6\,M_\odot} \right)^{0.321}. \quad (79)$$

Thus, $r_{\rm AGN}/r_{\rm eff,NSC}$ in Equation (74) increases from 0.01 to 0.1 as $M_{\rm SMBH}$ increases from 10^5 to $10^9\,M_\odot$.

Following Bartos et al. (2017), we use the log-normal fit to the observed AGN mass function in the local universe (Greene & Ho 2007, 2009) in Equation (73):

$$\frac{dn_{\rm AGN}}{dM_{\rm SMBH}} = \frac{3.4 \times 10^{-5}\,{\rm Mpc^{-3}}}{M_{\rm SMBH}} \times 10^{-[\log(M_{\rm SMBH}/M_\odot) - 6.7]^2/1.22}. \quad (80)$$

This mass function includes low-luminosity AGNs with Eddington ratios of $f_{\rm Edd} \equiv L/L_{\rm Edd} = 0.01$. We include mergers in such low-luminosity AGNs as the rate of mergers from preexisting BHs is not very sensitive to the accretion rate onto the SMBH (models 1, 9, 10). Below $f_{\rm Edd} \approx 0.01$ geometrically thin AGN disks transition to geometrically thick advection-dominated accretion flows (Narayan & McClintock 2008). In such low-density flows, it is not obvious if mergers proceed as we modeled in this paper. Here, to be conservative, we consider the rate of mergers only in AGN disks with $f_{\rm Edd} \gtrsim 0.01$.

By integrating Equation (73) between $M_{\rm SMBH,min} = 10^5\,M_\odot$ and $M_{\rm SMBH,max} = 10^9\,M_\odot$ using the assumptions above, we

[12] Note, however, that we use the $e = 0$ approximation to simulate the evolution of binaries. Binaries may be hardened more efficiently by GWs at a somewhat lower frequency for higher eccentricity than shown in Figure 18. Thus, LISA may detect the GWs of stellar-mass BH and IMBH binaries embedded in AGNs where astrophysical environmental effects are still significant (see also Kocsis et al. 2011; Barausse et al. 2015). For these binaries, the mean inspiral rate ($df_{\rm GW}/dt$, the "chirp") is higher than that of an isolated binary in vacuum, which leads to an astrophysical GW phase shift for nonstationary sources (see also Kocsis et al. 2011; Yunes et al. 2011; Derdzinski et al. 2019). For nearly stationary GW sources (with respect to the observation time), the $f_{\rm GW}$ distribution of binaries may be used to measure the residence time that the binaries spend at a particular frequency to infer the underlying astrophysical mechanism driving the evolution of the binary separation (Kocsis & Sesana 2011a).

find

$$\mathcal{R}_{\rm sBH} \sim 3\ {\rm Gpc^{-3}\ yr^{-1}} \left(\frac{f_{\rm BH,mer}}{0.5}\right)\left(\frac{t_{\rm AGN}}{30\ {\rm Myr}}\right)^{-1} \times \left(\frac{r_{\rm AGN,MW}}{0.1\ {\rm pc}}\right)\left(\frac{\eta_{\rm n,BH}}{0.005\ M_\odot^{-1}}\right). \quad (81)$$

The relative contribution of the mass ranges $M_{\rm SMBH} = 10^{5-6}$, 10^{6-7}, 10^{7-8}, and $10^{8-9}\ M_\odot$ are 0.96%, 34%, 59%, and 6.1%, respectively. The rate is dominated by $M_{\rm SMBH} \approx 10^{7-8}\ M_\odot$; this is because the peak of the AGN mass function is at $10^{6.7}\ M_\odot$ (Greene & Ho 2007) and the number of BHs crossing the AGN disk increases with $M_{\rm SMBH}^{0.83}$.

5.5.2. Uncertainties in the Merger Rate Estimate

The merger rate estimate in AGNs is parameterized in Equation (81) with the merger fraction per AGN lifetime $f_{\rm BH,mer}/t_{\rm AGN}$, the radius of the AGN for a Milky Way–size galaxy, $r_{\rm AGN,MW}$, and the number of BHs per unit mass in the nuclear star cluster. The uncertainties in these parameters may be estimated as follows.

The radius of the AGN disk based on mid-infrared observations is given by Equation (75). We assume that the allowed range of $r_{\rm AGN,MW} = 0.06$–0.2 pc for $M_{\rm SMBH} = 4 \times 10^6\ M_\odot$, considering that the merger rate is dominated by low-luminosity AGNs with $f_{\rm Edd} = 0.01$–0.1 (Kelly & Shen 2013).

Table 3 shows the value of $f_{\rm BH,mer}$ for the different models. For a stationary accretion disk with a fixed accretion rate and Eddington rate, the merger fraction per unit time ($f_{\rm BH,mer}/t$) is 1.7×10^{-8}, 2.0×10^{-8}, 1.9×10^{-8}, 1.3×10^{-8}, and $6.2 \times 10^{-9}\ {\rm yr^{-1}}$ at 1, 3, 10, 30, and 100 Myr, respectively, in the fiducial model. Compared to its value at 30 Myr, $f_{\rm BH,mer}/t$ is higher by a factor of $\sim$1.6 at 3 Myr and lower by a factor of $\sim$2.1 at 100 Myr. Thus, the merger fraction is correlated with the lifetime of the AGN disk (Figure 7), which reduces the uncertainties of the merger rate caused by the uncertain AGN disk lifetime. From Table 3, the maximum and minimum $f_{\rm BH,mer}/t$ at 30 Myr are $\sim 2.5 \times 10^{-8}$ (model 19) and $\sim 6.7 \times 10^{-10}\ {\rm yr^{-1}}$ (model 2), respectively. Based on these results, we consider a reasonable range of uncertainty to be $f_{\rm BH,mer}/t_{\rm AGN} \sim 3 \times 10^{-10}\ {\rm yr^{-1}}$–$4 \times 10^{-8}\ {\rm yr^{-1}}$, so that $0.018 \lesssim (f_{\rm BH,mer}/0.5)(t_{\rm AGN}/30\ {\rm Myr})^{-1} \lesssim 2.4$ in Equation (81).

In comparison, $f_{\rm BH,mer}/t_{\rm AGN}$ has been poorly constrained in previous studies, with the allowed range as wide as $\sim 5 \times 10^{-13}$–3×10^{-7} (McKernan et al. 2018). The uncertainty in $f_{\rm BH,mer}$ comes from the uncertainties of the binary fraction, the capture fraction of BHs by AGN disks, and the merger fraction of binaries. The typical lifetime of AGN disks ($t_{\rm AGN}$) also has large uncertainties of 1–100 Myr (e.g., Haiman & Hui 2001; Martini & Weinberg 2001; Marconi et al. 2004; Martini 2004). In the present study, we find that binaries are efficiently formed by gas-capture and dynamical mechanisms, and as a result, the merger fraction is relatively insensitive to the highly uncertain preexisting binary fraction (models 1, 29–31). The number of mergers is a factor of 5 smaller than in the fiducial model if the initial BH population is isotropic (model 16, $\beta_v = 1$; see model 1 with $\beta_v = 0.2$.).

For a Salpeter IMF with $\delta_{\rm IMF} = -2.35$, the number of BHs per unit mass $\eta_{\rm n,BH}$ is $\sim 0.002\ M_\odot^{-1}$ if we assume that the mass range of stars is 0.1–140 $M_\odot$ and 20–140 $M_\odot$ stars form BHs. On the other hand, the IMF in galactic centers is suggested to be top heavy, referring to observational ($\delta_{\rm IMF} = -1.7 \pm 0.2$ by Lu et al. 2013) and theoretical studies (Nayakshin et al. 2007). For example, $\eta_{\rm n,BH}$ is $\sim 0.01\ M_\odot^{-1}$ for $\delta_{\rm IMF} = -1.7$. Furthermore, within parsec regions, numerical studies (Miralda-Escude & Gould 2000; Freitag et al. 2006; Hopman & Alexander 2006; Antonini 2014) show that the number of BHs per unit mass $\eta_{\rm n,BH}$ is enhanced by mass segregation by a factor of $\sim$2. We assume that the range of $\eta_{\rm n,BH}$ is ~ 0.002–$0.02\ M_\odot^{-1}$, allowing for the possibility of both a top-heavy IMF and mass segregation.

In summary, with the uncertainties adopted above, $f_{\rm BH,mer}/t_{\rm AGN} = (3$–$400) \times 10^{-10}\ {\rm yr^{-1}}$, $r_{\rm AGN,MW} = 0.06$–0.2 pc, and $\eta_{\rm n,BH} = 0.002$–$0.02\ M_\odot^{-1}$, the allowed range of merger rates is estimated to be

$$0.02\ {\rm Gpc^{-3}\ yr^{-1}} \lesssim \mathcal{R}_{\rm sBH} \lesssim 60\ {\rm Gpc^{-3}\ yr^{-1}}. \quad (82)$$

In comparison, the current measurement of the merger rate using the LIGO–VIRGO observations is in the range of 9.7–101 ${\rm Gpc^{-3}\ yr^{-1}}$ (Abbott et al. 2019a). Thus, mergers in AGN disks are plausible candidates for the observed GW events.

5.5.3. Extreme-mass-ratio Inspirals

We next predict the rate of extreme-mass-ratio inspirals (EMRIs). EMRIs into SMBHs of $\sim 10^4$–$10^7\ M_\odot$ are promising targets for future low-frequency GW observations by LISA (Amaro-Seoane et al. 2007). In our simulation, the inner boundary is at 10^{-4} pc, which corresponds to $\sim 530\ R_g$ for a $4 \times 10^6\ M_\odot$ SMBH. The distance from which a $5\ M_\odot$ BH on a circular orbit can migrate to the SMBH within a Hubble time via GW radiation is $\sim 1000\ R_g$. However, if BHs accumulate at migration traps ($\lesssim 490\ R_g$) and repeatedly merge with one another (Bellovary et al. 2016; Secunda et al. 2019; Yang et al. 2019a, 2019b; Gayathri et al. 2020; but see also Dittmann & Miller 2020), the number of BHs that can spiral into SMBHs may decrease significantly. Thus, not all BHs that migrate within our inner boundary may spiral into the SMBH, and so $N_{\rm acc}$ is an upper limit for the number of EMRIs. According to the results of our simulations (Table 3), $N_{\rm acc} \sim 1$–5 at 30 Myr. If we assume that $N_{\rm acc}$ is independent of $\dot{M}_{\rm SMBH}$ and most AGNs are low-luminosity AGNs with $\sim 0.01\ f_{\rm Edd}$ (Kelly & Shen 2013), and $N_{\rm acc}$ is roughly proportional to time (brown line in Figure 6), the number of BHs accreted onto the SMBH per accreted gas mass can be approximated as $N_{\rm acc}/(\dot{M}_{\rm out} t_{\rm AGN}) \sim (4$–$20) \times 10^{-5}\ M_\odot^{-1}$. Then, we can roughly estimate the EMRI event rate density as

$$R_{\rm EMRI} \sim \frac{N_{\rm acc}\dot{\rho}_{\rm SMBH}}{t_{\rm AGN}\dot{M}_{\rm SMBH}} \sim (0.1\text{–}0.6)\,{\rm Gpc^{-3}\ yr^{-1}} \left[\frac{N_{\rm acc}/(\dot{M}_{\rm SMBH} t_{\rm AGN})}{(4\text{–}20) \times 10^{-5}\ M_\odot^{-1}}\right] \times \left(\frac{\dot{\rho}_{\rm SMBH}}{3 \times 10^3\ {\rm Gpc^{-3}} M_\odot\ {\rm yr^{-1}}}\right), \quad (83)$$

where $\dot{\rho}_{\rm SMBH}$ is the total mass accretion rate onto all SMBHs in the local universe, and we adopt $\dot{\rho}_{\rm SMBH} = 3 \times 10^3\ M_\odot\,{\rm Gpc^{-3}\ yr^{-1}}$ (Marconi et al. 2004). If the EMRI rate by migration in AGN disks is ~ 0.1–$0.6\ {\rm Gpc^{-3}\ yr^{-1}}$, this channel may largely contribute to the EMRI rate, as the EMRI rate by stellar relaxation processes is

predicted to be comparable, $\sim$0.02–2 Gpc^{-3} yr^{-1} (e.g., Miller et al. 2005; Freitag et al. 2006; Hopman & Alexander 2006; Amaro-Seoane et al. 2007; Amaro-Seoane & Preto 2011; Aharon & Perets 2016; Bar-Or & Alexander 2016; Babak et al. 2017). Even if repeated mergers take place at migration traps and reduce the number of EMRIs significantly, at least one massive BH can migrate and merge with the central SMBH during each AGN phase of every galaxy, which can be observed as intermediate-mass-ratio inspirals (IMRIs; e.g., Derdzinski et al. 2019). Note that the LISA detection rate is enhanced by the increased detection volume that corresponds to the increased migrator mass following repeated mergers.

In our simulation, all BHs that migrate within the inner boundary $R_{\rm min}$ are single (not binary). This is because binaries either merge or are disrupted by binary–single interactions before they migrate to $R_{\rm min}$.

5.6. Comparison with Previous Works

In this section, we compare our models and results with those in previous works on BH mergers in AGN disks by Bartos et al. (2017) and Stone et al. (2017). A major difference between the present study and earlier works is that we here model the time-evolving system explicitly, enabling us to follow the formation and destruction of binaries, together with the evolution of their separation, their center-of-mass velocity, and their radial distance from the SMBH consistently.

Bartos et al. (2017) considered the capture of binaries due to linear momentum exchange with an AGN disk within 0.01 pc from the SMBH, and the hardening of binaries by the gas dynamical friction of the AGN disk and type I/II torques of a circumbinary disk. Bartos et al. (2017) found the merger rate to be $\sim$1.2 Gpc^{-3} yr^{-1}. Our study is a more detailed and extended version of Bartos et al. (2017). One difference between Bartos et al. (2017) and this work is the binary fraction. Bartos et al. (2017) considered the evolution of preexisting binaries, whose fraction is assumed to be 0.3, while our study finds that a large fraction of single BHs captured within AGN disks later form binaries by gas-capture and dynamical mechanisms. A second difference is the assumption of the BH distribution. Bartos et al. (2017) assumed an isotropic velocity distribution, in which the merger rate is lower by a factor of $\sim$6 than the anisotropic velocity distributions adopted here (see models 1 and 13–16 in Table 3). Such anisotropic velocity distribution is predicted by theoretical (Kocsis & Tremaine 2011b; Szolgyen & Kocsis 2018) and observational studies (Trippe et al. 2008; Feldmeier et al. 2014, 2015; Yelda et al. 2014). Also Bartos et al. (2017) assumed the strongly mass-segregated number density of $\gamma_\rho = 0.5$, while our study assumes $\gamma_\rho = -0.5$ to 0 (models 1, 22). A third difference is the assumed size of the AGN disks. Bartos et al. (2017) consider a size of 0.01 pc, compared to the $\sim$0.03–0.1 pc $(M_{\rm SMBH}/4\times10^6\,M_\odot)^{1/2}$ adopted here. The larger disk sizes are motivated by observations of AGN disks (Burtscher et al. 2013).

Stone et al. (2017) considered the evolution of binaries formed in situ in AGN disks at $\sim$parsec from the SMBH. Both Stone et al. (2017) and our study use the disk model proposed by Thompson et al. (2005) and consider the hardening by type I/II torque and binary–single interactions. The differences are that we treat binary–single interactions considering the evolution of the distribution of BHs, and we include the new mechanism of gas capture to form new binaries. Stone et al. (2017) estimated the merger rate from in situ formed binaries to be $\sim$3 Gpc^{-3} yr^{-1}, in which the binary fraction (the binary number over the BH number) and the merger fraction are assumed to be 0.56 and 1, respectively. In our simulation, the fraction of the number of mergers from in situ formed BHs ($N_{\rm mer,SF}$) over the number of in situ formed BHs ($N_{\rm SF}$) is $\sim$0.14–0.67 in models 1, 9, 10, and 23–25. Note that these values are upper limits, as we assume that BHs form immediately at star formation. Following the estimate in Stone et al. (2017), we find the merger rate density for in situ formed BHs to be

$$R_{\rm IS} \sim f_{\rm SF/AGN}\,(N_{\rm mer,SF}/N_{\rm SF}) f_{\rm BH}\,\dot\rho_{\rm SMBH}/\bar m_{\rm BH} \sim 0.7\text{–}22\ {\rm Gpc^{-3}\ yr^{-1}}, \quad (84)$$

where $\bar m_{\rm BH}$ is the average BH mass, $f_{\rm BH}$ is the mass fraction of BHs over stars, $\dot\rho_{\rm SMBH}$ is the total mass accretion rate onto all SMBHs in the local universe, and $f_{\rm SF/AGN}$ is the star formation rate within the AGN disk over the accretion rate onto the SMBH. In the estimate above, we use $f_{\rm SF/AGN} = 1$ and $\dot\rho = 3\times10^3\,M_\odot{\rm Gpc^{-3}}$ (Marconi et al. 2004) as adopted in Stone et al. (2017). For a top-heavy IMF with $\delta_{\rm IMF} = 1.7 - 2.35$ (Lu et al. 2013), we find $f_{\rm BH} = 0.016$–0.092 and $\bar m_{\rm BH} = 8.4$–$9.2\,M_\odot$. Because these differences are relatively small, our estimated rate is consistent with that by Stone et al. (2017). We find that mergers between preexisting BHs captured by AGN disks ($\sim$0.02–60 Gpc^{-3} yr^{-1}) are roughly comparable to the mergers from BHs formed in situ in AGN disks ($\sim$0.7–22 Gpc^{-3} yr^{-1}).

5.7. Ignored Effects

In this section, we discuss several effects that have been ignored in our model.

5.7.1. Heating of AGN Disks

We first discuss several heating processes that we have not included. All heating rates must be compared to the cooling rate of the disk, which we show for our fiducial disk model in Figure 19 by the black curve. The effective volumetric cooling rate is given by

$$\Lambda_{\rm cool} \sim \frac{\sigma_{\rm SB}T_{\rm eff}^4}{h_{\rm disk}}V, \quad (85)$$

where $V = 4\pi r_l \Delta r_l h_{\rm disk}$ is the disk's volume in the cell r_l, $T_{\rm eff}$ is the effective surface temperature, and $\sigma_{\rm SB}$ is the Stefan–Boltzmann constant. In the outer regions ($r \gtrsim 0.3$ pc), gas is optically thin and is stabilized by star formation feedback.

In addition to the α viscosity and star formation feedback, which are implicitly part of our disk model, there are several processes that heat the AGN disk that we have not taken into account:

(i) damping of the orbital velocity of stars and compact objects in the spherical cluster when they cross the AGN disk,
(ii) torques operating on single objects and (the center of mass of) binaries embedded in the AGN disk,

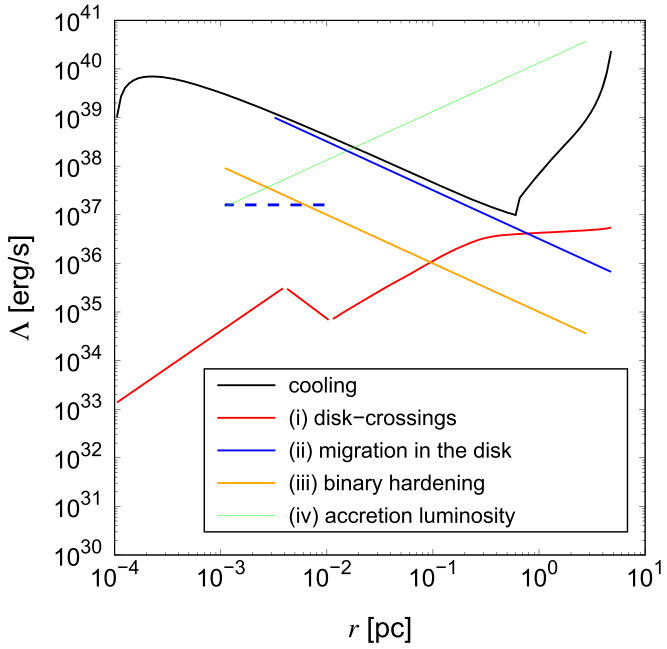

Figure 19. Cooling and heating rates in each cell l as a function of the distance from the SMBH for the fiducial model. Solid and dashed black lines correspond to the optically thick and thin cooling rates. Red, blue, orange, and green lines correspond to heating via the processes of (i) disk crossings, (ii) migration in the disk, (iii) binary hardening, and (iv) accretion luminosity, respectively. Solid and dashed blue lines present the heating rate due to migration torque and damping of velocity by gas dynamical friction, respectively.

(iii) hardening of binaries, as well as
(iv) radiation feedback from accretion onto stellar-mass BHs.

We estimate the order of magnitude of these effects in turn below.

First, we consider the total heating rate due to the damping of the velocities of a spherical cluster of stars during disk crossings (process (i)). During one orbital period around the SMBH, the orbital velocity of an object is damped by $\Delta v \sim v_{\rm orb}\Delta M_{\rm cross}/m_i$ (e.g., Bartos et al. 2017), where $\Delta M_{\rm cross} = \pi[\max(r_{\rm BHL}, R_{{\rm star},i})]^2 h_{\rm cross}\rho_{\rm gas}$ is the gas mass that passes within the Bondi–Hoyle–Lyttleton radius of the object when crossing the disk (twice per orbit), $h_{\rm cross} \sim 2h_{\rm disk}/\sin\iota$ is the distance in which the object crosses the disk, where ι is the inclination of the orbit, and recall that $h_{\rm disk}$ is the disk half-thickness and $v_{\rm orb}$ is the orbital velocity of the object. In practice, $r_{\rm BHL}$ is smaller than the Hill radius (Equation (15)) if the orbital inclination satisfies $\iota \gtrsim = 3^{1/6}(m_i/M_{\rm SMBH})^{1/3} = 5\times 10^{-3}(m_i/0.36M_\odot)^{1/3}$, so the accretion rate during disk crossing is typically not limited by the Hill radius.[13] If this condition holds and if $\sin\iota \geqslant h_{\rm disk}/r$, then for circular orbits $r_{\rm BHL}$ is determined by the ι inclination of the orbit as[14]

$$r_{\rm BHL} = \frac{Gm_i}{c_s^2 + v_i^2} \approx \frac{Gm_i}{2(1-\cos\iota)v_{\rm orb}^2} = \frac{\cos^2\frac{\iota}{2}}{\sin^2\iota}\frac{m_i}{M_{\rm SMBH}}r. \tag{86}$$

Because $v_{\rm orb} \gg \Delta v$, the kinetic energy-loss rate averaged over an orbit is $\sim m_i\Delta v v_{\rm orb}/t_{\rm orb}$. The total heating rate by damping of the orbital velocity of all stars in cell l is estimated to be

$$\begin{aligned}\Lambda_{\rm i,damp} &\sim \frac{N_{{\rm ob},l}m_i\Delta v v_{\rm orb}}{t_{\rm orb}} = N_{{\rm ob},l}\frac{\cos^4\frac{\iota}{2}}{\sin^5\iota}\frac{G^{3/2}m_i^2\rho_{\rm gas}h_{\rm disk}}{M_{\rm SMBH}^{1/2}r^{1/2}}\\ &\sim 2\times 10^{34}\ {\rm erg\ s^{-1}}\left(\frac{N_{{\rm ob},l}}{2\times 10^4}\right)\frac{m_i^2}{(0.36\,M_\odot)^2}\\ &\times\left(\frac{M_{\rm SMBH}}{4\times 10^6\,M_\odot}\right)^{-1/2}\left(\frac{r_l}{0.1\ {\rm pc}}\right)^{-2.5}\\ &\times\left(\frac{\rho_{\rm gas}r_l^3}{7\times 10^5\,M_\odot}\right)\left(\frac{h_{\rm disk}/r_l}{10^{-3}}\right)\left(\frac{\sin\iota}{0.3}\right)^{-5}\\ &\quad {\rm for}\ R_{{\rm star},i} < r_{\rm BHL},\end{aligned} \tag{87}$$

and

$$\begin{aligned}\Lambda_{\rm i,damp} &= N_{{\rm ob},l}\frac{G^{3/2}M_{\rm SMBH}^{3/2}R_{\rm star}^2\rho_{\rm gas}h_{\rm disk}}{\sin\iota\, r^{5/2}}\\ &\sim 4\times 10^{32}\ {\rm erg\ s^{-1}}\left(\frac{N_{{\rm ob},l}}{2\times 10^4}\right)\left(\frac{m_i}{0.36\,M_\odot}\right)\\ &\times\left(\frac{M_{\rm SMBH}}{4\times 10^6\,M_\odot}\right)^{3/2}\left(\frac{r_l}{0.1\ {\rm pc}}\right)^{-4.5}\\ &\times\left(\frac{\rho_{\rm gas}r_l^3}{7\times 10^5\,M_\odot}\right)\left(\frac{h_{\rm disk}/r_l}{10^{-3}}\right)\left(\frac{\sin\iota}{0.3}\right)^{-1}\\ &\quad {\rm for}\ R_{{\rm star},i} > r_{\rm BHL},\end{aligned} \tag{88}$$

where $N_{{\rm ob},l}$ is the number of objects[15] in cell l and $R_{{\rm star},i}$ is given by Equation (5). Additionally, the total heat of process (i) is limited by the initial kinetic energy of objects in the Keplerian corotating frame with the gas.[16] If we average the total heat over $t_{\rm AGN}$, the upper limit for the time-averaged heating rate by disk crossing is given by

$$\begin{aligned}\Lambda_{\rm i,lim} &\sim \frac{N_{{\rm ob},l}m_i(2v_{\rm orb})^2}{2t_{\rm AGN}}\\ &\sim 5\times 10^{37}\ {\rm erg\ s^{-1}}\left(\frac{N_{{\rm ob},l}}{2\times 10^4}\right)\left(\frac{m_i}{0.36\,M_\odot}\right)\\ &\times\left(\frac{M_{\rm SMBH}}{4\times 10^6\,M_\odot}\right)\left(\frac{r_l}{0.1\ {\rm pc}}\right)^{-1}\left(\frac{t_{\rm AGN}}{30\ {\rm Myr}}\right)^{-1}.\end{aligned} \tag{89}$$

The red curve in Figure 19 shows $\min(\Lambda_{\rm i,damp}, \Lambda_{\rm i,lim})$. For $R_{{\rm star},i} > r_{\rm BHL}$ ($r \lesssim 0.2\ {\rm pc}\times\sin^2\iota/\cos^2(\iota/2)$, Equation (88)), we assume $1/\sin\iota = 1.5$ as a typical inclination for isotropic orbits.

[13] For $\iota \lesssim 5\times 10^{-3}$, Bondi accretion must be limited to the Hill sphere, which reduces the accretion rate by $(r_{\rm Hill}/r_{\rm BHL})^2$.

[14] Recall that v_i is the relative velocity with respect to the gas that follows the equatorial Keplerian orbit.

[15] Because we have $N_{\rm bin} = 120$ bins with a log-uniform distribution in radius between $r_{\rm max} = 5$ pc and $r_{\rm min} = 10^{-4}$ pc, $\Delta r/r = (\ln\Lambda)/N_{\rm bin}$, where $\ln\Lambda = \ln(r_{\rm max}/r_{\rm min})$ and the number density of objects in the spherical component $n(r)$ is given by Equation (7), and the number of objects in a cell at r is $N_{{\rm ob},l}(r) = 4\pi r^2 n(r)\Delta r$, which scales as $\propto r^{2.5}$ for $r \ll 0.3$ pc and $\propto r^{1.2}$ for $r \gg 0.3$ pc.

[16] Assuming that the gravitational potential is dominated by the SMBH.

On the other hand, because the heating rate for $R_{\mathrm{star},i} < r_{\mathrm{BHL}}$ (Equation (87)) is sensitive to $\sin\iota$, the allowed values for $\sin\iota$ need to be examined carefully. Even if the heating rate is much higher than the AGN cooling rate, this may still be a small effect if the heating timescale is very short. Although stars with small $\sin\iota$ strongly heat gas as $\Lambda_{\mathrm{i,damp}} \propto \sin\iota^{-5}$, the probability (timescale) for a star to have ι also scales with $\sin\iota^{5}$ while $r_{\mathrm{BHL}} < r_{\mathrm{Hill}}$. Thus, the product of the heating rate at ι and the timescale for a star to have ι is roughly constant. On the other hand, the maximum dissipated energy during the AGN lifetime differs for different ι. We assume that the upper limit for the heating rate averaged on the AGN lifetime is given by setting all stars to have the inclination ι_{cap} at which the relative velocities of stars are damped on the AGN lifetime. Such inclination is derived to satisfy $v_{\mathrm{rel}}/t_{\mathrm{AGN}} = \Delta v/t_{\mathrm{orb}}$. Assuming $v_{\mathrm{rel}} \sim v_{\mathrm{orb}}\sin\iota$,

$$(\sin\iota_{\mathrm{cap}}) \sim \left(\frac{t_{\mathrm{AGN}}}{t_{\mathrm{orb}}}\frac{4\pi m_i \rho_{\mathrm{gas}} h_{\mathrm{disk}} r^2}{M_{\mathrm{SMBH}}^2}\right)^{1/6} \sim 0.13 \times \left(\frac{\rho_{\mathrm{gas}} r_l^3}{7\times10^5\,M_\odot}\right)^{1/6}\left(\frac{h_{\mathrm{disk}}/r_l}{10^{-3}}\right)^{1/6} \times \left(\frac{m_i}{0.36\,M_\odot}\right)^{1/6}\left(\frac{M_{\mathrm{SMBH}}}{4\times10^6\,M_\odot}\right)^{-1/4} \times \left(\frac{r_l}{0.1\ \mathrm{pc}}\right)^{-1/4}\left(\frac{t_{\mathrm{AGN}}}{30\ \mathrm{Myr}}\right)^{1/6}. \quad (90)$$

We use i_{cap} to estimate the heating due to disk crossing for $R_{\mathrm{star},i} < r_{\mathrm{BHL}}$ ($r \gtrsim 10^{-2}$ pc) in Figure 19. Because the fraction of stars having $v_{\mathrm{rel}} \lesssim \iota_{\mathrm{cap}} v_{\mathrm{orb}}$ over all stars is $\lesssim\iota_{\mathrm{cap}}$, and the average heating rate for stars with $\iota > \iota_{\mathrm{cap}}$ rapidly decreases, the average heating rate is overestimated by $\sim 1/\iota_{\mathrm{cap}}$.

On the other hand, for $R_{\mathrm{star},i} < r_{\mathrm{BHL}}$, the heating rate using $m_i = 0.36 M_\odot$ in Equation (87) underestimates the true heating rate because $\Lambda_{i,\mathrm{damp}} \propto m_i^2$ and $\langle m^2\rangle$ may be much larger than $\langle m\rangle^2$, and so massive stars dominate the heating due to the strong dependence on mass. If we assume preexisting stars are mostly old ($\gtrsim$a few 100 Myr), the maximum mass of massive stars is $\sim 3\,M_\odot$. Here we consider the extreme case that all stars are as massive as $3\,M_\odot$. As the mass of a stellar cluster is fixed, $N_{\mathrm{ob},l}$ for $m_i = 3\,M_\odot$ is lowered by a factor of $\sim$10 compared to that for $m_i = 0.36\,M_\odot$. Then, $\Lambda_{\mathrm{i,damp}} \propto N_{\mathrm{ob},l}\langle m^2\rangle$ is enhanced by a factor of $\sim$10 compared with Equation (87) for $m_i = 0.36 M_\odot$.

In conclusion, the dynamical heating rate by disk crossing of stars (process (i)) may exceed the cooling rate at $r \sim 0.5$ pc. If the number of BHs compared to the number of stars is between 10^{-4}–10^{-3}, and the typical BH mass is 10–100 times larger than the typical stellar mass, the heating due to disk crossing $\Lambda_{\mathrm{i,damp}} \propto N_{\mathrm{ob},l} m_i^2$ (Equation (87)) may be comparable to that of stars within a factor 10.

Next, we consider heating corresponding to torques operating on objects embedded in the disk (process (ii)). Because these objects are assumed to migrate toward the SMBH via gas torques, the disk can be heated by the corresponding increase in these objects' binding energy. If we assume that roughly half of all BHs migrate to $\sim 10^{-3}$–10^{-2} pc in our models (see the black line in panel (a) of Figure 10), the total dissipation rate in cell l, averaged over t_{AGN}, is

$$\Lambda_{\mathrm{ii,mig}} \sim \frac{N_{\mathrm{mig}} G m_i M_{\mathrm{SMBH}}}{t_{\mathrm{AGN}}}\left(\frac{1}{r_l - \Delta r_l} - \frac{1}{r_l}\right) \sim 3\times10^{36}\ \mathrm{erg\ s^{-1}}\left(\frac{N_{\mathrm{mig}}}{10^4}\right)\left(\frac{m_i}{10\,M_\odot}\right) \times \left(\frac{M_{\mathrm{SMBH}}}{4\times10^6\,M_\odot}\right)\left(\frac{r_l}{1\ \mathrm{pc}}\right)^{-1}\left(\frac{\Delta r_l/r_l}{0.08}\right)\left(\frac{t_{\mathrm{AGN}}}{30\ \mathrm{Myr}}\right), \quad (91)$$

where N_{mig} is the number of objects that migrated to $r \lesssim 10^{-2}$ pc. $\Delta r_l/r_l = 0.08$ is the value adopted in the fiducial model ($N_{\mathrm{cell}} = 120$). The solid blue line in Figure 19 presents $\Lambda_{\mathrm{ii,mig}}$, with parameter values as in Equation (91). We can see that this heating rate roughly matches the cooling rate in the optically thick region ($r \lesssim 0.3$ pc), but is significantly below it in the optically thin region ($r \gtrsim 0.3$ pc). As the number of objects in the AGN disk varies with time (cyan line in Figure 6), the heating rate can momentarily be even higher than the average value in Equation (91), which may require revisions of the AGN disk model.

Equation (91) ignores the contribution from stars for simplicity. In our simulation, the total mass of stars captured by the AGN disk over 30 Myr is $\sim 10^5\,M_\odot$ (brown line in panel (a) of Figure 10). If all these stars migrate to $\lesssim 10^{-2}$ pc, the heating rate is enhanced by a factor of 2 compared to Equation (91). However, the migration timescale is inversely proportional to the mass of migrating objects as long as a gap does not form, which suggests that typical-mass stars ($\sim 0.36\,M_\odot$) do not migrate inward within 30 Myr if they begin at $r \gtrsim 0.2$ pc (blue line in panel (c) of Figure 10). This suggests a minor contribution from stars to heating compared with BHs.

After binary BHs migrate within $\sim 10^{-2}$ pc of the SMBH, they receive kicks due to binary–single interactions, which dominate the heating of the orbital velocities of binaries (e.g., panel (c) of Figure 5). Following each kick, the center-of-mass velocity of the binary is damped by gas dynamical friction, heating the disk. If we assume that each binary experiences $N_{\mathrm{damp}} \sim 10$ binary–single interactions, the total energy transferred to the disk can be estimated as

$$E_{\mathrm{ii,damp}} \sim \frac{1}{2} m_{\mathrm{tot,cap}} v_{\mathrm{typ}}^2 N_{\mathrm{damp}} \sim 4\times10^{53}\ \mathrm{erg}\frac{m_{\mathrm{tot,cap}}}{10^5\,M_\odot}\left(\frac{v_{\mathrm{typ}}}{200\ \mathrm{km\ s^{-1}}}\right)^2\frac{N_{\mathrm{damp}}}{10}, \quad (92)$$

where v_{typ} is the typical excess velocity damped by gas dynamical friction, $m_{\mathrm{tot,cap}}$ is the total mass of binaries captured by the AGN disk, and N_{damp} is the typical number of velocity-damping episodes per binary. If we spread this total energy over the total simulation time of 30 Myr, the corresponding average heating rate is

$$\Lambda_{\mathrm{ii,damp}} \sim E_{\mathrm{ii,damp}}/t_{\mathrm{AGN}} \sim 4\times10^{38}\ \mathrm{erg\ s^{-1}}\left(\frac{E_{\mathrm{ii,damp}}}{10^{53}\ \mathrm{erg}}\right)\left(\frac{t_{\mathrm{AGN}}}{30\ \mathrm{Myr}}\right)^{-1}. \quad (93)$$

We further assume that binary–single interactions occur uniformly between 10^{-2}–10^{-3} pc, where mergers typically occur (panel (b) of Figure 10). The heating rate under these

assumptions is shown by the dashed blue line in Figure 19. We can see that this process represents a relatively minor contribution compared with the cooling or other heating processes. We speculate that $\Lambda_{\rm ii,damp}$ is not strongly time dependent, as the number of merged binaries is roughly proportional to the elapsed time (Figure 7).

Interactions with the gas disk also harden BH binaries (process (iii)), further heating the ambient gas. According to Figure 9, binaries are hardened by gas dynamical friction and type I/II torques to $s \sim 10^{-6}$ pc at $r \sim 10^{-2}$ pc and to $s \sim 10^{-4}$ pc at $r \sim 1$ pc in the AGN disk. For simplicity, we assume that binaries harden to $s \sim 10^{-4}r$. Then, the corresponding heating rate as a function of distance from the SMBH is approximately

$$\Lambda_{\rm iii,hard} \sim \frac{N_{\rm hard,bin} G m_1 m_2}{t_{\rm AGN}}\left(\frac{1}{s-\Delta s}-\frac{1}{s}\right) \sim 10^{36}\,{\rm erg\,s^{-1}}\left(\frac{N_{\rm hard,bin}}{10^4}\right)\left(\frac{m_1}{10\,M_\odot}\right)\left(\frac{m_2}{10\,M_\odot}\right) \times\left(\frac{r_l}{1\,{\rm pc}}\right)^{-1}\left(\frac{\Delta r_l/r_l}{0.08}\right)\left(\frac{t_{\rm AGN}}{30\,{\rm Myr}}\right)^{-1}, \quad (94)$$

which is shown by the orange line in Figure 19. Although we assume that all binaries are hardened as they migrate, if all binaries form in some cell and they are hardened to $s \sim 10^{-4}r$, $\Lambda_{\rm iii,hard}$ is enhanced by a factor of 10, which is slightly lower than the cooling rate (black lines). Hence, we estimate that the heating by process (iii) does not affect the disk properties.

To estimate the radiation luminosity from accretion onto stellar-mass BHs (process (iv)), we assume that the number of BHs in the disk at cell l follows $N_{{\rm disk},l} \sim 40(r_l/3\,{\rm pc})$ for $r_l < 3$ pc. This is motivated by the initial BH distribution, which remains roughly in place at $t = 30$ Myr (cyan and blue lines in panel (a) of Figure 10). The luminosity of the population of stellar-mass BHs can then be estimated by

$$L_{\rm vi,rad} \sim N_{{\rm disk},l} L_{\rm Edd}\Gamma_{\rm Edd,cir} \sim 4\times10^{40}\,{\rm erg\,s^{-1}}\left(\frac{r_l}{3\,{\rm pc}}\right)\left(\frac{m_{\rm BH}}{10\,M_\odot}\right)\left(\frac{\Gamma_{\rm Edd,cir}}{1}\right), \quad (95)$$

which is shown by the green line in Figure 19. This luminosity exceeds the cooling rate at $r \gtrsim 10^{-2}$ pc, which is consistent with the estimate by Levin (2003). However, the majority of this radiation might escape in directions perpendicular to the AGN disk due to predicted anisotropic radiation (e.g., Sugimura et al. 2018) and the small disk height compared with the Bondi–Hoyle–Lyttleton radii and the Hill radii. Also, the H II regions are mostly confined inside the Bondi–Hoyle–Lyttleton radii in simulations. In this case, the gas on larger scales is not affected by radiation feedback (e.g., Toyouchi et al. 2020). Here, the size of H II regions for stellar-mass BHs at $r \sim$ pc in the AGN disk is

$$R_{\rm H\,II} \sim 0.01\,{\rm pc}\left(1+710\frac{Z}{Z_\odot}\right)^{-1/3}\left(\frac{m_i}{10\,M_\odot}\right)^{1/3} \times\left(\frac{\rho_{\rm gas}}{10^6\,M_\odot\,{\rm pc^{-3}}}\right)^{-2/3}\left(\frac{\sqrt{c_s^2+v_i^2}}{1\,{\rm km\,s^{-1}}}\right)^{-4/3} \quad (96)$$

(Toyouchi et al. 2020), where Z is the metallicity of gas and $Z_\odot$ is the solar value, while the Bondi–Hoyle–Lyttleton radius is

$$r_{\rm BHL} \sim 0.04\,{\rm pc}\left(\frac{m_i}{10\,M_\odot}\right)\left(\frac{\sqrt{c_s^2+v_i^2}}{1\,{\rm km\,s^{-1}}}\right)^{-2}. \quad (97)$$

Due to the small filling factor of the H II regions, we expect that process (iv) does not significantly affect gas properties on large scales in the inner regions ($r \lesssim$ pc) of the AGN disk. On the other hand, in the outer regions ($r \gtrsim$ a few pc), because the H II regions become larger than the Bondi–Hoyle–Lyttleton radii, radiation from stellar-mass BHs can significantly heat the AGN disk.

Let us now consider the luminosity from stars embedded in the disk. If we assume the Salpeter IMF with mass ranges from 0.1 to 140 $M_\odot$ and the luminosity from Equation (A2), the average luminosity per stellar mass over 100 Myr is $\sim$30 $L_\odot$. If we roughly assume that the number of stars captured by the AGN disk is two orders of magnitude larger than that of BHs with 10 $M_\odot$ (see cyan and orange lines in panel (a) of Figure 10), the total luminosity from stars is lower than that from BHs by a factor of $\sim$300. Hence, we expect that the luminosity from stars are negligible compared to that from BHs.

Overall, we conclude that migration torques (process (ii)) may heat and thicken the AGN disk relative to the model we adopted. Furthermore, radiation from accreting stellar-mass BHs (process (iv)) may also significantly heat the outer regions of the AGN disk. Additionally, more localized structures in the disk (e.g., the widths of the annular gaps around compact objects, local inhomogeneities) may be affected by mechanical feedback from both BHs and stars. Such effects need to be investigated in the future.

5.7.2. Kozai–Lidov Mechanism

There are several possibilities for the Kozai–Lidov (KL) mechanism to affect the dynamical evolution of compact objects in AGN disks. The KL mechanism operates on triple systems when the motion of an inner binary orbit is strongly misaligned with the outer orbit, and the timescale of the KL mechanism is given as

$$t_{\rm KL} = \frac{2}{3\pi}\frac{P_{\rm out}^2}{P_{\rm in}}(1-e_{\rm out}^2)^{3/2}\frac{m_1+m_2+m_3}{m_3} \quad (98)$$

(Kiseleva et al. 1998), where $P_{\rm out}$ and $P_{\rm in}$ are the orbital periods of the outer and inner orbits, respectively, $e_{\rm out}$ is the eccentricity of the outer orbit, m_1 and m_2 are the masses of inner binary components, and m_3 is the mass of the third body. Here, we consider three triple-system configurations, composed respectively of

(i) a compact-object binary and the central SMBH,
(ii) three compact objects,
(iii) the central SMBH, a compact object, and the AGN disk.

For (i) and (ii), the angle between the inner and outer orbits is damped by gas dynamical friction in the AGN disk, which weakens the effect of the KL mechanism. However, if the outer orbit is eccentric, the coplanar configuration may also lead to very high eccentricities and an orbital flip typically on a timescale between 1 and 10$t_{\rm KL}$ (Li et al. 2014). Additionally,

after binary–single interaction and before the binary is captured by the AGN disk, the angle is randomized. During this period, the KL mechanism may efficiently induce mergers.

For (i), the KL timescale is estimated as

$$t_{\rm KL,i} \sim 2\ {\rm Myr}\left(\frac{a_{\rm out}}{0.1\ {\rm pc}}\right)^{3}\left(\frac{a_{\rm in}}{1\ {\rm au}}\right)^{-3/2} \times \left(\frac{m_{\rm bin}}{20\,M_\odot}\right)^{1/2}\left(\frac{M_{\rm SMBH}}{4\times10^{6}\,M_\odot}\right)^{-1} \quad (99)$$

assuming $e_{\rm out} \sim 0$. The KL timescale is shorter than the capture timescale by the AGN disk due to gas dynamical friction (gray and black lines in panel (c) of Figure 10) in the inner regions ($a_{\rm out} \lesssim 0.1$ pc). On the other hand, if the timescale of apsidal precession for either the inner or the outer orbit due to additional mass or general relativity is shorter than the KL timescale, the KL mechanism is typically suppressed (e.g., Fabrycky & Tremaine 2007; Naoz et al. 2013b). Because the timescale for precession due to a circumbinary disk is

$$t_{\rm pre} \sim P_{\rm in}\frac{m_1+m_2}{M_{\rm cir}} \sim 40\ {\rm yr}\left(\frac{a_{\rm in}}{1\ {\rm au}}\right)^{3/2}\left(\frac{m_1+m_2}{20\,M_\odot}\right)^{1/2}\left(\frac{M_{\rm cir}}{0.1\,M_\odot}\right)^{-1} \quad (100)$$

(e.g., Chang 2009), where $M_{\rm cir}$ is the mass of a circumbinary disk, the KL mechanism (i) is suppressed at $r \gtrsim 10^{-3}$ pc where binary–single interactions occur efficiently.

Similarly, the KL timescale for (ii) is

$$t_{\rm KL,ii} \sim 3\ {\rm yr}\left(\frac{a_{\rm out}}{1\ {\rm au}}\right)^{3}\left(\frac{a_{\rm in}}{0.1\ {\rm au}}\right)^{-3/2} \times \left(\frac{m_{\rm bin}}{20\,M_\odot}\right)^{1/2}\left(\frac{M_3}{10\,M_\odot}\right)^{-1} \quad (101)$$

assuming $e_{\rm out} \sim 0$. This timescale is much shorter than the timescale of capture by the AGN disk and shorter than the precession timescale. In AGN disks, such three-body systems presumably efficiently form due to the gas-capture mechanism. If the angle between the inner and outer orbits becomes $\sim 90°$ after inner binary–single interactions and a third body is stably bound after the interactions (Mardling & Aarseth 2001), mergers can be driven by the KL mechanism. Octupole order corrections may lead to close encounters and mergers even in cases where the inclination angle is far from 90° (Naoz et al. 2013a; Hoang et al. 2018a). Due to the KL mechanism, mergers in AGN disks may be further accelerated. Such systems would be worth investigating in the future.

For (iii), during the damping of the velocity of a compact object due to gas dynamical friction when crossing the AGN disk, the eccentricity and the inclination of the orbital motion of the compact object can be exchanged with each other due to the perturbation by the AGN disk as investigated by Vokrouhlicky & Karas (1998) and Šubr & Karas (2005). Chang (2009) estimated that for this KL oscillation to operate, the mass of stars and BHs within a radius r needs to be smaller than the mass of the gas disk within the same radius. In our fiducial model, the mass of stars and BHs is always higher than the gas disk's mass, making the KL mechanism inefficient.

In summary, the KL mechanism for systems composed of three compact objects (ii) formed by gas-capture mechanism may further facilitate mergers. This can be the case if the angular momentum directions between the inner and outer orbits become close to orthogonal after a binary–single interaction, or if the inner orbit is highly eccentric.

5.7.3. Interaction with an SMBH–IMBH Binary

A hard IMBH–SMBH binary can form whenever IMBHs are present in the AGN disk. Here we consider the interaction of compact objects with such an IMBH–SMBH binary. If compact objects migrate inward in the AGN disk, they can gradually approach the IMBH. In this case, after entering the Hill radius of the IMBH, the third body is captured by the IMBH due to the high gas density (Equation (68)).

On the other hand, if a third body orbiting outside of the AGN disk comes close to an IMBH, it can suffer a strong kick via the slingshot mechanism. For high-mass ratio binaries, it takes a long time for a third body to receive a strong kick, presumably due to the small Hill radius of an IMBH (Figure 2 in Bonetti et al. 2020). Furthermore, stellar-mass binaries can be disrupted by an IMBH as they push the binary close to the SMBH where the tidal forces disrupt the binary (Deme et al. 2020). Treating the dynamical evolution of stars and BHs interacting with an SMBH–IMBH binary is beyond the scope of our present study, but should be studied in the future via direct N-body simulation.

5.8. Spatial Distribution of Surviving Binaries

The observed LMXBs found by Hailey et al. (2018) provide useful constraints for theories of binary formation and evolution in the Galactic center. Interestingly, Hailey et al. (2018) have shown that the LMXB candidates are found only within $\sim$1 pc despite the fact that other X-ray sources have been observed out to $\sim$ 4 pc (Muno et al. 2009). The possible reason for the cutoff at $\sim$1 pc in the LMXB distribution has not been previously explained.

Figure 20 shows the spatial distribution of hard binaries at 1, 3, 10, and 20 Myr in the fiducial model. Different colored lines show the distribution of binaries formed by different mechanisms. To select the binaries that would survive until today, we impose the following conditions:

(i) The timescale of merger by GW radiation is longer than 10 Gyr.

(ii) The binary is hard compared to the spherical stellar component (Gould 1991; Binney & Tremaine 2008),

$$s_j < \frac{G m_{j_1} m_{j_2}}{\bar{m}_{\rm star} v_{\rm Kep}^2}, \quad (102)$$

where $\bar{m}_{\rm star}$ is defined below Equation (4).

(iii) The timescale of binary–single interactions with the spherical stellar component at separation $s_{\rm GW}$ is longer than 10 Gyr, where $s_{\rm GW}$ is the separation from which the binary merges in a Hubble time for the mass of the binary and assuming zero eccentricity (Peters 1964).

Condition (i) removes binaries whose separation is smaller than

$$s_{\rm GW} = 0.053\ {\rm au}\left(\frac{m_{j_1}}{5\,M_\odot}\right)^{1/4}\left(\frac{m_{j_2}}{5\,M_\odot}\right)^{1/4}\left(\frac{m_j}{10\,M_\odot}\right)^{1/4}, \quad (103)$$

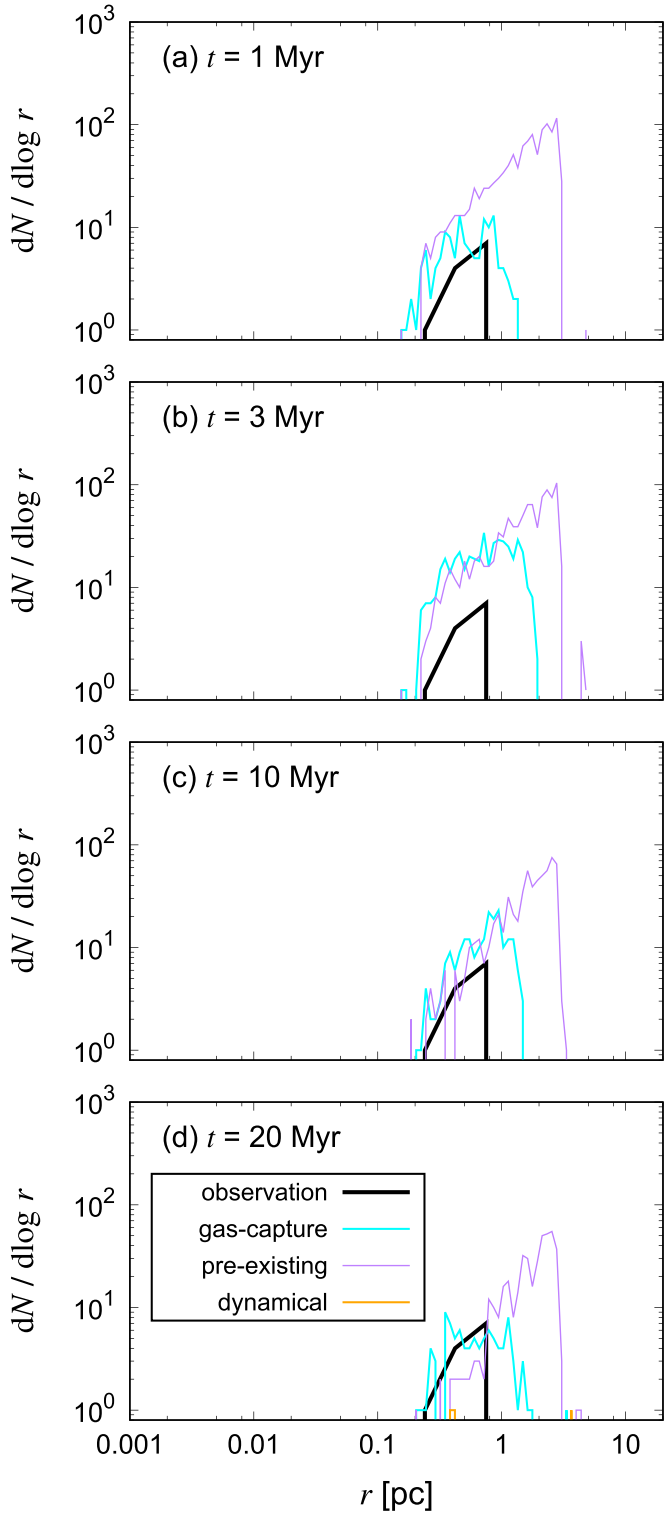

Figure 20. Final binary distribution as a function of the distance from the SMBH r for the fiducial model at $t = 1$, 3, 10, and 20 Myr for the fiducial model. Cyan, purple, and orange lines are the distributions for gas-capture-formed binaries, preexisting binaries, and dynamically formed binaries, respectively. The thick black line shows the observed distribution of X-ray binary candidates (Hailey et al. 2018) as a function of the projected distance from the Galactic center. These binaries satisfy the following conditions: (i) the timescale of merger by GW radiation is longer than 10 Gyr. (ii) The binary is hard compared to the spherical stellar component ($Gm_{j_1}m_{j_2}/(2s_j) > (1/2)\bar{m}_{\rm star}v_{\rm Kep}^2$). (iii) The timescale of binary–single interaction with the spherical stellar component at separation $s_{\rm GW}$ is longer than 10 Gyr. Gas-capture binaries can reproduce the distribution of the observed X-ray binaries.

which corresponds to lower regions ($s \lesssim 10^{-7}$ pc) in Figure 8. Condition (ii) accounts for the lack of the purple points in the upper-left region in panel (a)). Condition (iii) produces the inner cutoff at ∼0.1 pc. Conditions (i), (i)+(ii), and (i)+(ii)+(iii), respectively, exclude 1622, 1709, and 1880 binaries from the set of 2750 binaries at 10 Myr.

The outer cutoff seen in gas-capture binaries (cyan lines in Figure 20) can be explained by the competition between binary hardening due to gas dynamical friction and type I/II migration in the AGN disk, whose timescales are shown by the blue and orange lines in panel (c) of Figure 10, respectively. In model 1, these timescales become equal at around ∼ parsec. At $\gtrsim$ parsec, migration is faster than hardening. Thus, before gas-capture binaries become hard, they migrate in to $\lesssim$ parsec. The exact position of the outer cutoff for gas-capture binaries is influenced by the scale height of the AGN disk (black line in Figure 4) and the binary mass, which affect the ratio of the migration and hardening rates (Equations (17) and (27)). As the scale height decreases or the binary mass decreases, the cutoff moves to inner regions.

For preexisting binaries, the outer cutoff is at ∼3 pc (purple lines in Figure 20), reflecting our assumed initial BH distribution. Because the BH distribution extends to larger radii (e.g., Freitag et al. 2006; Antonini 2014; Feldmeier et al. 2014; Schödel et al. 2014; Generozov et al. 2018), preexisting binaries may not have the outer cutoff at ∼1 pc as in the LMXB observations. However, the fraction of preexisting binaries among all binaries in the Galactic center is poorly constrained; it may be subdominant. Due to the rapid hardening expected during the common-envelope phase, the formation of LMXBs is puzzling (Podsiadlowski et al. 2003; Wiktorowicz et al. 2014; Li 2015; Wang et al. 2016). This is especially the case in galactic nuclei where only hard binaries are long lived, so that surviving the common-envelope phase without merging is even more difficult (Stephan et al. 2019).

These considerations suggest gas-capture binaries as a possible origin of LMXBs. Therefore, we compare the number of LMXBs between observations and our models. Including the undetected population of faint sources, the total number of LMXBs in the Galactic Center is estimated to be hundreds to a thousand (Hailey et al. 2018). In our simulation, several hundreds to thousands of binaries survive until the dissipation of the AGN disk (Table 3). Also, the number of gas-capture binaries, which would survive until today, at 1, 3, 10, and 20 Myr in Figure 20 is 134, 441, 205, and 96 respectively. Note that we only consider the evolution of BH–BH binaries, leaving the corresponding number of LMXBs uncertain. Because stars outnumber BHs in the disk at $\gtrsim$0.1 pc (Figure 10), stars are expected to reside frequently in binaries. However, to estimate the number of LMXBs, we need to consider the fact that massive objects more commonly reside in binaries after binary–single interactions (e.g., Heggie et al. 1996). Also, after the dissipation of the AGN disk, the distribution of BHs may evolve due to two-body relaxation whose timescale is uncertain and comparable to the Hubble time (e.g., Merritt 2010; Emami & Loeb 2020). To understand the relation between the binary evolution in the AGN disk and the observed LMXBs in detail requires one to account for the effect of stellar relaxation processes. Also, vector resonant relaxation redistributes the orbital angular momentum vector directions of LMXBs around the SMBH (Kocsis & Tremaine 2011b; Szolgyen & Kocsis 2018), which is roughly

consistent with the two-dimensional distribution of LMXBs (Hailey et al. 2018).

Finally, the apparent paucity of high-mass X-ray binaries (HMXBs) in the Galactic Center is an interesting additional piece of information for binary formation and evolution. The lack of HMXBs in our scenario may be explained by the short lifetime of massive stars if these HMXBs formed during long-past AGN phases, although there are suggestions that the last AGN phase occurred as recently as several Myr ago in the Galaxy (Nayakshin et al. 2007; Wardle & Yusef-Zadeh 2008; Su et al. 2010; Bland-Hawthorn et al. 2013).

6. Conclusions

In this paper, we investigated mergers of BHs in accretion disks during the active phase of galactic nuclei. We performed one-dimensional *N*-body simulations combined with a semianalytical model. While simplified, this model allows us to incorporate the formation and disruption of binaries, binary–single interactions, weak gravitational scattering with ambient stars, gas dynamical friction in the AGN disk, binary hardening due to type I/II torques from circumbinary disks and gas dynamical friction, migration in the AGN disk, star formation, and GW radiation. Our main results can be summarized as follows:

1. Gas-capture binaries, which have been ignored in previous studies, contribute ∼58%–97% of all BH–BH mergers in the AGN disk, with dynamically formed binaries contributing up to ∼6% (Table 3).
2. After their formation, binaries in the AGN disk are hardened by gas dynamical friction, binary–single interactions with disk stellar and BH components, and finally by gravitational radiation (Figure 5). Because binaries efficiently migrate to the inner regions of the disk ($\lesssim$0.01 pc) before they merge, Doppler acceleration due to their center-of-mass motion around the SMBH is expected to be observable in many cases by the future GW detector LISA (Section 5.2).
3. Due to the recoil kick at frequent binary–single interactions, ∼80% of mergers occur outside the AGN disk. In this case, the binaries' orbital planes at merger are randomly oriented.
4. On the other hand, ∼20% of mergers occur inside the AGN disk. In this case, due to accretion from a circumbinary disk, some degree of (anti)alignment of the BH spins with the binary's internal orbital angular momentum is expected, as suggested in the high-effective-spin merger candidates, GW 151216, GW 170403, and GW 170817A (Section 5.1).
5. Due to frequent binary–single interactions during the binary inspiral, the binary eccentricity is thermalized in the LISA band. LISA will detect such highly eccentric binaries (Section 5.3).
6. The binary separation is driven predominantly by binary–single scattering interactions in the evolutionary phase preceding the GW-driven merger. The GW frequency is already in the LISA band in the binary–single interaction-driven phase, which may be identified by a significant GW phase shift for individual sources and/or the frequency distribution of a population of sources (Section 5.4).
7. We explicitly compute the binary fraction, the capture fraction to AGN disks, the merger fraction of binaries, and the dependence of the merger fraction on the lifetime of the AGN disk. Accounting for uncertainties in these quantities, we find a volumetric BH merger rate of $\sim$0.02–60 Gpc^{-3} yr^{-1}, whose uncertainties are reduced by several orders of magnitude compared to prior works (McKernan et al. 2018).
8. Due to repeated mergers, this pathway naturally explains "heavy" BHs detected in existing GW observations, even if BHs are born with much smaller ($\lesssim 15 M_\odot$) masses. Our model also predicts that mergers of yet more massive BHs ($\gtrsim 10^2\ M_\odot$) will be detected by LIGO in the future (Figure 14). IMBHs formed during repeated mergers in an AGN in most of our models (one exception is model 2 where gas-driven migration was turned off).
9. The maximum rate of EMRIs involving stellar-mass BHs is roughly estimated to be ∼0.1–0.6 Gpc^{-3} yr^{-1}, which could largely contribute to the total EMRI rate, as well as possibly to the total IMRI rate (Section 5.5.3).
10. The distribution of surviving binaries formed by the gas-capture mechanism can reproduce the spatial distribution of LMXBs observed in the Galactic center, including their outer cutoff at ∼1 pc. This cutoff arises from the competition between binary hardening by gas dynamical friction and type I/II migration in the disk (Section 5.8). Binaries migrate inside $\lesssim$1 pc before they are hardened.

In this paper, we employed simplified prescriptions and ignored the exchange of binary components during binary–single interactions and the evolution in the binary eccentricities, as well as other possibly important processes (see Section 2). These issues will be further investigated in the future.

We thank Imre Bartos, Barry McKernan, Yuri Levin, Brian Metzger, Hidekazu Tanaka, Alexander Rasskazov, Massimo Ricotti, and Alessandro Trani for useful discussions. This project was supported by funds from the European Research Council (ERC) under the European Union's Horizon 2020 research and innovation program under grant agreement No 638435 (GalNUC) and by the Hungarian National Research, Development, and Innovation Office grant NKFIH KH-125675. This research was supported in part by the National Science Foundation under grant No. NSF PHY-1748958. Z.H. acknowledges support from NASA grant NNX15AB19G and NSF grant 1715661. Simulations and analyses were carried out on Cray XC50 and other computers at the Center for Computational Astrophysics, National Astronomical Observatory of Japan.

Appendix A
Conversion Efficiency

In the disk model of Thompson et al. (2005), the outer regions of the AGN disk are stabilized by radiation pressure and supernovae from in situ formed stars. The model introduces a parameter ϵ defined as the conversion efficiency with which star formation converts mass into radiation and uses this parameter to calculate the stellar contribution of radiation pressure and the radiative flux. We modify the calculation of ϵ by accounting for the stellar and AGN lifetimes. The radiation flux of main-sequence stars formed in the disk averaged over the two disk faces is

$$F_{\rm AGN,*} = \frac{\sum_i^{N_{\rm form}} L(m_{{\rm star},i}) \min[t_{\rm AGN},\, t_{\rm star}(m_{{\rm star},i})]}{2 A t_{\rm AGN}}, \quad \text{(A1)}$$

where $A = \pi r^2$ is the disk's area of radius r, $t_{\rm star} = 10\ {\rm Gyr}(m_{\rm star}/M_\odot)(L_{\rm star}/L_\odot)^{-1}$ is the lifetime of a star (Hansen & Kawaler 1994), $t_{\rm AGN} = 100$ Myr is the typical lifetime of AGN disks, $N_{\rm form}$ is the number of stars formed during the AGN phase, and $L(m_{\rm star})$ is the luminosity of a star of mass $m_{\rm star}$:

$$L(m_{\rm star}) = \begin{cases} 0.27\,L_\odot (m_{\rm star}/M_\odot)^{2.6} & \text{for } m_{\rm star} < 0.5\,M_\odot, \\ L_\odot (m_{\rm star}/M_\odot)^{4.5} & \text{for } 0.5\,M_\odot < m_{\rm star} < 2\,M_\odot, \\ 1.9\,L_\odot (m_{\rm star}/M_\odot)^{3.6} & \text{for } 2\,M_\odot < m_{\rm star} < 42\,M_\odot, \\ 32000\,L_\odot (m_{\rm star}/M_\odot) & \text{for } 42\,M_\odot < m_{\rm star} < 140\,M_\odot \end{cases} \tag{A2}$$

(Salaris & Cassisi 2005). In Equation (A1), we introduced the limitation of the stellar lifetime during an AGN episode. The conversion efficiency ϵ is defined as

$$F_{{\rm AGN},*} = \frac{1}{2}\epsilon \dot{\Sigma}_* c^2, \tag{A3}$$

where the $\dot{\Sigma}_*$ is the star formation rate surface density, which is given by

$$\dot{\Sigma}_* = \frac{\sum_i^{N_{\rm form}} m_{{\rm star},i}}{A t_{\rm AGN}}. \tag{A4}$$

Combining Equations (A1), (A3), and (A4), and that $m_{{\rm star},i}$ are drawn from the IMF, ϵ is expressed as

$$\epsilon = \frac{\int L(m_{\rm star}) \min[t_{\rm AGN},\, t_{\rm star}(m_{\rm star})]\, \frac{dN}{dm} dm_{\rm star}}{\int m_{\rm star} c^2 \frac{dN}{dm} dm_{\rm star}}. \tag{A5}$$

The result lies between $\epsilon = 1.5 \times 10^{-4}$ and 7.7×10^{-4} depending on the IMF exponent between $dN/dm \propto m^{-2.35}$ and $m^{-1.7}$. The limitation due to the stellar and AGN lifetimes reduces ϵ by a factor of $\sim$4.

Appendix B
Scattering in Two Dimensions

We utilize the following approximations to evaluate the first- and second-order diffusion coefficients during gravitational scattering encounters in two dimensions, Equations (50)–(51) in the main text,

$$D[\Delta v_\parallel] = -G\Sigma_{\rm c} \times \begin{cases} 2^{1/2}\pi^{3/2} e^{-x}(x^{1/2} + \frac{1}{2}x^{3/2} + \frac{1}{4}x^{5/2}) & \text{for } v < 2.3\sigma_{\rm c}, \\ 2\pi & \text{for } v > 2.3\sigma_{\rm c}, \end{cases} \tag{B1}$$

$$D[\Delta v_\perp^2] = D[\Delta v_\parallel^2] = G\Sigma_{\rm c} \times \begin{cases} (2\pi)^{3/2} \frac{\sigma_{\rm c} m_{\rm c}}{m + m_{\rm c}} e^{-x}(\frac{1}{2} + x + \frac{5}{8}x^2 + \frac{1}{4}x^3) & \text{for } v < 2.3\sigma_{\rm c}, \\ \pi \frac{\sigma_{\rm c} m_{\rm c}}{m + m_{\rm c}}[(4x+1)/\sqrt{x}] & \text{for } v > 2.3\sigma_{\rm c} \end{cases}, \tag{B2}$$

where we use $I_0(x) \approx 1 + \frac{1}{4}x^2$ and $I_1(x) \approx \frac{1}{2}x$ for small x and $I_0(x) \approx I_1(x) \approx e^x/\sqrt{2\pi x}$ for large x. The boundary between the two cases is adjusted to give comparable errors for the two formulae, and the maximum error of the approximated formulae is $\sim$10% at the boundary. The acceleration is calculated as

$$\boldsymbol{a}_{{\rm WS},k} = p_{{\rm c},k}\left\{ D[\Delta v_\parallel]\hat{\boldsymbol{v}}_k + \left(\frac{D[\Delta v_\perp^2] + D[\Delta v_\parallel^2]}{\Delta t} \right)^{1/2} \hat{\boldsymbol{n}}_{xy} \right\}, \tag{B3}$$

where $\boldsymbol{n}_{xy}$ is a unit vector in a random direction in the xy (AGN) plane. In the simulation, we adopt an acceleration in unit time Δt.

ORCID iDs

Zoltán Haiman https://orcid.org/0000-0003-3633-5403
Bence Kocsis https://orcid.org/0000-0002-4865-7517

References

Aarseth, S. J., & Heggie, D. C. 1976, A&A, 53, 259
Abbott, B. P., Abbott, R., Abbott, T. D., et al. 2016a, PhRvL, 116, 241103
Abbott, B. P., Abbott, R., Abbott, T. D., et al. 2016b, PhRvL, 116, 061102
Abbott, B. P., Abbott, R., Abbott, T. D., et al. 2017a, PhRvL, 118, 221101
Abbott, B. P., Abbott, R., Abbott, T. D., et al. 2017b, PhRvL, 119, 141101
Abbott, B. P., Abbott, R., Abbott, T. D., et al. 2017c, PhRvL, 119, 161101
Abbott, B. P., Abbott, R., Abbott, T. D., et al. 2019a, PhRvX, 9, 031040
Abbott, B. P., Abbott, R., Abbott, T. D., et al. 2019b, ApJ, 883, 149
Abt, H. A. 1983, ARA&A, 21, 343
Aharon, D., & Perets, H. B. 2016, ApJL, 830, L1
Alexander, T., & Hopman, C. 2009, ApJ, 697, 1861
Amaro-Seoane, P., Audley, H., Babak, S., et al. 2017, arXiv:1702.00786
Amaro-Seoane, P., Gair, J. R., Freitag, M., et al. 2007, CQGra, 24, R113
Amaro-Seoane, P., & Preto, M. 2011, CQGra, 28, 094017
Antonini, F. 2014, ApJ, 794, 106
Antonini, F., Toonen, S., & Hamers, A. S. 2017, ApJ, 841, 77
Arca-Sedda, M., Li, G., & Kocsis, B. 2018, arXiv:1805.06458
Armitage, P. J., & Natarajan, P. 2005, ApJ, 634, 921
Artymowicz, P., Clarke, C. J., Lubow, S. H., & Pringle, J. E. 1991, ApJL, 370, L35
Artymowicz, P., Lin, D. N. C., & Wampler, E. J. 1993, ApJ, 409, 592
Askar, A., Szkudlarek, M., Gondek-Rosińska, D., Giersz, M., & Bulik, T. 2017, MNRASL, 464, L36
Babak, S., Gair, J., Sesana, A., et al. 2017, PhRvD, 95, 103012
Bai, X.-N., & Stone, J. M. 2013, ApJ, 767, 30
Baker, J. G., Boggs, W. D., Centrella, J., et al. 2007, ApJ, 668, 1140
Banerjee, S. 2017, MNRAS, 467, 524
Banerjee, S. 2018a, MNRAS, 473, 909
Banerjee, S. 2018b, MNRAS, 481, 5123
Barausse, E., Cardoso, V., & Pani, P. 2015, JPhCS, 610, 012044
Bar-Or, B., & Alexander, T. 2016, ApJ, 820, 129
Bartko, H., Martins, F., Trippe, S., et al. 2010, ApJ, 708, 834
Bartos, I., Kocsis, B., Haiman, Z., & Márka, S. 2017, ApJ, 835, 165
Baruteau, C., Cuadra, J., & Lin, D. N. C. 2011, ApJ, 726, 28
Baruteau, C., & Lin, D. N. C. 2010, ApJ, 709, 759
Bavera, S. S., Fragos, T., Qin, Y., et al. 2019, arXiv:1906.12257
Belczynski, K., Askar, A., Arca-Sedda, M., et al. 2017, A&A, 615, A91
Belczynski, K., Bulik, T., Fryer, C., et al. 2010, ApJ, 714, 1217
Belczynski, K., Daniel, E. H., Bulik, T., & O'Shaughnessy, R. 2016, Natur, 534, 512
Belczynski, K., Kalogera, V., Rasio, F. A., et al. 2008, ApJS, 174, 223
Belczynski, K., Sadowski, A., & Rasio, F. A. 2004, ApJ, 611, 1068
Bell, K. R., & Lin, D. N. C. 1994, ApJ, 427, 987
Bellovary, J. M., mac Low, M. M., McKernan, B., & Ford, K. E. S. 2016, ApJL, 819, L17
Binney, J., & Tremaine, S. 2008, Galactic Dynamics (2nd ed.; Princeton, NJ: Princeton Univ. Press)
Bland-Hawthorn, J., Maloney, P. R., Sutherland, R. S., & Madsen, G. J. 2013, ApJ, 778, 58
Bogdanovic, T., Reynolds, C. S., & Miller, M. C. 2007, ApJL, 661, L147
Bonetti, M., Rasskazov, A., Sesana, A., et al. 2020, MNRAS, 493, L114
Bouffanais, Y., Mapelli, M., Gerosa, D., et al. 2019, ApJ, 886, 25

Breivik, K., Rodriguez, C. L., Larson, S. L., Kalogera, V., & Rasio, F. A. 2016, ApJL, 830, L18
Brown, D. A., & Zimmerman, P. J. 2010, PhRvD, 81, 024007
Broz, M., Chrenko, O., Nesvornu, D., & Lambrechts, M. 2018, A&A, 620, A157
Burtscher, L., Meisenheimer, K., Tristram, K. R. W., et al. 2013, A&A, 558, 149
Campanelli, M., Lousto, C., Zlochower, Y., & Merritt, D. 2007, ApJL, 659, L5
Chang, P. 2009, MNRAS, 393, 224
Chapon, D., & Mayer, L. R. T. 2013, MNRAS, 429, 3114
Crida, A., Morbidelli, A., & Masset, F. 2006, Icar, 181, 587
Cuadra, J., Armitage, P. J., Alexander, R. D., & Begelman, M. C. 2009, MNRAS, 393, 1423
de Mink, S. E., & Mandel, I. 2016, MNRAS, 460, 3545
del Valle, L., & Volonteri, M. 2018, MNRAS, 480, 439
Deme, B., Meiron, Y., & Kocsis, B. 2020, ApJ, 892, 130
Derdzinski, A. M., D'Orazio, D., Duffell, P., Haiman, Z., & MacFadyen, A. 2019, MNRAS, 486, 2754
di Carlo, U. N., Giacobbo, N., Mapelli, M., et al. 2019, MNRAS, 487, 2947
Dittmann, A. J., & Miller, M. C. 2020, MNRAS, 493, 3732
Dominik, M., Belczynski, K., Fryer, C., et al. 2012, ApJ, 759, 52
D'Orazio, D. J., & Loeb, A. 2020, PhRvD, 101, 083031
Duffell, P. C., D'Orazio, D., Derdzinski, A., et al. 2019, ApJ, submitted (arXiv:1911.05506)
Duffell, P. C., Haiman, Z., MacFadyen, A. I., D'Orazio, D. J., & Farris, B. D. 2014, ApJL, 792, L10
Durmann, C., & Kley, W. 2015, A&A, 574, 52
Edgar, R. G. 2007, ApJ, 663, 1325
Emami, R., & Loeb, A. 2020, JCAP, 02, 021
Escala, A., Larson, R. B., Coppi, P. S., & Mardones, D. 2004, ApJ, 607, 765
Fabrycky, D., & Tremaine, S. 2007, ApJ, 669, 1298
Farris, B. D., Duffell, P., MacFadyen, A. I., & Haiman, Z. 2014, ApJ, 783, 134
Feldmeier, A., Neumayer, N., Schödel, R., et al. 2015, A&A, 584, A2
Feldmeier, A., Neumayer, N., Seth, A., et al. 2014, A&A, 570, A2
Fishbach, M., Farr, W. M., & Holz, D. E. 2020, ApJL, 801, L31
Fishbach, M., Holz, D. E., & Farr, B. 2017, ApJL, 840, L24
Fleming, D. P., & Quinn, T. R. 2017, MNRAS, 464, 3343
Fragione, G., Grishin, E., Leigh, N. W. C., Perets, H. B., & Perna, R. 2019, MNRAS, 488, 47
Fragione, G., & Kocsis, B. 2019, MNRAS, 486, 4781
Freitag, M., Amro-Seoane, P., & Kalogera, V. 2006, ApJ, 649, 91
Fujii, M. S., Tanikawa, A., & Makino, J. 2017, PASJ, 69, 94
Fung, J., Shi, J. M., & Chiang, E. 2014, ApJ, 782, 88
Gallego-Cano, E., Schödel, R., Dong, H., et al. 2018, A&A, 609, 26
Gayathri, V., Bartos, I., Haiman, Z., et al. 2020, ApJL, 890, L20
Geller, A. M., Leigh, N. W. C., Giersz, M., Kremer, K., & Rasio, F. A. 2019, ApJ, 872, 165
Generozov, A., Stone, N. C., Metzger, B. D., & Ostriker, J. P. 2018, MNRAS, 478, 4030
Georgiev, I. Y., Boker, T., Leigh, N., Lutzgendorf, N., & Neumayer, N. 2016, MNRAS, 457, 2122
Gerosa, D., & Berti, E. 2017, PhRvD, 95, 124046
Giacobbo, N., Mapelli, M., & Spera, M. 2018, MNRAS, 474, 2959
Goldreich, P., Lithwick, Y., & Sari, R. 2002, Natur, 420, 643
Gondan, L., & Kocsis, B. 2019, ApJ, 871, 178
Gondan, L., Kocsis, B., Raffai, P., & Frei, Z. 2018a, ApJ, 855, 34
Gondán, L., Kocsis, B., Raffai, P., & Frei, Z. 2018b, ApJ, 860, 5
Goodman, J., & Tan, J. C. 2004, ApJ, 608, 108
Gould, A. 1991, ApJ, 379, 280
Graham, M. J., Djorgovski, S. G., Drake, A. J., et al. 2017, MNRAS, 470, 4112
Greene, J. E., & Ho, L. C. 2007, ApJ, 667, 131
Greene, J. E., & Ho, L. C. 2009, ApJ, 704, 1743
Gruzinov, A., Levin, Y., & Matzner, C. D. 2020, MNRAS, 492, 2755
Hailey, C. J., Mori, K., Bauer, F. E., et al. 2018, Nature Letters, 556, 70
Haiman, Z., & Hui, L. 2001, ApJ, 547, 27
Haiman, Z., Kocsis, B., & Menou, K. 2009, ApJ, 700, 1952
Hansen, C. J., & Kawaler, S. D. 1994, Stellar Interiors. Physical Principles, Structure, and Evolution (Berlin: Springer-Verlag)
Heggie, D. C. 1975, MNRAS, 173, 729
Heggie, D. C., Hut, P., & McMillan, S. L. W. 1996, ApJ, 467, 359
Herrmann, F., Hinder, I., Shoemaker, D., Laguna, P., & Matzner, R. A. 2007, ApJ, 661, 430
Hills, J. G. 1975, AJ, 80, 809
Hinder, I., Kidder, L. E., & Pfeiffer, H. P. 2018, PhRvD, 98, 044015
Hoang, B.-M., Naoz, S., Kocsis, B., Rasio, F. A., & Dosopoulou, F. 2018a, ApJ, 856, 140
Hoang, B.-M., Naoz, S., Kocsis, B., Rasio, F. A, & Dosopoulou, F. 2018b, ApJ, 856, 140
Hopman, C., & Alexander, T. 2006, ApJL, 645, L133
Huerta, E. A., Moore, C. J., Kumar, P., et al. 2018, PhRvD, 97, 024031
Hughes, S. A., & Blandford, R. D. 2003, ApJL, 585, L101
Ida, S., & Lin, D. N. C. 2004, ApJ, 616, 567
Inayoshi, K., Hirai, R., Kinugawa, T., & Hotokezaka, K. 2017a, MNRAS, 468, 5020
Inayoshi, K., Ostriker, J. P., Haiman, Z., & Kuiper, R. 2018, MNRAS, 476, 1412
Inayoshi, K., Tamanini, N., Caprini, C., & Haiman, Z. 2017b, PhRvD, 96, 063014
Ivanov, P. B., Papaloizou, J. C. B., Paardekooper, S. J., & Polnarev, A. G. 2015, A&A, 576, A29
Ivanov, P. B., Papaloizou, J. C. B., & Polnarev, A. G. 1999, MNRAS, 307, 79
Ivanova, N., Justham, S., Chen, X., et al. 2013, A&ARv, 21, 59
Just, A., Yurin, D., Makukov, M., et al. 2012, ApJ, 758, 51
Kanagawa, K. D., Muto, T., Tanaka, H., et al. 2015, ApJL, 806, L15
Kanagawa, K. D., Tanaka, H., & Szuszkiewicz, E. 2018, ApJ, 861, 140
Kelley, L. Z., Haiman, Z., Sesana, A., & Hernquist, L. 2019, MNRAS, 485, 1579
Kelly, B. C., & Shen, Y. 2013, ApJ, 764, 45
Kennedy, G. F., Meiron, Y., Shukirgaliyev, B., et al. 2016, MNRAS, 460, 240
Keshet, U., Hopman, C., & Alexander, T. 2009, ApJL, 698, L64
Kim, H., & Kim, W. T. 2007, ApJ, 665, 432
King, A. R., Lubow, S. H., Ogilvie, G. I., & Pringle, J. E. 2005, MNRAS, 363, 49
King, A. R., Pringle, J. E., & Livio, M. 2007, MNRAS, 376, 1740
Kinugawa, T., Inayoshi, K., Hotokezaka, K., & Nakauchi, D. T. N. 2014, MNRAS, 442, 2963
Kiseleva, L. G., Eggleton, P. P., & Mikkola, S. 1998, MNRAS, 300, 292
Kissel, J., & Betzwieser, J. 2018, Ligo document ligo-g 1802164-v1, https://dcc.ligo.org/LIGO-G1802164/public
Klein, A., Boetzel, Y., Gopakumar, A., Jetzer, P., & de Vittori, L. 2018, PhRvD, 98, 104043
Kocsis, B. 2013, ApJ, 763, 122
Kocsis, B., & Levin, J. 2012, PhRvD, 85, 123005
Kocsis, B., & Sesana, A. 2011a, MNRAS, 411, 1467
Kocsis, B., & Tremaine, S. 2011b, MNRAS, 412, 187
Kocsis, B., Yunes, N., & Loeb, A. 2011, PhRvD, 84, 024032
Koppitz, M., Pollney, D., Reisswig, C., et al. 2007, PhRvL, 99, 041102
Kormendy, J., & Ho, L. C. 2013, ARA&A, 51, 511
Kumamoto, J., Fujii, M. S., & Tanikawa, A. 2019, MNRAS, 486, 3942
Laughlin, G., Steinacker, A., & Adams, F. C. 2004, ApJ, 608, 489
Leigh, N. W. C., Geller, A. M., McKernan, B., et al. 2018, MNRAS, 474, 5672
Levin, Y. 2003, arXiv:astro-ph/0307084
Li, G., Naoz, S., Kocsis, B., & Loeb, A. 2014, ApJ, 785, 116
Li, X., Chang, P., Levin, Y., Matzner, C. D., & Armitage, P. J. 2020, MNRAS, 494, 2327
Li, X.-D. 2015, NewARv, 64, 1
Lin, D. N. C., & Papaloizou, J. 1986, ApJ, 309, 846
Liu, B., & Lai, D. 2017, ApJL, 846, L11
Liu, B., & Lai, D. 2018, ApJ, 863, 68
Liu, B., & Lai, D. 2019, MNRAS, 483, 4060
Lodato, G., & Gerosa, D. 2013, MNRAS, 429, L30
Lower, M. E., Thrane, E., Lasky, P. D., & Smith, R. 2018, PhRvD, 98, 083028
Lu, J. R., Do, T., Ghez, A. M., et al. 2013, ApJ, 764, 155
Lubow, S. H., Seibert, M., & Artymowicz, P. 1999, ApJ, 526, 1001
Mandel, I., & de Mink, S. E. 2016, MNRAS, 458, 2634
Mapelli, M. 2016, MNRAS, 459, 3432
Marchant, P., Langer, N., Podsiadlowski, P., Tauris, T., & Moriya, T. 2016, A&A, 588, A50
Marconi, A., Risaliti, G., Gilli, R., et al. 2004, MNRAS, 351, 169
Mardling, R. A., & Aarseth, S. J. 2001, MNRAS, 321, 398
Martini, P. 2004, in Coevolution of Black Holes and Galaxies, Vol. 169, ed. L. C. Ho (Cambridge: Cambridge Univ. Press), 169
Martini, P., & Weinberg, D. H. 2001, ApJ, 547, 12
McKernan, B., Ford, K. E. S., Bellovary, J., et al. 2018, ApJ, 866, 66
McKernan, B., Ford, K. E. S., Kocsis, B., Lyra, W., & Winter, L. M. 2014, MNRAS, 441, 900
McKernan, B., Ford, K. E. S., Lyra, W., & Perets, H. B. 2012, MNRAS, 425, 460
McKernan, B., Ford, K. E. S., O'Shaughnessy, R., & Wysocki, D. 2020, MNRAS, 494, 1203
Meiron, Y., Kocsis, B., & Loeb, A. 2017, ApJ, 834, 200
Merritt, D. 2010, ApJ, 718, 739

Michaely, E., & Perets, H. B. 2019, ApJL, 887, L36
Miller, M. C., Freitag, M., Hamilton, D. P., & Lauburb, V. M. 2005, ApJL, 631, L117
Miralda-Escude, J., & Gould, A. 2000, ApJ, 545, 847
Miranda, R., Munoz, D. J., & Lai, D. 2017, MNRAS, 466, 1170
Moody, M. S. L., Shi, J.-M., & Stone, J. M. 2019, ApJ, 875, 66
Muno, M. P., Bauer, F. E., & Baganoff, F. K. 2009, ApJS, 181, 110
Muñoz, D. J., Miranda, R., & Lai, D. 2019, ApJ, 871, 84
Namekata, D., & Umemura, M. 2016, MNRAS, 460, 980
Naoz, S., Farr, W. M., Lithwick, Y., Rasio, F. A., & Teyssandier, J. 2013a, MNRAS, 431, 2155
Naoz, S., Kocsis, B., Loeb, A., & Yunes, N. 2013b, ApJ, 773, 187
Narayan, R., & McClintock, J. E. 2008, NewAR, 51, 733
Natarajan, P., & Pringle, J. E. 1998, ApJL, 506, L97
Nayakshin, S., Cuadra, J., & Springel, V. 2007, MNRAS, 379, 21
Nishizawa, A., Berti, E., Klein, A., & Sesana, A. 2016, PhRvD, 94, 064020
Norris, M. A., Kannappan, S. J., Forbes, D. A., et al. 2014, MNRAS, 443, 1151
Novak, M., Bañados, E., Decarli, R., et al. 2019, ApJ, 881, 63
Ogilvie, G. I. 1999, MNRAS, 304, 557
O'Leary, R. M., Kocsis, B., & Loeb, A. 2009, MNRAS, 395, 2127
O'Leary, R. M., Meiron, Y., & Kocsis, B. 2016, ApJL, 824, L12
O'Leary, R. M., Rasio, F. A., Fregeau, J. M., Ivanova, N., & O'Shaughnessy, R. 2006, ApJ, 637, 937
Ostriker, E. C. 1999, ApJ, 513, 252
Paardekooper, S.-J., Baruteau, C., Crida, A., & Kley, W. 2010, MNRAS, 401, 1950
Paczynski, B. 1976, in IAU Symp. 73, Structure and Evolution of Close Binary Systems, ed. P. Eggleton, S. Mitton, & J. Whelan (Dordrecht: Reidel), 75
Panamarev, T., Shukirgaliyev, B., Meiron, Y., et al. 2018, MNRAS, 476, 4224
Papaloizou, J. C. B., & Larwood, J. D. 2000, MNRAS, 315, 823
Park, K., & Bogdanovic, T. 2017, ApJ, 838, 103
Park, K., & Ricotti, M. 2013, ApJ, 767, 163
Pavlovskii, K., Ivanova, N., Belczynski, K., & Van, K. X. 2017, MNRAS, 465, 2092
Pérez-Torres, M. A., Alberdi, A., Romero-Cañizales, C., & Bondi, M. 2010, A&A, 519, L5
Peters, P. C. 1964, PhRv, 136, 1224
Pfuhl, O., Alexander, T., & Gillessen, S. 2014, ApJ, 782, 101
Podsiadlowski, P., Rappaport, S., & Han, Z. 2003, MNRAS, 341, 385
Portegies Zwart, S. F., & McMillan, S. L. W. 2000, ApJL, 528, L17
Randall, L., & Xianyu, Z.-Z. 2018, ApJ, 864, 134
Rasskazov, A., & Kocsis, B. 2019, arXiv:1902.03242
Rastello, S., Amaro-Seoane, P., Arca-Sedda, M., et al. 2019, MNRAS, 483, 1233
Regan, J. A., Downes, T. P., Volonteri, M., et al. 2019, MNRAS, 486, 3892
Rödig, C., Dotti, M., Sesana, A., Cuadra, J., & Colpi, M. 2011, MNRAS, 415, 3033
Rodriguez, C. L., Amaro-Seoane, P., Chatterjee, S., et al. 2018, PhRvD, 98, 123005
Rodriguez, C. L., Chatterjee, S., & Rasio, F. A. 2016a, PhRvD, 93, 084029
Rodriguez, C. L., Haster, C.-J., Chatterjee, S., Kalogera, V., & Rasio, F. A. 2016b, ApJL, 824, L8
Romero-Shaw, I. M., Lasky, P. D., & Thrane, E. 2019, MNRAS, 490, 5210
Salaris, M., & Cassisi, S. 2005, Evolution of Stars and Stellar Populations (Weinheim: Wiley-VCH)
Samsing, J., D'Orazio, D. J., Kremer, K., Rodriguez, C. L., & Askar, A. 2020, PhRvD, 101, 123010
Samsing, J., MacLeod, M., & Ramirez-Ruiz, E. 2014, ApJ, 784, 71
Sana, H., de Mink, S. E., de Koter, A., et al. 2012, Sci, 337, 444
Sánchez-Salcedo, F. J., Chametla, R. O., & Santillán, A. 2018, ApJ, 860, 129
Scheuer, P. A. G., & Feiler, R. 1996, MNRAS, 282, 291
Schödel, R., Feldmeier, A., Kunneriath, D., et al. 2014, A&A, 566, A47
Scott, N., & Graham, A. W. 2013, ApJ, 763, 76
Secunda, A., Bellovary, J., mac Low, M.-M., et al. 2019, ApJ, 878, 85
Silsbee, K., & Tremaine, S. 2017, ApJ, 836, 39
Spera, M., Mapelli, M., Giacobbo, N., et al. 2019, MNRAS, 485, 889
Stephan, A. P., Naoz, S., Ghez, A. M., et al. 2016, MNRAS, 460, 3494
Stephan, A. P., Naoz, S., Ghez, A. M., et al. 2019, ApJ, 878, 58
Stone, N. C., Metzger, B. D., & Haiman, Z. 2017, MNRAS, 464, 946
Su, M., Slatyer, T. R., & Finkbeiner, D. P. 2010, ApJ, 724, 1044
Šubr, L., & Karas, V. 2005, A&A, 433, 405
Sugimura, K., Hosokawa, T., Yajima, H., Inayoshi, K., & Omukai, K. 2018, MNRAS, 478, 3961
Szolgyen, A., & Kocsis, B. 2018, PhRvL, 121, 101101
Tagawa, H., Haiman, Z., Bartos, I., & Kocsis, B. 2020, arXiv:2004.11914
Tagawa, H., Kocsis, B., & Saitoh, R. T. 2018, PhRvL, 120, 261101
Tagawa, H., & Umemura, M. 2018, ApJ, 856, 47
Takeo, E., Inayoshi, K., & Mineshige, S. 2020, arXiv:2002.07187
Tanaka, H., Takeuchi, T., & Ward, W. R. 2002, ApJ, 565, 1257
Tang, Y., & MacFadyen, A. Z. H. 2017, MNRAS, 469, 4258
The LIGO Scientific Collaboration & The Virgo Collaboration 2012, arXiv:1203.2674
The LIGO Scientific Collaboration & The Virgo Collaboration 2020, arXiv:2004.08342
Thompson, T. A., Quataert, E., & Murray, N. 2005, ApJ, 630, 167
Tichy, W., & Marronetti, P. 2008, PhRvD, 78, 081501
Tiede, C., Zrake, J., MacFadyen, A., & Zoltan, H. 2020, MNRAS, submitted (arXiv:2005.09555)
Torres, G., Andersen, J., & Gimenez, A. 2010, ARA&A, 18, 67
Toyouchi, D., Hosokawa, T., Sugimura, K., & Kuiper, R. 2020, MNRAS, 496, 1909
Toyouchi, D., Hosokawa, T., Sugimura, K., Nakatani, R., & Kuiper, R. 2019, MNRAS, 483, 2031
Trani, A. A., Fujii, M. S., & Spera, M. 2019, ApJ, 875, 42
Trippe, S., Gillessen, S., Gerhard, O. E., et al. 2008, A&A, 492, 419
Udall, R., Jani, K., Lange, J., et al. 2019, arXiv:1912.10533
Valtonen, M., & Karttunen, H. 2006, The Three-Body Problem (Cambridge: Cambridge Univ. Press)
van den Heuvel, E. P. J., Portegies Zwart, S. F., & de Mink, S. E. 2017, MNRAS, 471, 4256
Venumadhav, T., Zackay, B., Roulet, J., Dai, L., & Zaldarriaga, M. 2020, PhRvD, 101, 083030
Vokrouhlicky, D., & Karas, V. 1998, MNRAS, 298, 53
Volonteri, M., Sikora, M., & Lasota, J.-P. 2007, ApJ, 667, 704
Wada, K., Schartmann, M., & Meijerink, R. 2016, ApJL, 828, L19
Walcher, C. J., van der Marel, R. P., McLaughlin, D., et al. 2005, ApJ, 618, 237
Wang, C., Jia, K., & Li, X.-D. 2016, MNRAS, 457, 1015
Ward, W. R. 1997, Icar, 126, 261
Wardle, M., & Yusef-Zadeh, F. 2008, ApJL, 683, L37
Wen, L. 2003, ApJ, 598, 419
Wiktorowicz, G., Belczynski, K., & Maccarone, T. 2014, in Binary Systems, their Evolution and Environments (Ulaanbaatar: Mongolia-Japan Centre), 37
Williamson, D., Hönig, S., & Venanzi, M. 2019, ApJ, 876, 137
Wong, K. W. K., Baibhav, V., & Berti, E. 2019, MNRAS, 488, 5665
Xu, F., Bian, F., Shen, Y., et al. 2018, MNRAS, 480, 345
Yang, Y., Bartos, I., Gayathri, V., et al. 2019a, PhRvL, 123, 181101
Yang, Y., Bartos, I., Haiman, Z., et al. 2019b, ApJ, 876, 122
Yelda, S., Ghez, A. M., Lu, J. R., et al. 2014, ApJ, 783, 131
Yi, S.-X., Cheng, K. S., & Taam, R. E. 2018, ApJL, 859, L25
Yunes, N., Kocsis, B., Loeb, A., & Haiman, Z. 2011, PhRvL, 107, 171103
Zackay, B., Dai, L., Venumadhav, T., Roulet, J., & Zaldarriaga, M. 2020, PhRvD, 101, 083030
Zackay, B., Venumadhav, T., Dai, L., Roulet, J., & Zaldarriaga, M. 2019, PhRvD, 100, 023007
Zevin, M., Samsing, J., Rodriguez, C., Haster, C.-J., & Ramirez-Ruiz, E. 2019, ApJ, 871, 91
Zhang, F., Shao, L., & Zhu, W. 2019, ApJ, 877, 87
Ziosi, B. M., Mapelli, M., Branchesi, M., & Tormen, G. 2014, MNRAS, 441, 3703
Zubovas, K., King, A. R., & Nayakshin, S. 2011, MNRAS Letters, 415 L21